Fabrication and Characterization of Hierarchical Nanostructure Materials

by

Yue Zhang, B.E., M.S.

A Dissertation

In

INDUSTRIAL ENGINEERING

Submitted to the Graduate Faculty
of Texas Tech University in
Partial Fulfillment of
the Requirements for
the Degree of

DOCTOR OF PHILOSOPHY

Approved

Dr. Shiren Wang
Chair of Committee

Dr. Ismael Regis de Farias Jr.

Dr. Louisa J. Hope-Weeks

Dr. Jingjing Qiu

Dr. Hongchao Zhang

Dominick Casadonte
Interim Dean of the Graduate School

May, 2013

Copyright 2013, Yue Zhang

I would like to dedicate my dissertation to my parents who sacrifice so much for me.

Acknowledgements

First and foremost, I would like to give my sincere gratitude to my mentor, Dr. Shiren Wang, for his guidance, supervision, and help throughout the past four years. He has given me a chance to explore new knowledge, as well as given me precious advice to improve myself to become a better person.

I also wish to express my thanks to Dr. Ismael Regis de Farias JR, Dr. Louisa J. Hope-Weeks, Dr. Jingjing Qiu and Dr. Hongchao Zhang for taking the time to serve as my committee members. They always give me valuable advice on my projects and have helped me a lot with my doctoral program. Deep appreciation also goes to Dr. Jharna Chaudhuri, Dr. Guigen Li, Dr. Brandon L. Weeks, Dr. Iris V. Rivero, Dr. Mark Holtz, Dr. Yanzhang Ma for allowing me using their equipments.

I would like to thank the members of Dr. Wang's group. It has been wonderful to know all of you during the past several years at Texas Tech University. The big thank-you goes to Mr. Liqiang Ren, Mr. Kun Zhang and Mr. Li Li.

I would thank my parents for their endless encouragement and support. I am also grateful to my friends, Mr. Xin Zhang, Mr. Marauo Davis, Mr. Archis Marathe, Mr. Jianbin Wu, and Miss Yu Tian, for their help with my projects. They have always been there for me, no matter where I am. I also appreciate the National Science Foundation for the funding support.

Thank you all from my heart!

Table of Contents

Acknowledgements ii

Abstract viii

List of Tables xi

List of Figures xii

Chapter I Introduction 1

1.1 Motivation 1

1.2 Technical Challenges 2

1.3 Research Objectives 3

Chapter II Literature Review 4

2.1 Structure of Graphene 4

2.2 Properties of Graphene 6

2.2.1 Electrical Conductivity 6

2.2.2 Mechanical Properties 7

2.2.3 Optical Properties 7

2.2.4 Thermal Properties 8

2.3 Synthesis of Graphene 9

2.3.1 Epitaxial Growth 9

2.3.2 Chemical Vapor Deposition 10

2.3.3 Organic Synthesis 13

2.3.4 Mechanical Exfoliation 15

2.3.5 Wet Chemical Synthesis 17

2.3.6 Un-zipping Carbon Nanotubes (CNTs) 26

2.3.7 Summary 28

2.4 Functionalization of Graphene with Nanoparticles 29

2.4.1 In situ Hybridization 29

2.4.2 Ex situ Hybridization 34

2.5 Applications of Nanoparticle Functionalized Graphene 37

2.5.1 Lithium Ion Batteries 37

2.5.2 Supercapacitors 38

2.5.3 Solar Cell 39

2.5.4 Catalyst 39

2.6 Summary 42

Chapter III Silver Nanoparticle/Graphene Hierarchical Nanostructure 43

3.1 Introduction 43

3.2 Experimental 44

3.2.1 Materials and Equipment 44

3.2.2 Graphene Preparation 45

3.2.3 Silver-Ammonia Solution Preparation 48

3.2.4 Ag/Graphene Preparation 48

3.2.5 Characterization 48

3.3 Mechanism Analysis 50

3.4 Characterization of Ag NPs/Graphene Hierarchical Materials 52

3.4.1 XRD Pattern 52

3.4.2 TGA Analysis 54

3.4.3 TEM Analysis 55

3.4.4 Surface Area Analysis 56

3.4.5 Electrical Conductivity Analysis 58

3.4.6 Specific Capacitance 60

3.5 Summary 62

Chapter IV C_{60}/Graphene Hierarchical Nanostructure 63

4.1 Introduction 63

4.2 Experiments of Covalent Functionalization 64

4.2.1 Materials 64

4.2.2 Covalent Synthesis of C60/graphene 64

4.2.3 Preparation of C60/Graphene 65

4.2.4 Characterization 66

4.3 Characterization of Covalently Functionalized C_{60}/Graphene 67

4.3.1 FT-IR Spectroscopy 67

4.3.2 UV-Vis Spectroscopy 68

4.3.3 TGA Analysis 69

4.3.4 AFM Analysis 70

4.3.5 HRTEM Analysis 71

4.4 Summary of Covalent Method 72

4.5 Experiments of Non-covalent Functionalization 73

4.5.1 Materials 73

4.5.2 Preparation of C60/Graphene 73

4.5.3 Characterization 73

4.6 Noncovalent Synthesis of C_{60}/graphene 74

4.7 Characterization of Non-covalently Functionalized C_{60}/Graphene 74

4.7.1 Raman Spectroscopy 74

4.7.2 TEM Analysis 75

4.7.3 Particle Size Analysis 77

4.7.4 XRD Pattern 80

4.7.5 UV-Vis Spectroscopy 81

4.8 Summary of Non-covalent Method 82

4.9 Summary 82

Chapter V Seebeck Effect of C_{60}/Graphene Nanocomposites 83

5.1 Introduction 83

5.2 Experimental 85

5.2.1 Materials 85

5.2.2 Preparation of C60/Graphene Hierarchical Nanostructures 85

5.2.3 Preparation of C60/Graphene/Epoxy Nanocomposites 86

5.2.4 Preparation of C60/Graphene/PEDOT:PSS Nanocomposites 86

5.2.5 Characterization 86

5.3 Power Factor of C_{60}/Graphene/Epoxy Nanocomposites 87

5.4 Power Factor of C_{60}/Graphene/PEDOT:PSS Nanocomposites 89

5.5 Summary 95

Chapter VI Conclusion and Future Work 97

6.1 Conclusions 97

6.2 Future Work 99

References 101

Publications 124

Abstract

Graphene, a one-atom-thick planar sheet of graphite, has demonstrated high electrical conductivity, charge carrier mobility, specific surface area, as well as excellent mechanical and thermal properties. The graphene nanosheets have been integrated with various nanoparticles (NPs) to form NPs/graphene hierarchical nanostructure materials. The hierarchical nanostructure materials exhibit excellent properties and new functionalities due to the synergetic effects between graphene nanosheets and the nanoparticles, and are regarded as one of the most promising materials for energy storage and conversion. However, to date, the wide application of NPs/graphene nanostructures has been hindered due to several technical challenges. The first challenge involves the effective functionalization of graphene with nanoparticles. The second one is a lack of understanding of the processing-structure-property relationship of the hierarchical nanostructure. In this dissertation, two types of nanoparticles (metallic silver nanoparticles and non-metallic C_{60} nanoparticles) were functionalized onto graphene nanosheets. The processing-structure relationship of the hierarchical structures was well studied and analyzed. Moreover, the specific capacitance of the silver NPs/graphene hierarchical nanostructures and the power factor of the C_{60}/graphene/polymer nanocomposites were quantitatively compared and analyzed.

First, the processing-structure-property relationship of silver nanoparticles (Ag NPs)/graphene nanostructure was studied. Silver nanoparticles were deposited onto graphene nanosheets through electrostatic attraction and subsequent reduction. Characterizations by X-ray diffraction and transmission electron microscopy (TEM) have confirmed the formation of Ag NPs/graphene nanostructure. The TEM images and TGA test results showed that the concentration of the silver salt solution can effectively tune the graft density and morphology of the silver nanoparticles on graphene. The nitrogen adsorption/desorption tests indicated that the Ag NPs prevented the restacking of graphene sheets, resulting in larger surface area. The electrical conductivity and the specific capacitance of silver-deposited graphene were improved by adjusting the

concentration of the silver salt solution. Particularly, the electrical conductivity and capacitance increased by three times and two times, respectively, when compared with the as-fabricated graphene nanosheets.

Secondly, the processing-structure relationship of C_{60}/graphene nanostructure was investigated. In this study, a novel covalent method and a unique non-covalent method were presented to synthesize the nanostructure. The resultant materials were characterized by FT-IR spectroscopy, UV-Vis spectroscopy, atomic force microscopy, and TEM. The characterization results confirmed that fullerene was successfully attached onto graphene nanosheets through Fisher esterification reaction and liquid-liquid interfacial precipitation, respectively. It was found that the particle size (from 5 to 85 nm), size distribution, and morphology can be tuned by adjusting the concentration of the C_{60} solution, according to particle size analysis.

Finally, the enhancement effect of C_{60}/graphene hierarchical structure on the power factor of polymers was tested by incorporating the C_{60}/graphene hierarchical materials into epoxy resin and poly(3,4-ethylenedioxythiophene) poly(styrenesulfonate) (PEDOT:PSS). The electrical conductivity of epoxy resin was significantly increased with the hierarchical structures. An optimal power factor of 1.1 $\mu W/K^2m$ was achieved with the addition of 45 wt% C_{60}/graphene hierarchical nanostructure. When incorporated the hierarchical materials with the PEDOT:PSS, the Seebeck coefficient increased through an energy-filtering effect between the hierarchical nanostructure and the PEDOT:PSS. A power factor of 32.4 $\mu W/mK^2$, which was ~50% higher than the value of pure PEDOT:PSS, was achieved by properly adjusting the weight ratio between the C_{60}, graphene and PEDOT:PSS.

By developing three novel methods to functionalize graphene with nanoparticles, this dissertation thoroughly analyzes the processing-structure relationship of Ag NPs/graphene and C_{60}/graphene hierarchical nanostructure. Through these investigations, the specific capacitance and power factor of the hierarchical nanostructures and their composites were improved. This dissertation therefore provides guidance for the design

and fabrication of the NPs/graphene hierarchical nanostructures in order to achieve better energy storage and conversion performance.

List of Tables

2.1 Electrical conductivities of rGO prepared by different approaches.....26

2.2 Comparison of various methods for preparation of graphene 28

2.3 Preparation of NPs/graphene nanostructures and applications of the materials 41

3.1 List of materials used in the experiments 44

3.2 List of used equipments 45

3.3 Weight percentage of silver nanoparticles on Ag deposited graphene 55

3.4 Surface area of Ag NPs/graphene samples and as-produced graphene 57

5.1 Samples with different weight percent of fillers in composite and different weight percent of C_{60} in fillers.....89

List of Figures

1.1 Allotropes of carbon [6]. 1

2.1 Graphene is a 2D building material for carbon materials. It can be wrapped up into 0D buckyballs, rolled into 1D nanotubes or stacked into 3D graphite [14]. 4

2.2 (a) sp^2 hybrid orbitals of carbon atoms in graphene [15]. (b) The TEM image shows the atomic structure of graphene [16]. 5

2.3 "Rippled graphene" from a Monte Carlo simulation. The red arrows are ~8 nm long [17]. 5

2.4 (a) Ambipolar electric field effect in single-layer graphene [14]. (b) Charge mobility as a function of charge density [4]. 6

2.5 (a) Scanning electron micrograph of a large graphene flake spanning an array of circular holes. Scale bar, 3 μm [1]. (b) Schematic of nanoindentation on suspended graphene membrane [1]. 7

2.6 Optical micrograph of one- and two-atom thick graphene layers [25]. 8

2.7 Epitaxial graphene growth on metal single crystals [36]. 10

2.8 The CVD synthesis of large area graphene on copper substrate [36]. 11

2.9 (a) Schematic of the roll-based production of graphene films grown on a copper foil. (b) Roll-to-roll transfer of graphene films from a thermal release tape to a PET film. (c) A transparent ultralarge-area graphene film transferred on a 35-inch PET sheet. (d) An assembled graphene/PET touch panel showing outstanding flexibility. (e) A graphene-based touch-screen panel [45]. 12

2.10 Molecular structure of HBC [46] (a) and graphite discs with 150 carbon (b) [46] and 222 carbon (c) [47]. 13

2.11 Basic steps for surface supported GNRs synthesis. Grey, white, and red balls stand for carbon atom, hydrogen atom and halogen atom, respectively [52]. 14

2.12 (a) Mechanical exfoliation of graphene using scotch tape from HOPG. (b) Single-layer graphene observed by AFM. Double-folds single layer graphene with a thickness of 0.8nm [19]. 16

2.13 The process of producing graphene through thermal reduction and chemical reduction of graphite oxide. "OX", "RED", "TR", and "CR" stand for oxidation, reduction, thermal reduction, and chemical reduction, respectively [68]. 18

2.14 Proposed configurations for graphene oxide [73]. 19

2.15 Scheme of producing graphene through thermal exfoliation of graphite oxide. Carbon, oxygen, and hydrogen atoms are shown in gray, red, and white, respectively [65]. 20

2.16 (a) A proposed reaction mechanism for epoxy reduction by hydrazine [86]. (b) Oxidation of graphite to graphene oxide and reduction to reduced graphene oxide [33]. 22

2.17 The scheme of multi-step reduction of graphene oxide with $NaBH_4$ [89]. 23

2.18 Scheme showing the chemical route of the synthesis of aqueous graphene dispersions. 1. Oxidation of graphite to graphite oxide with increased interlayer distance. 2. Exfoliation of graphite oxide in water by sonication to obtain graphene oxide colloids that are stabilized by electrostatic repulsion. 3. Conversion of graphene oxide to graphene through reduction with hydrazine [96]. 24

2.19 (a) Scheme of the gradual unzipping of one wall of a carbon nanotube to form a nanoribbon [115]. AFM images of (b) pristine, (c) partially and (d) fully unzipped nanotubes, respectively [118]. 27

2.20 (a) Scheme shows the formation of Pt NPs/ rGO hybrid. (b) TEM images of the Pt/rGO hybrid [126]. 30

2.21 Reduction of GO through light irritation of TiO_2 [129]. 31

2.22 Schematic illustration of the formation mechanism of the graphene/iron oxide nanostructure [137]. 31

2.23 (a) Scheme of the one-step synthesis of CdS/graphene. (b) Scheme of the solvothermal reduction of GO to graphene in DMSO [143]. 32

2.24 Covalent synthesization of C_{60}/graphene hybrid [165].....35

2.25 Functionalization of graphene oxide with carbon nanotubes through π-π stacking [171].....36

2.26 Schematic illustration of fabrication of graphene-encapsulated metal oxide [170]. 37

3.1 Scheme illustrates the preparation of graphite oxide from graphite and preparation of reduced graphene oxide using thermal exfoliation and chemical reduction.....46

3.2 The process of fabricating graphene through hydrazine reduction.....47

3.3 Illustration of Ag NPs/graphene hybrid formation. 50

3.4 Mechanism of depositing silver nanoparticles on graphene. 51

3.5 XRD results of (a) graphite, (b) graphite oxide, (c) exfoliated graphene, and (d) Ag NPs/graphene. 53

3.6 TGA results of Ag-deposited graphene and graphene. 54

3.7 TEM images of Ag NPs/graphene synthesized by 0.025M (a), 0.05M (b), 0.1M (c), 0.4M (d) and 0.8M (e)(f) $AgNO_3$ solutions (Scale bar of all images: 100 nm).....56

3.8 Electrical conductivity of Ag NPs/graphene hybrid with different weigh percentages.....59

3.9 Capacitor using Ag NPs/graphene on positive electrode. (The Ag/AgCl reference electrode was omitted in this figure).....61

3.10 Cyclic voltammograms of graphene, Ag NPs/graphene (0.1M) and Ag NPs/graphene (0.8M) in 0.5 M Na_2SO_4 with a scan rate of 2 mVs^{-1}.....61

4.1 Exfoliation and functionalization of the graphite oxide with (1, 2-Methanofullerene C_{60})-61-carboxylic acid via the Fisher esterification. 65

4.2 FT-IR spectra of (a) graphite oxide and (b) fullerene-functionalized graphene. 68

4.3 UV-Vis spectra of graphite oxide and fullerene-functionalized graphene. Inset: a photograph of graphite oxide (left) and fullerene functionalized graphene (right) dispersion at the same concentration (100mg/mL). 69

4.4 TGA results of fullerene, graphite oxide and fullerene-functionalized graphene. 70

4.5 (a) AFM image of graphene sheet. (b) AFM image of fullerene-functionalized graphene. (c) Section analysis of fullerene-functionalized graphene. 71

4.6 HRTEM image of fullerene-functionalized graphene compound. 72

4.7 Attachment of C_{60} nanoparticles onto graphene. 74

4.8 Raman spectra of C_{60}, graphene and C_{60}/graphene. 75

4.9 TEM images of (a) graphene. TEM images of C_{60}/graphene hybrid fabricated using (b) 0.1 mg/ml, (c) 0.5 mg/ml, (d) 0.75 mg/ml, (e) 1 mg/ml, (f) and 2 mg/ml C_{60} solution. (Scale bar for all images: 100 nm). 77

4.10 Size distribution of C_{60} clusters using (a) 0.5, (b) 0.75, (c) 1, and (d) 2 mg/ml C_{60}/m-xylene solution and (e) particle size comparisons of samples using different C_{60} concentration. 79

4.11 XRD patterns of (a) graphite, (b) graphite oxide, (c) reduced graphene, and (d) C_{60}/graphene nanostructures. 80

4.12 UV-Vis spectra of C_{60} and C_{60}/graphene hybrid in solution. 81

5.1 (a) Electrical conductivity, Seebeck Coefficient, and (b) power factor of the C_{60}/graphene/epoxy composite. 88

5.2 (a) Electrical conductivity, Seebeck coefficient, and (b) power factor of the PEDOT:PSS and composites with different load of C_{60}/graphene. 91

5.3 (a) Electrical conductivity, Seebeck coefficient, and (b) power factor of the composites composing fillers with different weight percent of C_{60}. 94

5.4 (a) Scheme illustrates the influence of C_{60} coverage on the electrical conductivity of the C_{60}/graphene/PEDOT:PSS composite. (b) The circuit conducting analogue schematic of (b) composite with less C_{60} and (c) composite with more C_{60}. (Purple: graphene, green: PEDOT:PSS, red: C_{60}). 95

Chapter I

Introduction

1.1 Motivation

Graphene is a 2D sheet with one carbon atom thick. It is regarded as basic building materials for fullerene, nanotubes, and graphite (Figure 1.1). Investigations have shown that graphene integrates many amazing and excellent properties, such as high Young's modulus (~1 TPa) [1], tensile strength (130 GPa) [1], thermal conductivity (3000–5000 W m^{-1} K^{-1}) [2, 3], carrier mobility (200000 $cm^2V^{-1}s^{-1}$) [4], and theoretical specific surface area (2630 m^2g^{-1}) [5].

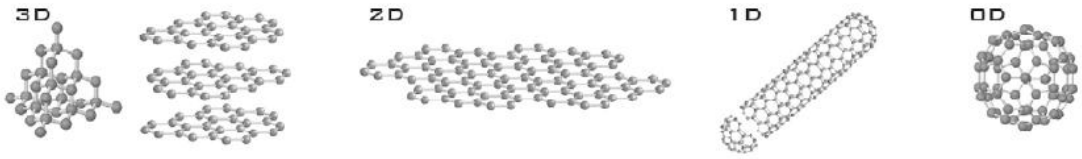

Figure 1.1 Allotropes of carbon [6].

Especially, the high surface area of graphene makes it an ideal supporting material for other nanomaterials. However, due to the restacking of graphene layers, the experimental values of the specific surface area of graphene were much lower than the theoretical values [7]. To solve this problem, zero dimensional nanoparticles have been integrated with graphene to form NPs/graphene hierarchical nanostructure. The zero dimensional nanoparticles have high specific surface area and work as spacers to prevent the restacking of graphene layers, and thus create materials with higher surface areas [8]. In addition, the electrical properties of the hierarchical nanostructure can be tuned by incorporating nanoparticles with different electrical performance. More importantly, different types of nanoparticles exhibit various properties, such as surface plasmon resonance, antimicrobial activity, catalytic activity and unique optical properties [9, 10]. The integration of nanoparticles brings graphene with excellent properties and new

functionalities through the synergetic effects between graphene layers and the nanoparticles. Due to the improved properties, the nanoparticles/graphene hierarchical nanostructures have been widely used in the field of catalysis, energy, analytical and biotechnology [11]. Particularly, with recent achievement in enhanced performances and anticipated commercialization in the near future, the NPs/graphene hierarchical nanostructures are attractive candidates in energy storage and thermoelectric energy conversion based applications [12]. However, the research of the NPs/graphene hierarchical nanostructures on the energy storage and conversion is limited.

1.2 Technical Challenges

In the past few years, even though some great progress has been made towards understanding the unique structure and properties of NPs/graphene hierarchical nanostructure materials, the applications of the materials has been hindered by several technical issues.

First, the reports on effective functionalization of graphene with nanoparticles are limited. The excellent properties and new functionalities are only coupled with the synergic effect of nanoparticles and graphene layers. An ineffective functionalization method may lead to a random mixture of the two components, which does not possess the synergic effect [13]. Thus effective methods to fabricate the hierarchical nanostructure rather than random mixtures are highly required.

Second, there's a lack in the understanding of processing-structure-property relationship in the hierarchical nanostructure. The properties of the hierarchical nanostructure is limited by the quality and structures of the components in the hierarchical nanostructure. The expected performance of the hierarchical nanostructures cannot be achieved if the structure of the materials cannot be controlled. Therefore, a successful design and application of the hierarchical nanostructures requires better understanding of the processing-structure-property relationship, which provides methodology to improve the properties of the hierarchical nanostructures.

1.3 Research Objectives

To improve the performance of NPs/graphene on energy storage and conversion, two different types of nanoparticles were studied. In this dissertation, three new approaches were proposed to fabricate the NPs/graphene hierarchical materials. The processing-structure-property relationship of the hierarchical materials was well studied. Specifically, the research objectives are given as follows:

i. A method was developed to graft silver nanoparticles onto graphene layers. The influence of the concentration of the silver salt solution on the morphology of silver nanoparticles was investigated. The electrical conductivity, specific surface area, and specific capacitance of the hierarchical nanostructure were analyzed.

ii. Methods to functionalize graphene with C_{60} molecules were studied. The C_{60} molecules were incorporated with graphene through covalent method (Fisher esterification) and non-covalent method (liquid-liquid interfacial precipitation). The processing effect on the particle size was investigated.

iii. The fabricated C_{60}/graphene hierarchical materials were incorporated into two types of polymer matrixes (epoxy resin and PEDOT:PSS). The power factor of these two composites was tested. The effect of the C_{60}/graphene hierarchical materials on the power factor of the nanocomposites was analyzed.

Chapter II

Literature Review

2.1 Structure of Graphene

Graphene is an allotrope of carbon. It is a one-atom-thick planar sheet of sp^2-bonded carbon atoms that are densely packed in a honeycomb crystal lattice. Graphene is the basic structural element of other graphitic materials including graphite, carbon nanotubes, and fullerenes (Figure 2.1). It can be wrapped up into 0D fullerenes, rolled into 1D nanotubes, or stacked into 3D graphite [14].

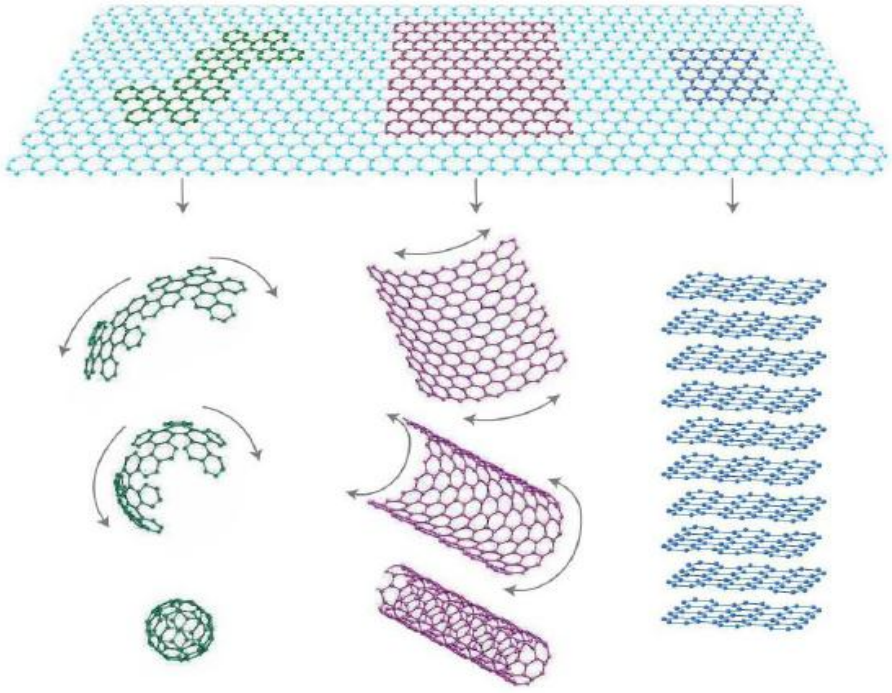

Figure 2.1 Graphene is a 2D building material for carbon materials. It can be wrapped up into 0D buckyballs, rolled into 1D nanotubes or stacked into 3D graphite [14].

Each carbon atom in the lattice has one *s* orbital and three *p* orbitals. Two of the *p* orbitals (*px* and *py*) and the *s* orbital hybridize to form a strong covalent sp^2 C-C bond with a length of 1.42 Å. The remaining *pz* orbital overlaps the *pz* orbital of the neighboring carbon atoms to form a filled π orbital (conduction) and the empty π^* orbital

(valence) (Figure 2.2a). The atomic structure of single-layer graphene was observed by TEM on graphene sheets suspended on a TEM grid (Figure 2.2b).

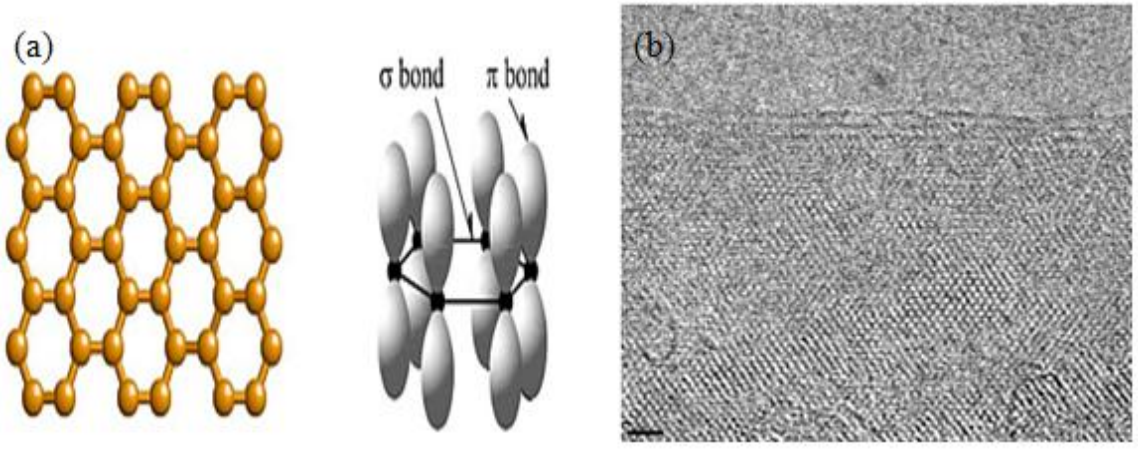

Figure 2.2 (a) sp^2 hybrid orbitals of carbon atoms in graphene [15]. (b) A TEM image shows the atomic structure of graphene (Scale bar: 1nm) [16].

Freely suspended graphene also shows intrinsic ripples, which are estimated to have a lateral dimension of 8 to 10 nm and an amplitude of 0.7 to 1nm (Figure 2.3) [17, 18]. These ripples may be due to the instability of the two-dimensional structure of graphene. By generating crumpling in the third dimension, graphene becomes stable [14].

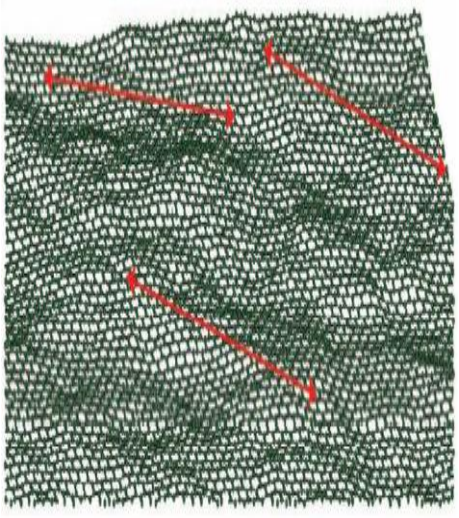

Figure 2.3 “Rippled graphene” from a Monte Carlo simulation. The red arrows are ~8 nm long [17].

2.2 Properties of Graphene

2.2.1 Electrical Conductivity

Many investigations on graphene nanosheets focus on their electrical properties. As a zero-bandgap semiconductor, graphene exhibits tiny overlap between the valence bands and conduction bands [19]. It has been demonstrated that graphene displays a strong ambipolar electric field effect (Figure 2.4a). When gate voltage is applied, the charge carrier concentration and mobility can be tuned to 10^{13} cm^{-2} and 15000 $cm^2V^{-1}s^{-1}$, respectively, at room temperature (Figure 2.4b) [19, 20]. Moreover, the mobility of the holes and electrons of graphene is nearly the same and has a weak dependence on temperature between 10K and 100K [20, 21]. It has been observed that the charge carriers of graphene move with little scattering under ambient conditions [20, 21]. A mobility of 200000 $cm^2V^{-1}s^{-1}$ has been achieved by minimizing impurities scattered in a suspended graphene [4].

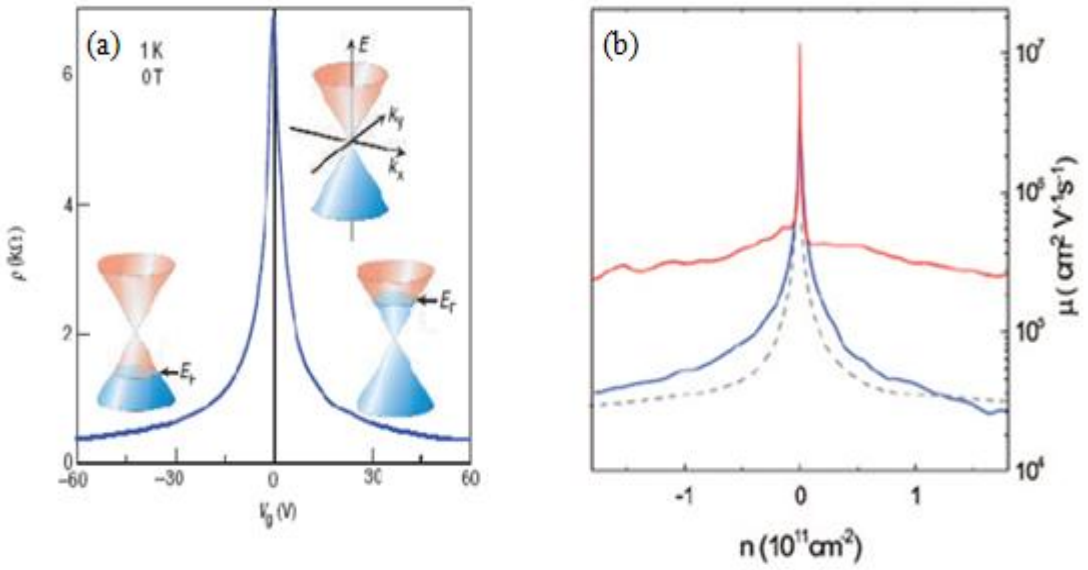

Figure 2.4 (a) Ambipolar electric field effect in single-layer graphene [14]. (b) Charge mobility as a function of charge density [4].

2.2.2 Mechanical Properties

The mechanical properties of graphene, including Young's modulus and fracture strength, have been studied [22, 23]. The mechanical properties of few-layer graphene membranes have been studied experimentally based on force-displacement measurements using atomic force microscopy (AFM) on a graphene strip [23]. Recently, the Young's modulus and intrinsic breaking strength of a free-standing graphene layer were investigated using nanoindentation and AFM (Figure 2.5a and 2.5b) [1]. It was reported that defect-free graphene showed a Young's modulus of 1 TPa and a fracture strength of 130 GPa [1, 23]. Freely suspended oxidized graphene showed a Young's modulus of 0.25 TPa even though there were many defects in it [22]. Graphene papers prepared by assembling graphene oxide sheets showed ~32 GPa of Young's modulus and ~120 MPa of highest fracture strength [24].

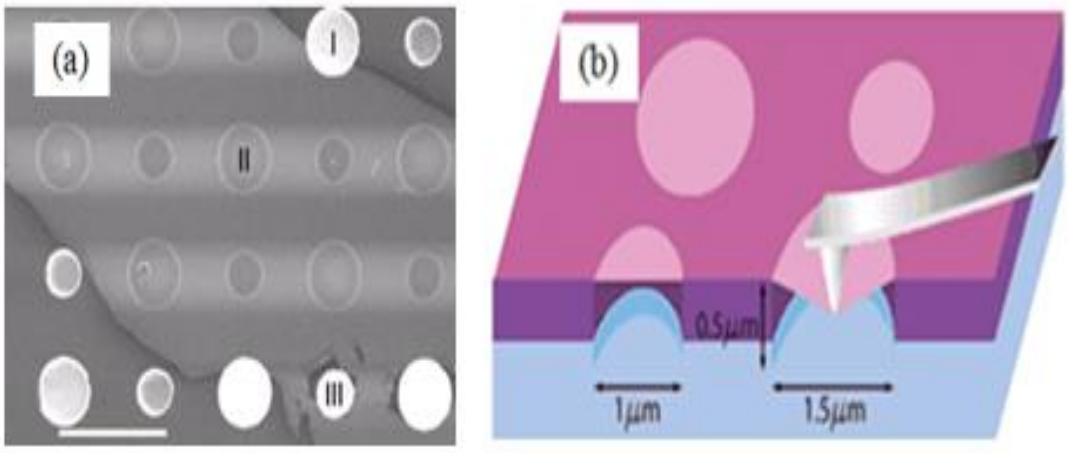

Figure 2.5 (a) Scanning electron micrograph of a large graphene flake spanning an array of circular holes. Scale bar, 3 μm [1]. (b) Schematic of nanoindentation on suspended graphene membrane [1].

2.2.3 Optical Properties

Graphene's unique optical properties produce an atomic monolayer with a high opacity, and showed a measured white light absorbance of 2.3% and a negligible reflectance (<0.1%) [25]. The transmittance of graphene displays a linear dependence on

its thickness [25]. It was reported that monolayer graphene appears to be transparent (Figure 2.6). A 10 nm-thick film has a transmittance of 70% while a 2 nm thick film has an even higher transmittance of 95% [25-27]. The optical transmittance of graphene is expressed as $T= (1+1/2\pi\alpha)^{-2}$ for normal incident light, which depends only on the fine-structure constant $\alpha=2\pi e^2/hc$ (where e is the electron charge, c the light speed, and h the Planck's constant) [28].

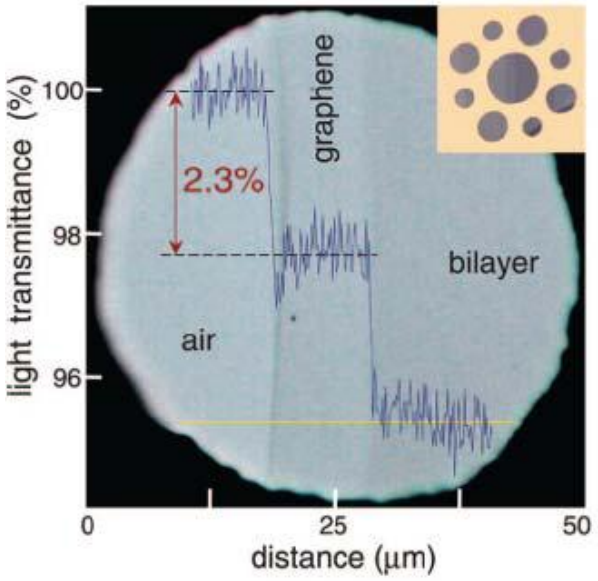

Figure 2.6 Optical micrograph of one- and two-atom thick graphene layers [25].

2.2.4 Thermal Properties

The near-room temperature thermal conductivity of monolayer suspended graphene was measured to be between 3000 to 5000 $Wm^{-1}K^{-1}$ [3]. Silica-supported graphene has a thermal conductivity of 600 $Wm^{-1}K^{-1}$, which is about one order of magnitude lower than that of suspended graphene.[29]. This decrease in thermal conductivity is due to the weak binding force between the graphene layer and the silica plane as well as the large interface-scattering.

2.3 Synthesis of Graphene

Various techniques have been developed to synthesize graphene. These methods can be classified into two categories: the bottom-up and top-down approaches. The bottom-up approach includes the epitaxial growth, chemical vapor deposition (CVD), and organic synthesis of graphene. The top-down approach includes mechanical exfoliation, wet chemical synthesis, and the unzipping of carbon nanotubes.

2.3.1 Epitaxial Growth

Graphene has been synthesized on solid substrates through epitaxial growth. In this process, silicon carbide, which works as the active material, is heated in an ultrahigh vacuum (UHV) to a high temperature in the range of 1000°C to 1500°C [30-32]. Silicon is sublimated, leaving behind a carbon-rich surface. The carbon layers are further graphitized on a metal substrate and ordered into a graphene structure with sp^2 hybridization (Figure 2.7). Therefore, the key factors that influence graphene's thickness are the annealing time and temperature. One major shortcoming of epitaxial growth is that it is difficult to control the thickness of the graphene [33]. Another challenge is that the orientation of the graphene on the substrate surface is varied. The rotation and mismatch of the graphene layers with respect to each other lead to the decoupling of graphene layers and thus influence the electrical conductivity of the resulting material [34]. The quality of graphene can be improved by heating the active substrate at higher temperatures and in argon, achieving a carrier density of ~10^{13} cm^{-2} [35]. Since epitaxial growth graphene is obtained on a silicon carbide substrate and no transfer of the resultant materials is needed, it is promising for the semiconductor industry. However, high temperatures and an ultrahigh vacuum are required for the growth process. Therefore, this method is very expensive and cannot be scalable for commercialization.

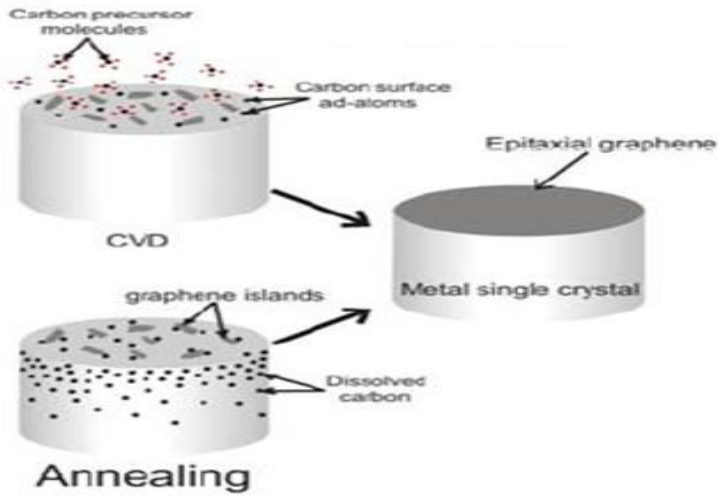

Figure 2.7 Epitaxial graphene growth on metal single crystals [36].

2.3.2 Chemical Vapor Deposition

Chemical vapor deposition (CVD) is used to grow graphene on single crystalline transition metals. It has been reported that graphene can grow on metal films like platinum [37], iridium [38], ruthenium [39, 40] and nickel [41]. Nickel was the first substrate on which single layer graphene was successfully synthesized [42]. In a typical process, a metal substrate, such as nickel, is exposed to hydrocarbon gas at a high temperature and under low pressure, or in an ultra-high vacuum. Carbon atoms diffuse into the metal film at the growth temperature. When cooled down, the carbon atoms tend to become supersaturated and precipitate out of the metal film, forming graphene nanosheets on the surface of the substrate metal. After a chemical treatment of the substrate, the graphene sheets can be removed from the substrate and transferred to the desired substrate. The cooling rate, and the type and concentration of the precursor gas play important roles in determining the thickness and surface quality of the synthesized graphene. One major shortcoming with the nickel substrate is that multi-layer graphene is formed because the growth of graphene is not self-limited. Another shortcoming is that wrinkles and folds are found on the synthesized graphene due to the different coefficient of thermal expansion of graphene and nickel [43].

To solve these problems, substrates with lower carbon solubility, like copper, can be used to synthesize graphene. It is noteworthy that the growth mechanism is different from copper when synthesize graphene on copper [44]. In a typical process, the precursor gas, methane, is catalyzed into C_xH_y when contact with copper. The C_xH_y becomes locally supersaturated on the copper and serves as the nuclei for graphene growth. The nucleus grows into graphene islands. The graphene islands grow bigger until they come into contact with each other. A graphene layer is formed when the copper substrate is fully covered. The scheme is shown in Figure 2.8.

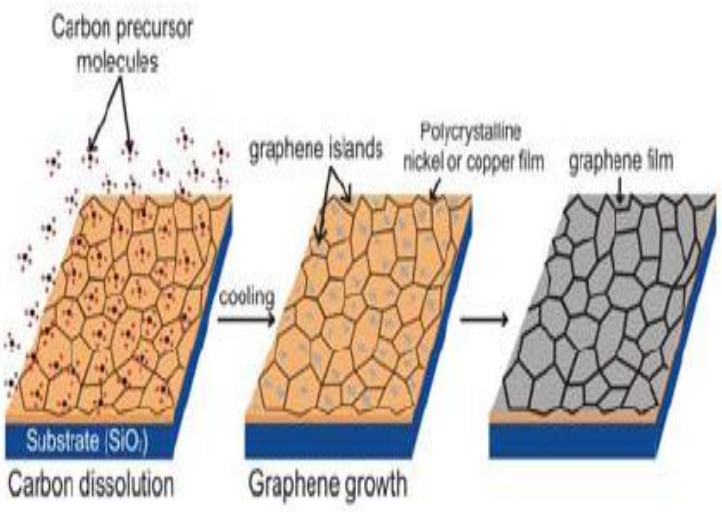

Figure 2.8 The CVD synthesis of large area graphene on copper substrate [36].

The study of this graphene growth mechanism suggests that copper is a promising substrate to produce large-area graphene. One recent breakthrough in roll-to-roll synthesis of 30-inch graphene was achieved by Bae (Figure 2.9) [45]. This method includes three steps beyond CVD synthesis of graphene. Typically, graphene film is attached to polymer supports after synthesis. The copper foil substrate is removed by etching. Large-area graphene is achieved after the thermal release of the polymer support. The fabricated graphene film can be employed as a touch-screen panel component. This application proves the great commercial potential of large area graphene as flexible touch screens and transparent conductive panels in the future.

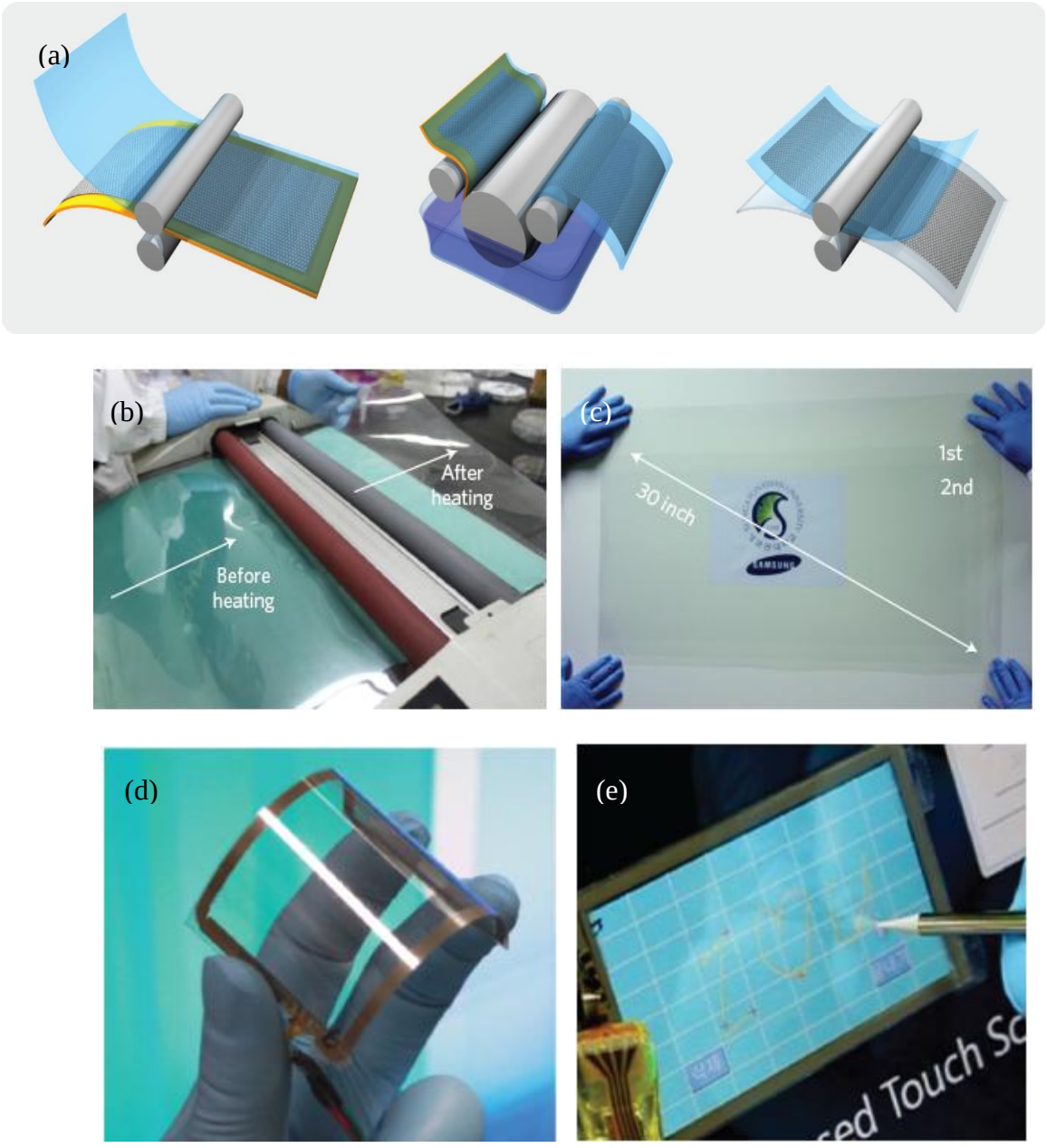

Figure 2.9 (a) Schematic of the roll-based production of graphene films grown on a copper foil. (b) Roll-to-roll transfer of graphene films from a thermal release tape to a PET film. (c) A transparent ultralarge-area graphene film transferred to a 35-inch PET sheet. (d) An assembled graphene/PET touch panel showing outstanding flexibility. (e) A graphene-based touch-screen panel [45].

CVD is promising as a way to synthesize high-quality graphene in a large scale. However, since CVD-synthesized graphene has multiple domains, the domain boundaries hinder the charge mobility and decrease the electrical conductivity of the resulting graphene. Also, the synthesis of high-quality graphene at a low temperature still remains a challenge for this method.

2.3.3 Organic Synthesis

Graphene can be regarded as a 2D pavement composed of many benzene rings. The bottom-up synthesis of larger polycyclic aromatic molecules (PAHs) is regarded as an alternative method for the total synthesis of graphene. In the organic synthesis process, the core precursor molecule is hexabenzocoronene (HBC) with thirteen hexagraphite aromatic rings (Figure 2.10a). Graphene discs with 150 [46] and up to 222 [47] carbon atoms (Figure 2.10b and 2.10c) can be obtained through the oxidative cyclodehydrogenation reaction of HBC with other hexaphenylbenzene derivatives. However, PAHs larger than $C_{42}H_{18}$ have poor solubility in organic solvent. To solve this problem, molecules with long, flexible aliphatic chains are applied to attach on PAHs for a better dispersion [48-50]. The affinity between solvent molecules and the attached molecules overcomes the π-π stacking between different graphene nanosheets. However, this strategy becomes less effective when the graphene size grows larger.

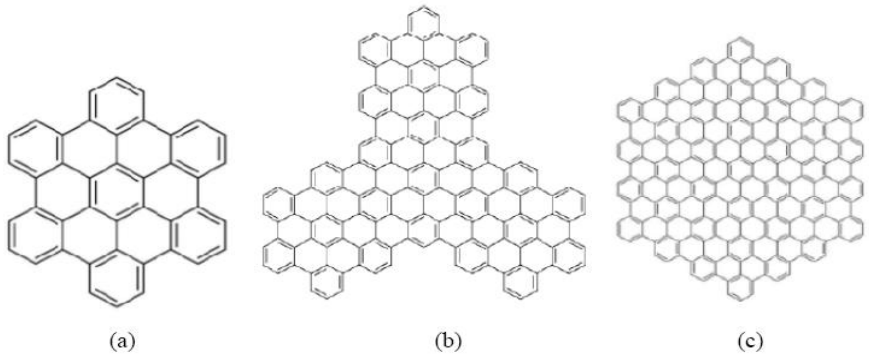

Figure 2.10 Molecular structure of HBC [46] (a) and graphite discs with 150 carbon (b) [46] and 222 carbon (c) [47].

Mullen et al. carried out many experimental studies on the total organic synthesis of graphene [51, 52]. They also successfully synthesized graphene nanoribbons (GNRs) using the same method. Linear GNRs with a width of 12 nm were synthesized via the organic protocol [51]. They also synthesized GNRs on a gold surface [52]. The basic steps for fabricating surface-supported GNRs are shown in Figure 2.11. In a typical process, the halogen element in the precursor monomer is removed during the thermal deposition of the precursor on a gold surface. During the following two steps of thermal activation, the precursor radical undergoes a radical addition reaction and surface-assisted cyclodehydrogenation, resulting in a linear aromatic system.

Though this method shows synthesis versatility; Howere, the poor dispersibility, poor solubility, and difficulties in geometry control hinder the wide application of this method in producing graphene.

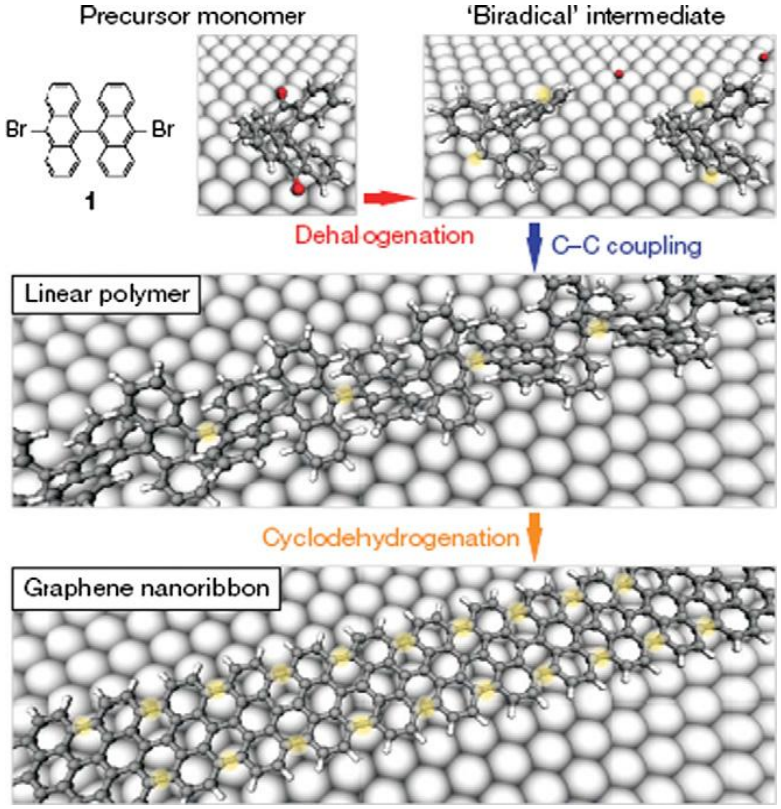

Figure 2.11 Basic steps for surface supported GNRs synthesis. Grey, white, and red balls stand for carbon atom, hydrogen atom and halogen atoms, respectively [52].

2.3.4 Mechanical Exfoliation

According to the study of Zhang and his co-workers, graphene layers have an interlayer energy of ~2 eV/nm^2, and a force with a magnitude of 300 nm/μm^2 is required to exfoliate graphite [53]. Mechanical exfoliation produces graphene sheets from bulk graphite or highly oriented pyrolytic graphite (HOPG) by repeated peeling/exfoliation. This peeling/exfoliation can be achieved with the assistance of an AFM tip [53], scotch tape [19], ultrasonication [54], transfer printing [55], or an electric field [56].

In 1999, Ruoff et al. showed that multiple or even single layers of graphene can be obtained by simple extensive rubbing of a patterned HOPG surface against other flat surfaces [57]. In Kim's group, a well-patterned HOPG block was mounted to a tipless cantilever. Graphene layers of 10 nm thick were transferred onto a SiO_2/Si substrate by controlling the pressure and shearing force of the cantilever [53]. Although these methods fabricated thin samples, no monolayer graphene was produced until 2004, by Geim et al [19, 58].

Geim and his co-workers prepared momolayer graphene for the first time by simply peeling small mesas of graphite with scotch tape repeatedly [11, 24]. Graphite was first etched using oxygen plasma, creating 5 mm-deep mesas. Then the graphite mesas were attached to a fresh wet photoresist by baking. By repeatedly peeling flakes of graphite off the mesas using a scotch tape, thin flakes were left on the photoresist. Single layer graphene with a thickness of 0.5 nm on a SiO_2 surface was observed using AFM (Figure 2.12).

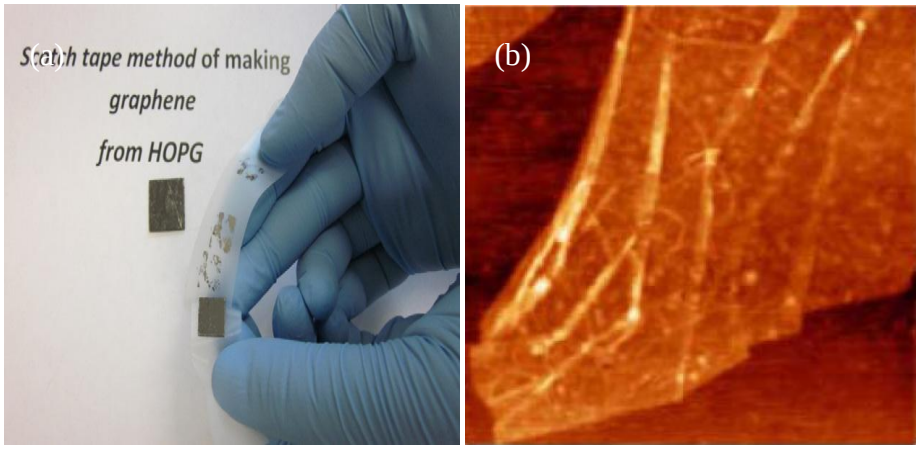

Figure 2.12 (a) Mechanical exfoliation of graphene using scotch tape from HOPG. (b) Single-layer graphene observed by AFM (double-folds single layer graphene with a thickness of 0.8nm) [19].

However, the glue residues left on the sample may influence the observed structure [59] of graphene as well as reduce the carrier mobility [60]. To solve this problem, the exfoliated graphene can be annealed in an argon/hydrogen atmosphere at 300°C for 1 hour to remove the impurities [59]. High electrical currents can be used to remove the impurities as well [61]. The application of a high current through the graphene generates tens of milliwatts of dissipation in the area of a few μm^2, and the impurities are melted away.

Exfoliation of graphite with high voltage has also been investigated [62, 63]. In Sidorov's research, graphite was first cleaved using the scotch tape technique to create a fresh surface [62]. Then the material was placed between two electrodes. It was found that the graphene sheets were loosely bound to the bulk graphite and that these sheets could be removed from the surface by applying a voltage of between 1 and 13 kV. When the voltage was in the range of 3 kV to 5 kV, 1- to 3-layer graphene was obtained. The number of layers tended to increase with increasing voltage. Shukla et al. took advantage of the electrostatic field formed by the migration of sodium ions in a Pyrex substrate when subjected to a voltage of between 1.2 kV and 1.7 kV [63]. Graphite was mounted to

the Pyrex substrate and formed electrostatic bonding with the substrate after the voltage was applied. The bulk graphite could then be cleaved off using the scotch tape technique.

Recently, Ajayan et al. reported a transfer printing process for exfoliating pre-patterned graphene using a gold transfer stamp [55]. In this method, HOPG is patterned by using photolithographic techniques and oxygen-plasma etching. Gold film is deposited onto the HOPG disk. A thermal release tape is used to peel off the gold film together with graphene sheets. Graphene sheets are obtained after releasing them onto the desired substrate and etching off the gold film.

Mechanical exfoliation produces graphene by overcoming the interaction energy of the graphene layers. Since the starting graphite source has a high quality and no extra harm is introduced to the network of graphene layers during the fabrication procedure, this method is regarded as the best method of producing graphene with high electrical and structural quality. One shortcoming of this method is the random size distribution of graphene layers, which ranges from a few microns to a couple of millimeters. Moreover, it is difficult to achieve a mass production of graphene through this method. Thus, this method is limited to a laboratory scale.

2.3.5 Wet Chemical Synthesis

Another typical method of producing graphene from graphite is the exfoliation of chemically intercalated graphite. This method starts with the oxidization of pristine graphite flakes, in which chemical groups are introduced to the surface of graphite layers. The intercalated chemical groups weaken the interlayer Van der Waals force. The resulting graphite oxide is then separated into individual graphene layers by thermal treatment. Graphite oxide can also be exfoliated to produce aqueous colloidal suspensions of graphene oxide (GO) sheets by simple sonication. The GO is further treated by chemical reduction [64, 65] or thermal annealing to restore the properties of graphene [66, 67]. The process of producing graphene through thermal exfoliation and chemical reduction is illustrated in Figure 2.13.

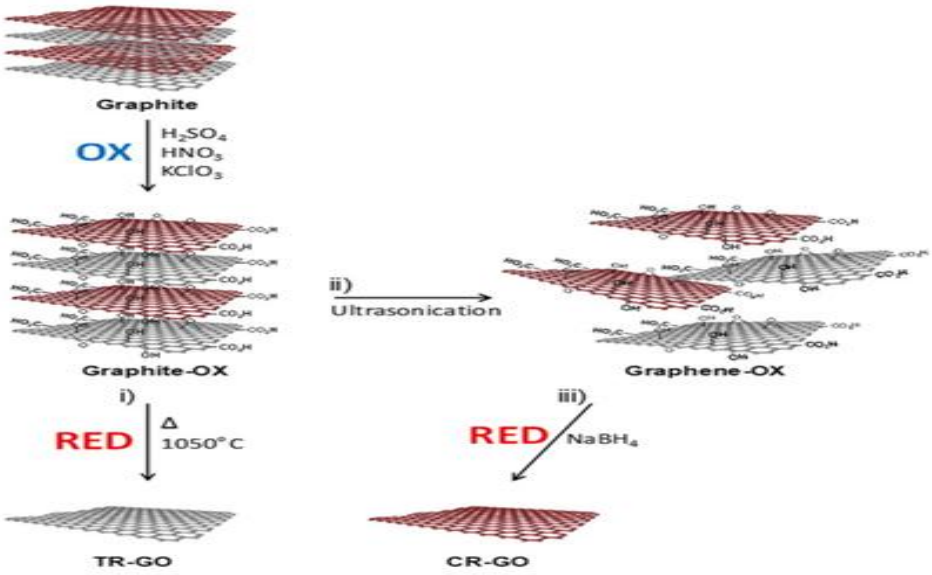

Figure 2.13 The process of producing graphene through thermal reduction and chemical reduction of graphite oxide. "OX," "RED," "TR," and "CR" stand for oxidation, reduction, thermal reduction, and chemical reduction, respectively [68].

In general, graphite oxide can be fabricated by following the Brodie [69], Hummers [70] and Staudenmaier [71] methods.

In the year 1859, Brodie's et al. first developed a method to derive graphite oxide from graphite [72]. An oxidation mixture consisting of fuming nitric acid and potassium chlorate was used to produce modified graphite flakes that composed of hydroxyl, epoxy, and carboxyl groups. The intercalated chemical groups increased the interlayer spacing of the graphite flakes. Many other methods had been developed to produce graphite oxide, all of which nearly rely on strong oxidizing mixtures containing one or more concentrated acids and oxidizing materials [72]. In 1958, Hummer reported a faster method to derive graphite oxide using a mixture of concentrated sulfuric acid, sodium nitrate, and potassium permanganate at 45°C for less than 2 hours [70].

Even though study on graphite oxide has gone on for more than a century, the structure of graphite oxide is still under debate. Currently, the Lerf-Klinowski model is favored and accepted by researchers [73]. Its proposed structure of graphene oxide, which

is supported by solid-state nuclear magnetic resonance (SSNMR) on ^{13}C-labeled graphene oxide, is shown in Figure 2.14. The structure of graphene oxide involves two kinds of regions: aromatic regions with an unoxidized carbon network and regions containing a carbon network bonded to chemical groups. A significant fraction of the functionalized carbon network is bonded to hydroxyl groups or epoxy groups while the minor fractions are bonded to carboxylic groups, ketone groups, or carbonyl groups at the edges of the carbon plane. The functional groups are formed on both sides of the carbon plane [73-77]. Due to the existence of these chemical groups, graphene oxide is very hydrophilic and can form a stable colloid in water.

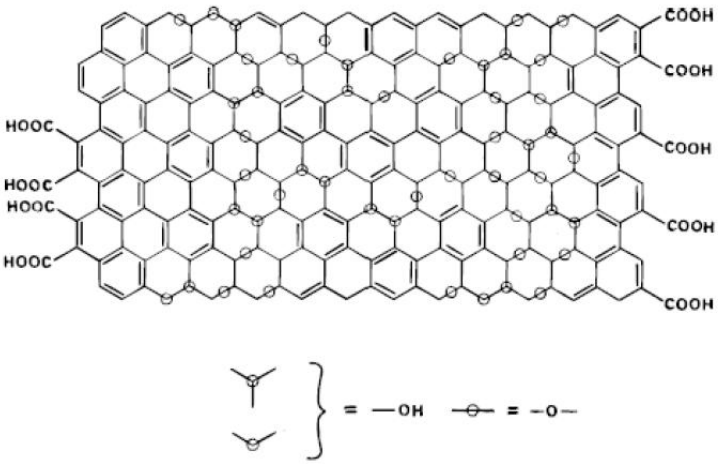

Figure 2.14 Proposed configurations for graphene oxide [73].

Regardless of which method is used to fabricate graphite oxide, after chemical intercalation, it can be separated into individual graphene layers by thermal exfoliation. During this process, the exfoliation of the graphene layers and the removal of the grafted chemical groups occur simultaneously. According to the study of Assay ea al., a fast heating decomposes the intercalated groups into gas (H_2O, CO_2 and CO) and generates a large pressure that overcomes the Van der Waals forces holding the graphene layers together (Figure 2.15) [78]. A high heating rate is required to generate pressure that is large enough to exceed the Van der Waals forces [65, 78, 79].

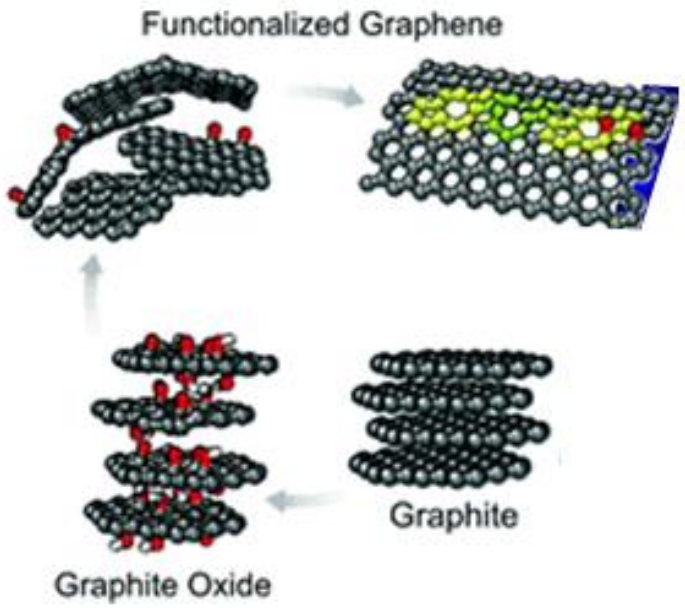

Figure 2.15 Scheme of producing graphene through thermal exfoliation of graphite oxide. (Carbon, oxygen, and hydrogen atoms are shown in gray, red, and white, respectively) [65].

Chen et al. expanded graphite oxide into graphene via a thermal shock at 1050°C and further treated the resultant materials using ultrasonic irradiation [80]. Jang et al. exposed the graphite oxide to an exfoliation temperature lower than 650°C and then subjected the exfoliated graphite to ultrasonication or ball milling [81]. Aksay et al. used this method to produce exfoliated graphite oxide platelets [65, 78, 79]. Based on a characterization using AFM, they claimed that 80% of the observed flakes were single layers.

Besides in an ultrahigh vacuum, the thermal exfoliation of graphite oxide can be carried out in various atmospheres like hydrogen and argon. Argon is used to prevent the GO from contamination during the reduction procedure. With the addition of hydrogen, the reduction of GO was further improved, which was observed through a higher C/O ratio [82]. Simulation results indicate that the existence of hydrogen can enhance the efficiency of reduction by 3.3-7.4%. This is due to the fact that hydrogen atoms may

transform the carbonyls [83] and epoxies [84] into hydroxyls, which will decompose into water when heated [85].

Thermal exfoliation of graphite oxide can produce highly reduced graphene through the control of the heating temperature, gas atmosphere, and duration. However, the removal of oxygen-containing groups leads to a mass loss of 30% and leaves behind vacancies and defects which significantly influence the mechanical and electrical properties of produced graphene.

Chemical reduction of graphene oxide is widely used to restore the properties of graphene since most of these approaches are simple and the price of the reducing agents is low. Various kinds of reducing agents are studied for GO reduction including hydrazine (N_2H_4), sodium borohydride ($NaBH_4$), iron/aluminum powder, ascorbic acid, hydroquinone, alcohol, and sodium/potassium hydroxide [85].

The most commonly used agent is hydrazine since it produces highly reduced GO at low temperatures and does not react with water. Ruoff et al. first reduced GO using hydrazine and proposed its possible reducing mechanism [86]. As shown in Figure 2.16, the epoxy ring is opened through the abstraction of hydrogen from hydrazine, forming hydrazino alcohol. Then each hydrazino alcohol molecule transfers one hydrogen atom to the hydroxyl group and releases one water molecule. The derivates undergo thermal elimination of diimide to form a double bond. This approach primarily removes the hydroxyl and epoxy groups but leaves others, such as carboxyl and ketone groups, on the edge.

Moreover, X-ray photoelectron spectroscopy results show that side reactions may occur during the reduction process, resulting in the formation of C-N groups at the surface of the reduced graphene which leaded to a low electrical conductivity of ~2000 S/m [86]. Post-thermal annealing was used to remove the C-N groups and other remaining functional groups, resulting in a high electrical conductivity in the range of 20,000 to 50,000 S/m [87].

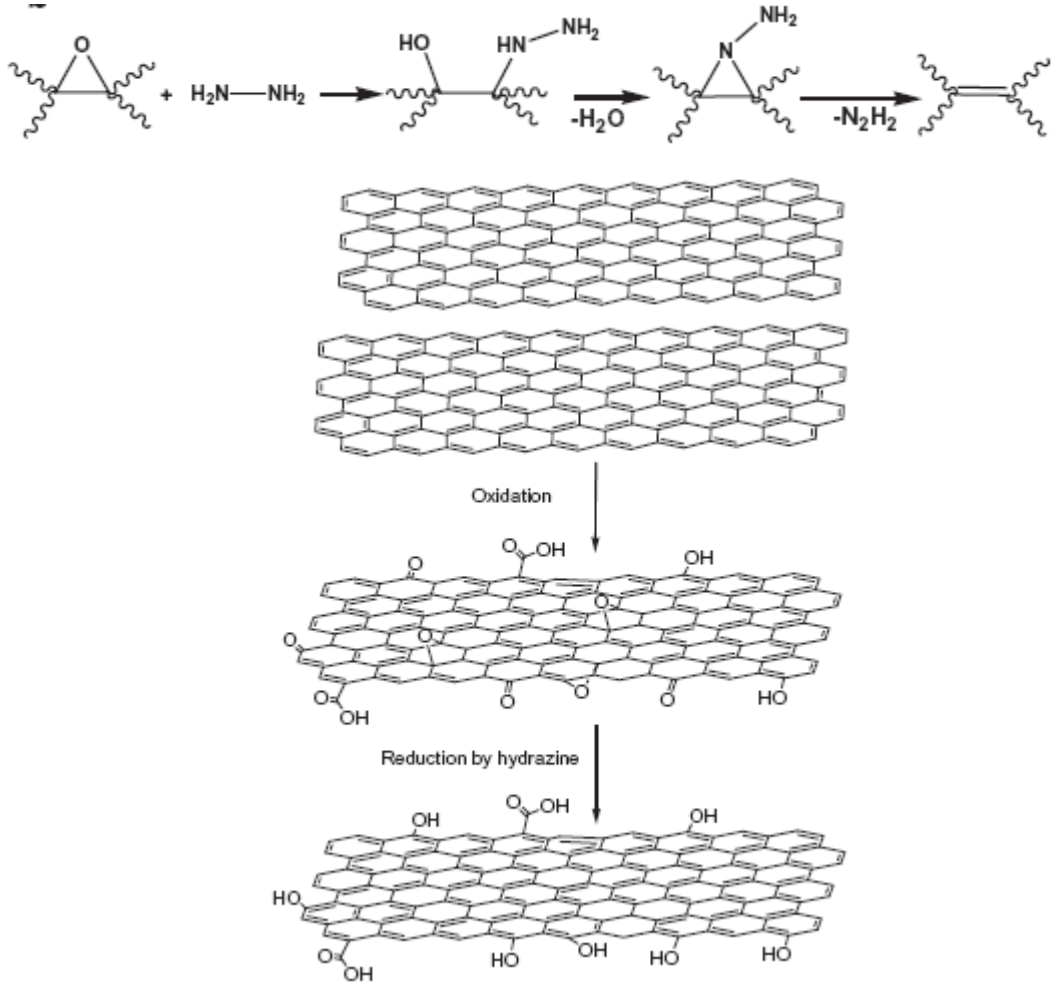

Figure 2.16 (a) A proposed reaction mechanism for epoxy reduction by hydrazine [86]. (b) Oxidation of graphite to graphene oxide and reduction to reduced graphene oxide [33].

$NaBH_4$ is a widely used reduction agent, which generally removes epoxy groups, but cannot reduce hydroxyl groups or carboxyl groups. Therefore, graphene reduced by $NaBH_4$ typically showed a low electrical conductivity, like 45 S/m [88]. A multi-step reduction procedure is used to remove the remaining functional groups on GO (Figure 2.17). Sulfuric acid and thermal annealing can be used to remove hydroxyl and carboxyl groups, respectively, and the reduced graphene has an electrical conductivity of 20200 S/m [89].

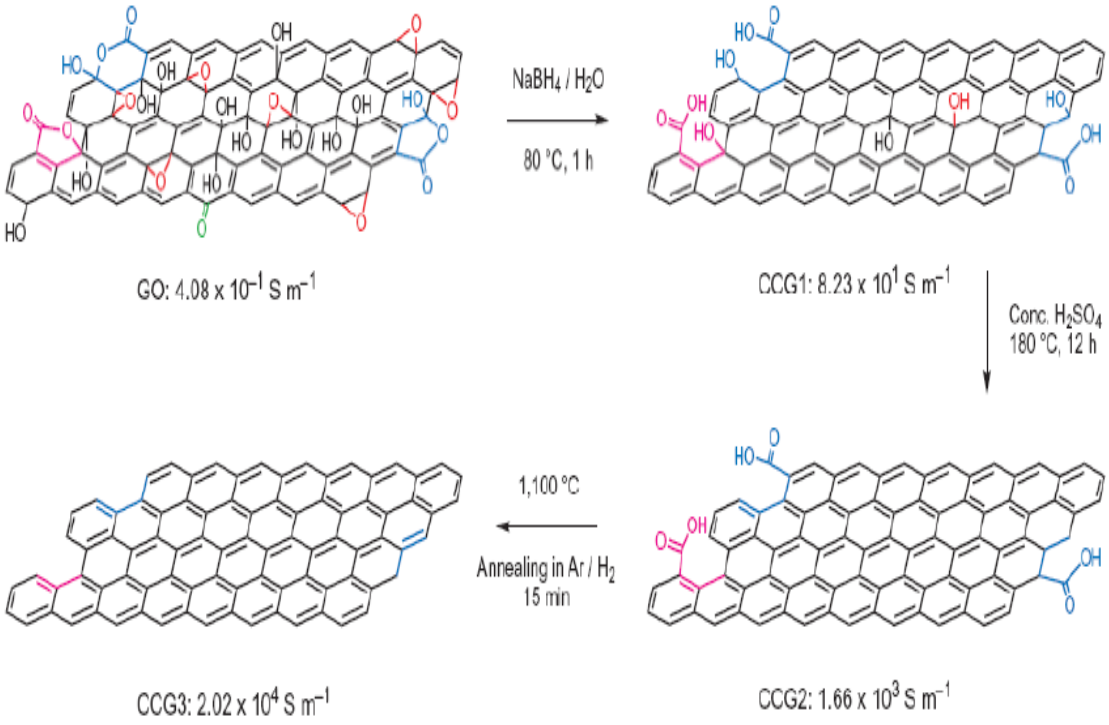

Figure 2.17 The scheme of multi-step reduction of graphene oxide with $NaBH_4$ [89].

Since hydrazine-based chemicals and $NaBH_4$ are toxic, eco-friendly reducing agents for the production of graphene have been explored. Iron can be used to reduce graphite oxide with the assistant of hydrochloric acid [90]. Iron powders react with H^+ to produce Fe^{2+} which is adsorbed on the surface of Fe particles. According to the zeta potential test, GO sheets possess negative charges in a solution (-37 mV), so positively charged Fe particles are absorbed by GO sheets. As a result, Fe particles that closely covered the surface of GO reduced GO through the transport of electrons from Fe/Fe^{2+} to GO sheets. The mechanisms can be expressed as follows [90]:

$$Fe \rightarrow Fe^{2+} + 2e^-$$

$$GO + H^+ + e^- \rightarrow \text{reduced GO} + H_2O$$

Since iron is cheap, rich on the earth, and eco-friendly, it has potential to be used in the mass production of reduced GO (rGO). Other metals such as aluminum and zinc

can be used to reduce GO with similar mechanisms, and the resulting electrical conductivity varies from 2100 to 15000 S/m [90-92].

The reduced graphene oxide sheets tend to become less hydrophilic and precipitate due to the removal of the hydrophilic groups [86]. To produce homogeneous rGO suspensions, the reduction can be carried out with the presence of a polymer or surfactant [93, 94]. Stankovich and his co-workers reduced poly(sodium 4-styrenesulfonate) (PSS)-wrapped GO with hydrazine, becoming the first to prepare stable aqueous dispersions of rGO [93]. Jay used sodium dodecylbenzenesulfonate (SDBS) as a surfactant to wrap GO [95]. After being reduced with hydrazine, the resulting graphene sheets were modified with aryl diazonium salt, making the graphene sheets stable in organic solvent like dimethylformamide, N,N'-dimethylacetamide, and N-methyl-2-pyrrolidone.

Colloidal suspensions of graphene sheets prepared without the help of a surfactant have been reported by Li et al. [96]. By raising the pH value of a graphite oxide suspension to 10, the charge density on the resulting graphene sheets was maximized by converting neutral carboxylic groups to negatively charged carboxylate groups. The electrostatic repulsion forces were responsible for the stabilization of the aqueous suspension. The procedure is shown in Figure 2.18. The graphene films prepared by using this method showed an electrical conductivity of 7200 S/m [96].

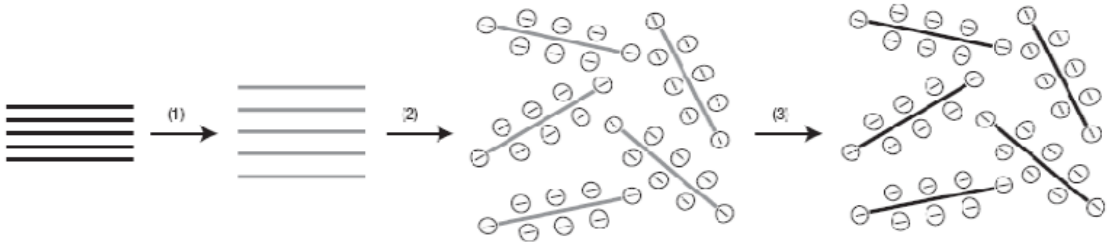

Figure 2.18 Scheme showing the chemical route of the synthesis of aqueous graphene dispersions. 1. Oxidation of graphite to graphite oxide with increased interlayer distance. 2. Exfoliation of graphite oxide in water by sonication to obtain graphene oxide colloids

that are stabilized by electrostatic repulsion. 3. Conversion of graphene oxide to graphene through reduction with hydrazine [96].

Electrical conductivity of rGO is an important indicator of the reduction level and the restoration level of the sp^2 network. The electrical conductivities of rGO produced by different methods are summarized in Table 2.1.

Table 2.1 Electrical conductivities of rGO prepared by different approaches

Sample	Forms	Conductivity (S/m)	Ref.
GO/N_2H_4	Film	9,960	[97]
GO/N_2H_4	Paper	1,700	[98]
150ºC	Paper	16,000	[98]
GO/$N_2H_4 \cdot H_2O$	Pellet	2,420	[86]
	Film	11,800	[87]
	Film	35,000	[87]
GO/phenylhydrazine	Film	4,770	[99]
150ºC	Film	20,950	[99]
GO/N_2H_4+ $NaBH_4$	Film	1,250	[64]
GO/$NaBH_4$	Film	45	[88]
H_2SO_4, 150ºC	Pellet	1,660	[89]
H_2/Ar, 1100ºC	Pellet	20,200	[89]
GO/Fe	Film	2,300	[90]
GO/Zn	Film	2,100	[91]
GO/Al	Film	15,000	[92]
GO/N_2H_4+KOH	Paper	690	[100]
GO/HI &AcOH	Pellet	30,400	[101]
GO/1100ºC	Film	10,000	[67]
GO/H_2/Ar/1050ºC	Single layer	100,000	[102]
GO/Ar/1900ºC	Pellet	56,500	[103]
GO/Flash	Film	1,000	[104]
GO/Microwave	Paper	200	[105]
GO/Microwave	Pellet	274	[106]

2.3.6 Un-zipping Carbon Nanotubes (CNTs)

Single-layer graphene is intrinsically a semimetal with a zero band gap which may hinder its application in the semiconductor industry [107-109]. Graphene

nanoribbons (GNRs) are thin strips of single-layer graphene which pose certain electrical properties depending on their width. Recently, Dai's group found that GNRs which are narrower than 20 nm showed a finite energy band gap [36, 110].

GNRs have been synthesized using a variety of methods, including mechanical cleavage lithography, etching, and chemical stripping [110-114]. One of the method is the unzipping of carbon nanotubes. Multi-walled carbon nanotubes (MWNTs) have been successfully opened up by using potassium permanganate oxidation and lithium and ammonia reactions, respectively (Figure 2.19a) [115, 116]. Dai et al. also reported the plasma etching of carbon nanotubes which are partially embedded in polymer film (Figure 2.19b) [117]. Recently, GNRs were fabricated by thermal expansion of encapsulated molecular nitrogen in MWNTs [114]. The shortcoming of this method is that the polydispersity of the carbon nanotube leads to varying width, thickness and chiralities [36].

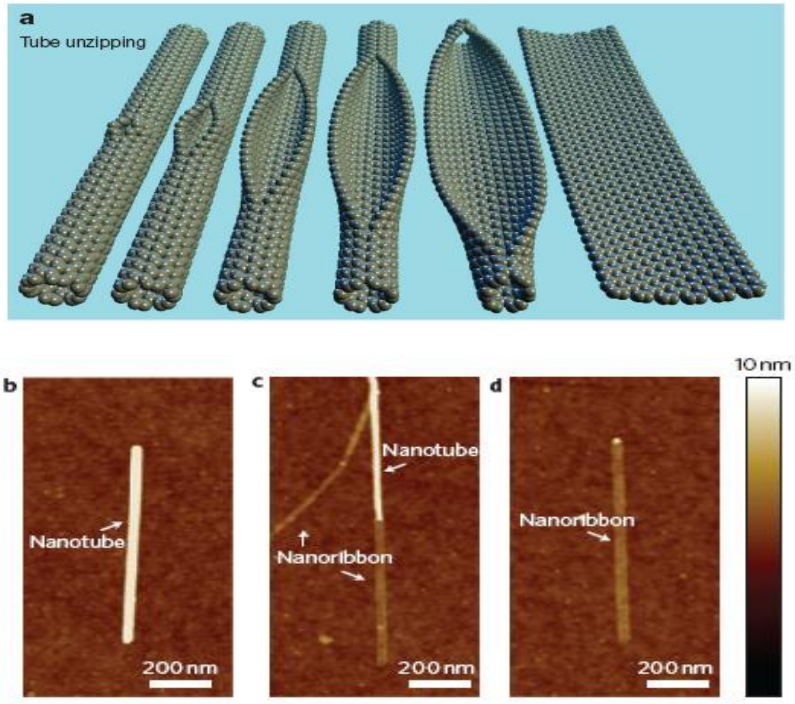

Figure 2.19 (a) Scheme of the gradual unzipping of one wall of a carbon nanotube to form a nanoribbon [115]. AFM images of (b) pristine, (c) partially and (d) fully unzipped nanotubes, respectively [118].

2.3.7 Summary

Graphene can be prepared by various methods as point out in Table 2.2 by comparing the advantages and disadvantages. Challenges remain in producing high quality graphene on a large scale and in a cost-effective manner. Recent developments, especially in the CVD growth of graphene on metal substrates, showed exceptional potential for the commercialization of graphene. The CVD-synthesized graphene typically shows multiple domains, which significantly limits its performance due to low electrical conductivity. Further improvements of CVD-synthesized high quality graphene at low temperatures, and with an easy transfer process, will allow for broader applications of graphene. A promising approach for the mass production of graphene at low cost is the wet chemical method. The wide application of chemically reduced GO is limited by the toxicity of the reducing agent. The reduction level of thermally reduced GO can be controlled through adjusting the heating temperature, gas atmosphere and duration. The combination of chemical reduction with thermal reduction is promising in order to achieve a highly reduced GO.

Table 2.2 Comparison of various methods for preparation of graphene

	Method	Advantages	Disadvantages
Bottom-up	CVD	Large area	Low electrical conductivity
	Epitaxial growth	Few defects	Low yield, small area, high cost
	Organic synthesis	Few defects, scalability	Poor solubility, small area, high cost
Top-down	Mechanical exfoliation	High quality, simple process	Poor scalability, small area
	Wet chemical synthesis	Low cost, high yield	A lot of defects
	Unzipping of CNTs	Controllable band gap	Low yield, poor scalability

2.4 Functionalization of Graphene with Nanoparticles

During the last few decades, the synthesis of inorganic nanoparticles (NPs) was well established. Inorganic nanoparticles are of great importance in many applications such as surface-enhanced Raman scattering (SERS), catalysis, microelctronics, photovoltaic cells, display devices, energy storage, and medical or biological applications [119-121]. Recently, various kinds of nanoparticles have been successfully incorporated with graphene for new functionalities and improved performance [122-124].

The grafted nanoparticles can be classified into two classes: metallic nanoparticles and non-metallic nanoparticles. Especially, the metallic nanoparticles can be further classified into two catalogues: metal and metal compound. Metal nanoparticles include Au, Ag, Pt and Pd. Metal compounds are the oxides, hydroxides, sulfides, nitride, and inorganic salts of metals. The typical non-metallic nanoparticles are carbon materials, S, Si, SiO_2, etc.

The fabrication methods of graphene/NPs hybrids can be generally classified as *in situ* hybridization and *ex situ* hybridization. The details of these two methods are discussed in section 2.4.1 and 2.4.2.

2.4.1 In situ Hybridization

Among these two methods, *in situ* hybridization is more widely used for the fabrication of graphene/NPs hybrids. The common precursors of graphene and NPs are GO and metal salts, respectively. Several methods were explored for the synthesis of graphene/NPs hybrids, including solution based reduction, sol-gel/hydrogel synthesis, hydrothermal/solvothermal synthesis, electrochemical deposition and electroless deposition, and chemical vapor deposition (CVD) [11].

Solution-based reduction method

In the typical procedure, the metal salts are mixed with GO and then converted into a corresponding metal or metal oxide. Graphene/NPs are formed when GO is

reduced. The commonly used reducing agents are sodium borohydride ($NaBH_4$) [125], ethylene glycol (EG) [126], and ascorbic acid [127]. For example, Zn^{2+} ions were added into a solution of GO and converted into ZnO nanoparticles with the addition of $NaBH_4$ and NaOH [125]. A Pt and Pt-based alloy/rGO hybrid was synthesized using a similar method, in which K_2PtCl_4 or K_2PdCl_4 and GO solution were mixed with EG aqueous solution. Both of the components were reduced by EG, forming corresponding hybrids (Figure 2.20) [126, 128]. A Pt/Pd alloy/graphene hybrid was fabricated by reducing the Pd and Pt precursors by formic acid and ascorbic acid, respectively [127].

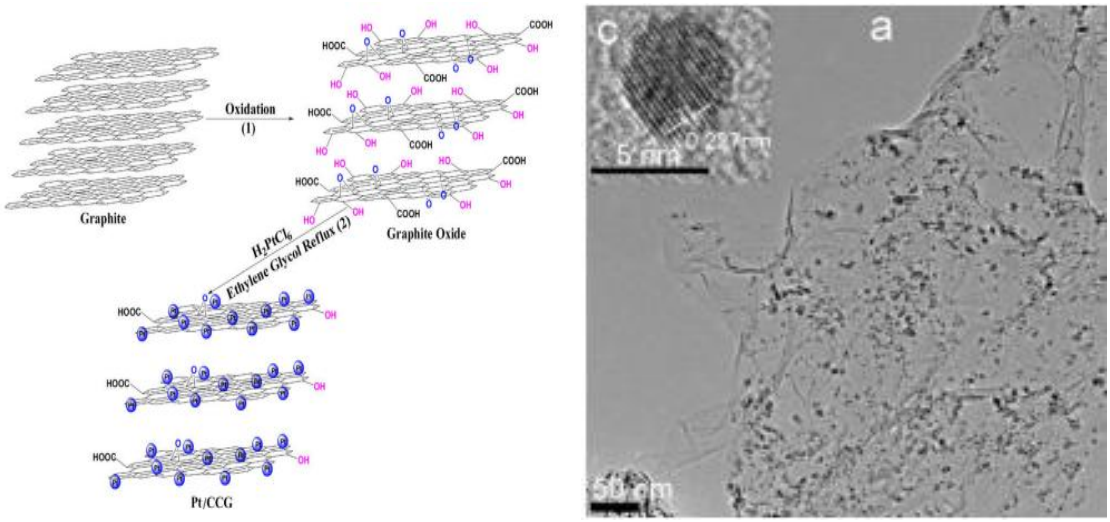

Figure 2.20 (a) Scheme shows the formation of Pt NPs/ rGO hybrid. (b) TEM images of the Pt/rGO hybrid [126].

UV-visible light irradiation is used as an alternative method for the fabrication of NPs/rGO hybrid. Semiconductors with a large band gap, such as TiO_2 and ZnO, are photocatalytically active under UV irradiation. When irradiated, electrons are generated and transferred to GO, which can be used for the reduction of GO (Figure 2.21) [129]. It is reported that TiO_2 is a mild reducing agent at a neutral pH [130]. A TiO_2/graphene hybrid can be fabricated by simply mixing TiO_2 particles with GO colloids, followed by ultraviolet irradiation [131]. A similar strategy was applied to hybridize TiO_2 [132, 133], ZnO [134, 135] WO_2 [136], and Au with graphene. Since the photocatalytic reduction is triggered by light irradiation, the process is feasible and controllable.

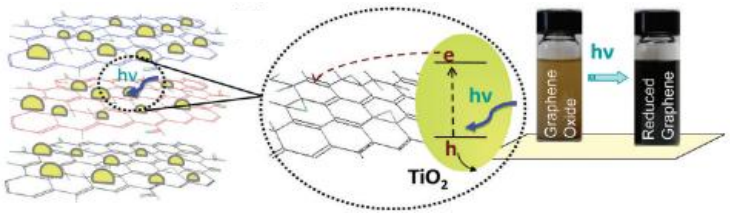

Figure 2.21 Reduction of GO through light irritation of TiO_2 [129].

Sol-gel/ hydrogel methods

In addition to the solution system, the synthesis of a NPs/graphene hybrid can be carried out in a sol-gel/ hydrogel system. Typically, metal alkoxides or chlorides work as precursors and undergo hydrolysis and polycondensation reactions during the procedure. Take the fabrication of Fe_3O_4 NPs/graphene hybrid as an example (Figure 2.22) [137]. The ferrous ions Fe^{2+} are anchored on the surface of GO through electrostatic interactions. The Fe^{2+} ions are then oxidized into Fe^{3+} ions by the oxygen-containing groups of GO. The Fe^{3+} ions underwent hydrolysis and formed α-FeCOOH or Fe_3O_4 NPs, depending on different pH values. The GO was reduced simultaneously by the electrons transferred from the Fe^{2+} ions. A 3D macroporous frame was formed when the NPs/graphene networks interconnected through hydrophobic and π-π stacking interactions. This method was also used to fabricate TiO_2 [138, 139], SiO_2 [140], RuO_2[141], and $Li_3V_2(PO_4)_3$ [142] nanoparticles on graphene sheets. The advantage of this method is that it is a cheap and low-temperature technique.

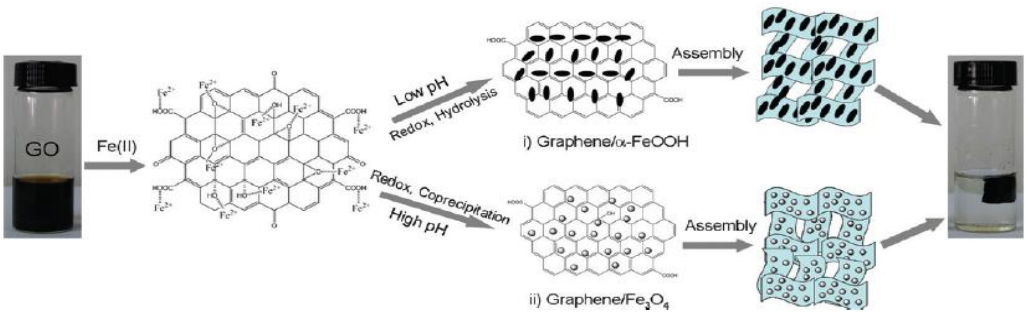

Figure 2.22 Schematic illustration of the formation mechanism of the graphene/iron oxide nanostructure [137].

Hydrothermal/ solvothermal synthesis

Hydrothermal/ solvothermal synthesis is a powerful tool used to synthesize inorganic crystals in solution at high-temperature and high vapor pressures. The crystal growth occurs in a steel pressure vessel called an autoclave, where a temperature gradient is applied. Since the synthesis process is carried out at a high temperature for a long time, GO is reduced without the assistance of a reducing agent. Liu et al. used a facile on-step method to produce CdS/graphene hybrid in DMSO at 180ºC (Figure 2.23) [143]. The thermal reduction of GO occurred at a high temperature with the assistance of H_2S released from DMSO. The CdS quantum dots were formed simultaneously by heating the precursor, $Cd(CH_3COO)_2$. Besides CdS [95], ZnS [144] and MoS_2 [145], metal oxide nanoparticles like ZnO [146], TiO_2 [147], Fe_3O_4 [148], SnO_2 [149], Co_3O_4 [150] and Bi_2O_3 [151], can also form on GO or rGO surface through hydrothermal/solvothermal methods. The advantage of this method is that the process can give rise to nanostructures with high crystallinity without the need of post-annealing.

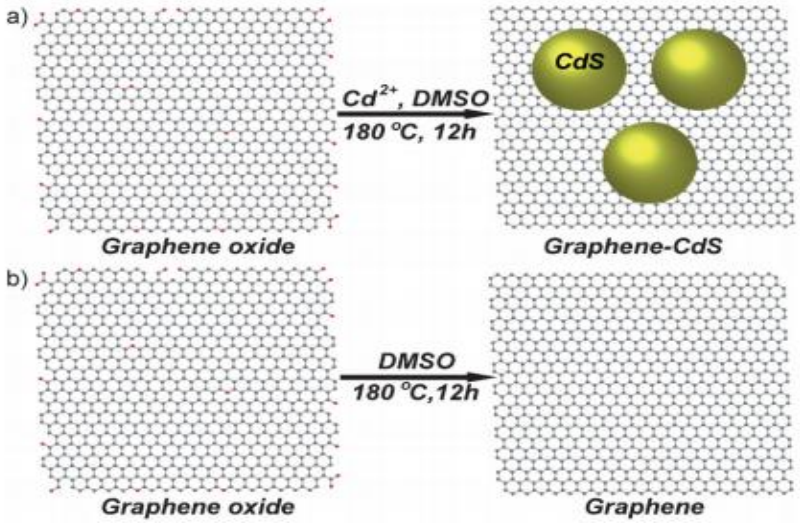

Figure 2.23 (a) Scheme of the one-step synthesis of CdS/graphene. (b) Scheme of the solvothermal reduction of GO to graphene in DMSO [143].

Electrochemical deposition

The direct electrochemical deposition approach has been paid considerable attention due to three reasons: it is simple, it has no contamination of the synthesized materials, and it does not require a post-synthesis transfer of materials [11, 152]. Currently, electrochemical deposition has been widely used to fabricate NPs/graphene nanostructure. Typically, two steps are sequentially carried out: firstly, graphene nanosheets are assembled on the electrode; then the electrochemical synthesis is performed by immersing the graphene-coated electrode in an electrolyte solution containing a metallic precursor. Metal nanoparticles such as Au [153-155] and Pt [156, 157] have successfully deposited on graphene nanosheets under proper conditions.

Through electrochemical deposition, metal oxides have also been deposited on the graphene-based substrates. Recent papers have reported that Cu_2O [158], MnO_2 [159] and CdSe [160] have been electrochemically deposited on an rGO-coated electrode. For example, Zhang's group proposed the electrochemical deposition of Cu_2O on an rGO-PET electrode [158]. In their study, GO was spin-coated on the terephthalate (PET) film that was modified by 3-aminopropyltriethoxysilane (APTES). The rGO-PET electrode was produced by the reduction of GO film in hydrazine vapor. Then Cu_2O was deposited at -0.4 V via reduction of Cu^{2+} ions. By adjusting the pH of the solution, p-type and n-type Cu_2O was formed.

Chemical vapor deposition (CVD)

Chemical Vapor Deposition (CVD) is a method to produce high-purity solid materials on a substrate surface by chemical reactions, which occur during the gaseous flow over a substrate surface [11]. The advantages of CVD include low cost, controllable reaction and high deposition rate. Currently, CVD has been used to obtain ZnO nanorods [161], ZnS nanowire [162] and CdSe nanoparticles [163] on the substrates covered by graphene nanosheets. It has been reported that crystallized ZnO having various morphologies, were grown on graphene nanosheets substrate under different reaction temperatures. Kim et al. studied a hybrid device composed of ZnS nanowire and Te-doped ZnS nanowire on multilayer graphene films. They demonstrated that this device

exhibited blue-green and blue emission, which made it a promising candidate for future electroluminescent devices [162].

2.4.2 Ex situ Hybridization

In the *ex situ* hybridization, graphene nanosheets are mixed with the pre-synthesized nanoparticles for manufacturing the hierarchical nanostructure. To achieve the NPs/graphene nanostructures, linking agents are applied to facilitate the attachment of NPs onto graphene through covalent or noncovalent interactions (π-π stacking, electrostatic interactions, Van der Waals force, and hydrogen bonding) [11]. The solubility of the NPs and graphene in various solvents are important for the hybridization, therefore surface modification is required for both of the components. Since the NPs are pre-synthesized, there is a better shape, size distribution and loading amount control of the grafted NPs when compared with the *in situ* hybridization method.

Covalent interaction

In the covalent interaction, graphene oxide is preferred for the incorporation of NPs since there are different types of functional groups on graphene oxide. The hydrophobic nature and chemical inertness of graphene restricts the process. Zhang et al. reported that Fe_3O_4 NPs modified with 2,3-dimercaptosuccinnic acid (DMSA) could graft onto GO that was modified with polyetheylenimine (PEI) by the amide bond forming between the COOH groups of DMSA and amine groups of PEI [164].

The covalent interaction can be applied to the fabrication of graphene/non-metallic nanoparticles hybrids as well. Zhang et al. covalently synthesized a C_{60}/graphene hybrid through the condensation reaction between pyrrolidine fullerene and acyl-chloride functionalized graphene oxide [165, 166] (Figure 2.24). Recently, our group successfully functionalized the graphene oxide by fullerene insertion and chemical reaction through the Fisher esterification between the hydroxyl groups on graphene oxide and the carboxyl groups on (1,2-methanofullerene C_{60})-61-carboxylic acid [167]. The GO/CNTs hybrid

was also formed through the reaction between the animated CNTs and the acid chloride-activated GO [168].

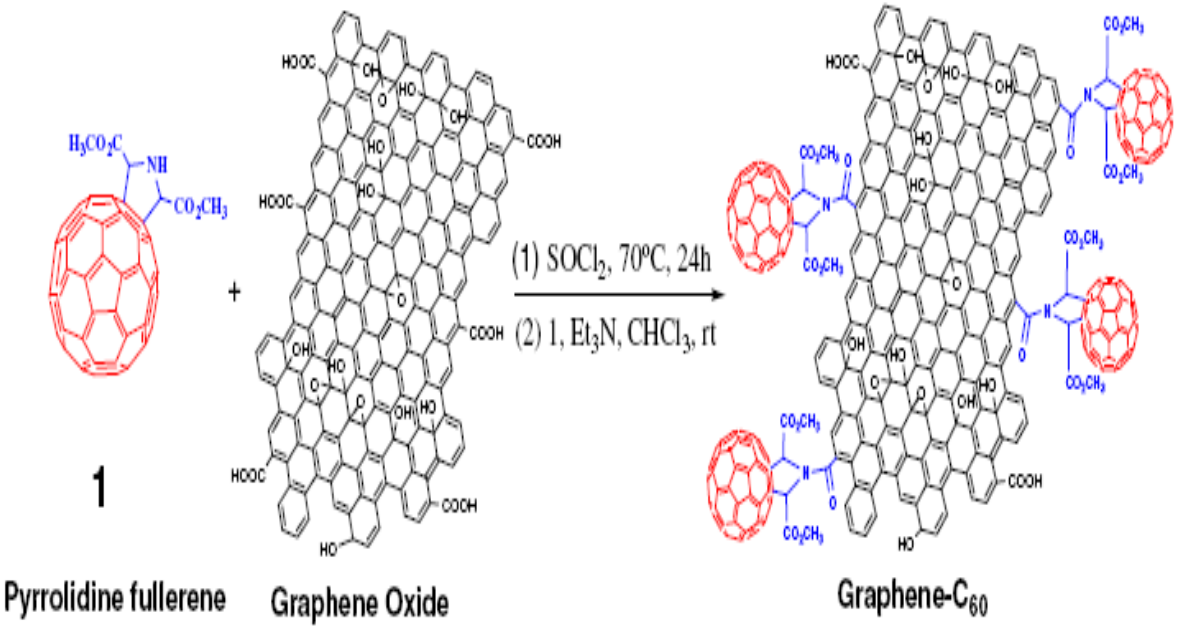

Figure 2.24 Covalent synthesization of C_{60}/graphene hybrid [165].

Noncovalent interaction

In the noncovalent interactions, π-π stacking, electrostatic interactions, Van der Waals force, and hydrogen bonding are used to produce graphene/NPs hybrids. Among these methods, π-π stacking and electrostatic interaction are commonly used for the fabrication [169, 170].

Generally, bridging molecules are needed for the fabrication of NPs/ graphene hybrid through π-π stacking. Typically, the bridging molecules include two parts. One part contains aromatic structures which are used to attach onto graphene and the other part is used to connect onto the NPs through the thiol, amine or acid groups [11]. Molecules like 2-mercaptopyridine, benzyl mercaptan, and bovine serum albumin (BSA) protein, were used to connect graphene and Au, CdSe, and Ag NPs, respectively. Carbon

materials, like fullerene and carbon nanotubes, contain many aromatic regions, which can directly graft onto graphene planes through π-π stacking without the assistant of bridging molecules. Kim and his co-workers assembled fullerene wires onto rGO through π-π stacking by employing a simple liquid-liquid interfacial precipitation method [169]. The GO/CNTs hybrid can be fabricated by filtration of the aqueous dispersion of GO and CNTs (Figure 2.25) [171].

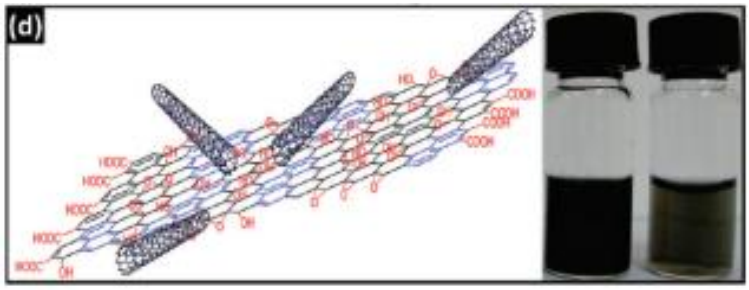

Figure 2.25 Functionalization of graphene oxide with carbon nanotubes through π-π stacking [171].

Electrostatic interaction is another widely used method for the preparation of the NPs/graphene hybrids. The graphite oxide, or reduced graphene oxide, can take negative charges by adjusting the pH value of their solution. Thus, positively charged nanoparticles can be anchored onto the plane of graphene through electrostatic interaction. As reported, positive charges were introduced onto SiO_2 or Co_3O_4 by mixing with minopropyltrimethoxysilane (APS) [170, 172]. The positively charged nanoparticles could be successfully wrapped by negatively charged GO (Figure 2.26). Positive charges can be assembled onto GO or rGO by coating with poly(diallyldimethyl ammonium chloride) (PDDA). After modification, negatively charged Au NPs and CdSe quantum dots can be effectively grafted onto GO and rGO, respectively [173, 174].

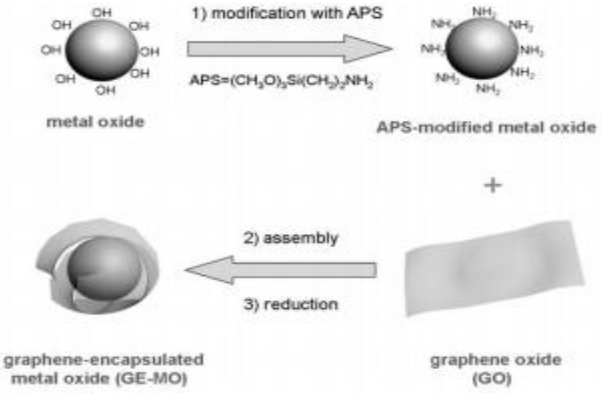

Figure 2.26 Schematic illustration of fabrication of graphene-encapsulated metal oxide [170].

2.5 Applications of Nanoparticle Functionalized Graphene

2.5.1 Lithium Ion Batteries

Lithium ion batteries (LIB) have received considerable attention as an alternative energy source due to their rechargeable features and longer cycle life. The performance of LIB mostly depends on the properties of the cathode and anode materials. Graphene has been a promising candidate as an anode material since it has unique characteristics, including high electrical conductivity, large surface to volume ratio and chemical stability. However, graphene nanosheets are easy to stack into multilayers, thus decreasing the surface to volume ratio. NPs/graphene nanostructure not only limit the aggregation of graphene, but also enhance the capacity of lithium storage. Currently, various nanomaterials of oxides, hydroxides and chalcogenides, such as Fe_3O_4 [175-177], Mn_3O_4 [178], CuO [179, 180], Co_3O_4 [181-183], TiO_2 [139, 184, 185], CoO [181, 186], Fe_2O_3 [187, 188], MoS_2 [189], and SnO_2 [149, 190, 191], have been incorporated into graphene as anode materials. These NPs/graphene nanostructures showed large capacity as well as excellent cycling performances.

NPs/graphene nanostructures have also been used as cathode materials for LIBs. $LiFePO_4$ [192, 193], $Li_3V_2(PO4)_3$ nanoparticles [142], $LiNi_{1/3}Co_{1/3}Mn_{1/2}O_2$ nanoparticles

[194] have been anchored on graphene nanosheets as a promising cathode material for LIBs. Apart from graphene-metal oxide nanostructures, graphene-carbon nanotube and graphene-fullerene hybrids have also been used as electrodes for LIBs [195]. It has been found that the energy storage property of graphene nanosheets electrode can be improved by mixing with carbon nanotubes or fullerene.

2.5.2 Supercapacitors

Supercapacitor is another type of electrochemical storage device which has been widely applied in heavy vehicles, portable media players and so on. Compared with batteries, supercapacitors provide a higher power density (10 kW kg^{-1}), a faster charge ability, and a longer cycling life. In terms of working mechanisms, supercapacitors can be divided into two types: electrical double layer capacitor (EDLC) and pseudo-capacitor. These devices store energy via electrostatistic processes, which describes charge accumulation at electrode interface. Therefore materials with good conductivity and large surface areas are desired in such devices. CNTs, carbon nanofibers and graphene sheets can beneficially provide large specific areas and good conductivity. Moreover, low cost and mass production also make them ideal for supercapacitors. The other type of supercapacitor, pseudo-capacitor, is based on fast redox reactions occurring on the electrode interface. In such devices, metal oxides and conducting polymers are commonly used electrode materials. However, their applications are limited due to the high cost and low conductivity. Therefore, the combination of graphene derivatives and metal oxides or polymers is a competitive choice to produce electrodes for supercapacitors.

Currently, various metal oxides, such as ZnO [196], SnO_2 [197], Co_3O_4 [198], MnO_2 [199] and RuO_2 [200] have been reported to be composited with graphene derivatives to produce electrodes for supercapacitors. The results showed that compared with pure graphene derivatives and metal oxides, the hybrid electrode provided about 3 times higher capacitance. Graphene-conducting polymers are also very attractive materials for supercapacitors due to their conductivity and flexibility. For example,

doped polyaniline (PANi) is one of the most frequently used polymers to be composited with GO sheets for supercapacitors [201]. It has been reported that the conductivity of GO-PANi composite improved from 2 S cm^{-1} (for pure PANi) to 10 S cm^{-1}, and the capacitance increased from 216 F g^{-1} to 531 F g^{-1} [202].

2.5.3 Solar Cell

Graphene has been an attractive material used for photovoltaic devices, which converts the solar energy into electricity. Graphene-based materials provide good transparency, high conductivity and low roughness, which make them ideal for solar cells [203]. Recently numerous graphene-based solar cells have been reported [204]. Dye-sensitized solar cells (DSSCs) have also been widely investigated because they have a moderately efficient light-to-electricity conversion efficiency, are low cost and easy to fabrication. Currently GN-TiO_2 and GN-CNT-TiO_2 have been used as the photoanode for DSSCs [205-207]. In this device, the conversion efficiency has been improved in comparison to the TiO_2 photoanode. In addition to DSSCs, quantum dots (QDs) are also anchored onto graphene to make photovoltaic devices. QDs have a large absorption coefficient and have potential as light-harvesting materials. Some results showed that when incorporated CdS QDs with graphene, the power conversion efficiencies (PCE) value increased 16% compared with pure QDs [208].

2.5.4 Catalyst

Recently, graphene has become an attractive material used as catalysts or catalyst supports in catalytic reactions due to its specific characteristics, such as a 2D structure with a high surface area and electronic transport properties [209-212]. Different graphene-based materials have been applied as catalysts in fuel cell and other catalytic reactions. For example, Pt/graphene hybrids have been used as catalysts in methanol oxidation and oxygen reduction reactions in fuel cells. The catalytic activity of Pt/ graphene was improved over Pt/carbon [212]. Moreover, bimetal catalysts such as Pt-Ru [213], Pt-Au [214], and Pt-Co [215] have been investigated to enhance activity as

catalysts. Graphene-based materials are used as catalysis in traditional reactions, such as photocatalysis reactions, as well as fuel cells. TiO_2/graphene nanostructures were applied for hydrogen evolution from water via photosplitting [216]. Photodegradation of methylene blue was also catalyzed by TiO_2/graphene hybrids [216].

Table 2.3 has summarized the typical methods to synthesize the NPs/graphene nanostructures and the applications of these nanostructures.

Table 2.3 Preparation of NPs/graphene nanostructures and applications of the materials

Nanoparticles	Synthesis	Applications	ref.
Ag	*Ex situ*: π- π stacking	SERS	[217]
Ag/ TiO_2	*In situ*: Ag is reduced by the photo-generated electrons from TiO_2/rGO	Sensors	[122]
Au	*Ex situ*: π- π stacking	Catalysis, SERS	[218]
	Ex situ: π- π stacking		[217]
	In situ: photochemical reduction		[219]
	In situ: reduction by hydroxyl-amine	Raman enhancement	[220]
	In situ: thermal evaporation	Checking layer number of graphene on substrate	[221]
CdS	*In situ*: hydrothermal	Optoelectronics	[143]
CdSe	*Ex situ*: GO+CdSe+TOPO ligand	Transparent film	[222]
	In situ: electrochemical deposition	Optoelectronics	[160]
Co_3O_4	*Ex situ*: electrostatic attraction	Li ion battery	[170]
	In situ: reduction of $Co(OH)_2$/GO at 450℃	Li ion battery	[183]
Cu_2O	*In situ*: electrochemical deposition	Photovoltaics	[223]
Fe_3O_4	*In situ*: hydrolysis starting with $FeCl_3$	Li ion battery	[176]
	In situ: redox reaction starting with Fe^{2+}, Fe^{3+}	Magnetic drug carrier	[224]
Mn_3O_4	*Ex situ*: Mn_3O_4 on GO, Ni two-step method	Li ion battery	[178]
SnO_2	*In situ*: rGO + SnO_2	Li energy storage	[225]
Pt	*In situ*: N doped rGO+DMF+NaOH+ethyleneglycol +H_2PtCl_6+$6H_2O$	Electrocatalytic activity	[226]
Pt, Au, Pd	*Ex situ*: ethylene glycol + metal precursor	Prevent restacking of graphene	[227]

2.6 Summary

NPs/graphene materials have been emerging in different areas due to the specific structures and properties of graphene. Controllable methods for preparing NPs/graphene hierarchical nanostructures have become a critical problem. Various fabrication methods, such as solution deposition, sol-gel method, covalent grafting and noncovalent processing, have been reported to prepare and enhance NPs/graphene nanostructures. Each method has its advantages based on the particular application. NPs/graphene materials have been attractive, especially in energy storage and conversion fields. They have exhibited good performance in solar cells, supercapacitors, and lithium ion batteries when working as electrode materials. Aside from being a charge collection and transportation material, NPs/graphene materials have also shown interesting results in the application of catalysts in chemical reactions. However, there are still some limitations and important problems, such as defects, low efficient assembly and poor interface between NPs and graphene, requiring further investigation. Therefore, more efforts are needed to investigate the processing-structure-property relationship in the NPs/graphene nanostructures.

Chapter III

Silver Nanoparticle/Graphene Hierarchical Nanostructure

3.1 Introduction

One of the most popular methods of producing graphene is to chemically exfoliate natural graphite flakes. However, the exfoliated graphene exhibits low conductivity due to chemical process- induced defects and attached chemical groups. In addition, monolayer graphene is a two-dimensional nanosheet that tends to stack with other sheets, resulting in a less active surface area. The attachment of highly conductive metallic nanocrystals onto graphene seems to be an effective method for increasing electrical conductivity. Among different kinds of nanoparticles, silver (Ag) nanoparticles are paid more attention due to silver's distinctive properties, such as high electrical and thermal conductivity, surface plasmon resonance, antimicrobial activity, catalytic activity, and unique optical properties [228]. Thus significant research has been carried out to study the outstanding properties of Ag/graphene hybrids, such as antimicrobial activity [229], photocatalytic activity [230], surface enhanced Raman scattering (SERS) [231], electrochemical properties [232], optical properties [233], and electrical properties [233, 234].

Moreover, the theoretical specific surface area of single layer graphene is ~2600 $m^2 g^{-1}$ which can provide a specific capacitance of ~ 550 F g^{-1} [5, 235, 236]. However, the actual specific capacitance of as-produced graphene is in the range of 90 - 264 F g^{-1} [236-238]. This is mainly due to the fact that graphene suffers from serious agglomeration which decreases its specific surface area during preparation [197, 236]. To solve this problem, lots of work has been done to create graphene with high specific area [239-242]. Graphene was also combined with pseudocapacitive electrode materials, such as polyaniline [243], RuO_2 [141], MnO_2 [199] and Fe_3O_4 [244] to prepare high-performance supercapacitor. Silver nanoparticles showed excellent performance on enhancing the electrochemical properties of carbon nanotubes [245, 246].

However, no attempt has been made to probe the effects of nanoparticle attachment on the active surface area and the electrochemical performance of graphene sheets. Additionally, the effect of silver fraction on conductivity of silver/graphene hybrids is not well understood. In this work, silver was deposited onto chemically-exfoliated graphene with different silver fractions and the effect on surface area and electrical conductivity were investigated. Highly conductive Ag/graphene hybrids may find applications in electrode materials for organic solar cells or high-performance supercapacitors.

3.2 Experimental

3.2.1 Materials and Equipment

The materials (Table 3.1) and equipments (Table 3.2) used in these experiments are listed as follows.

Table 3.1 List of materials used in the experiments

Material	Grade	Supplier
Graphite	Size:45 μm	Asbury Carbons
Sodium Chlorate	Lab grade, FW=106.44	Fisher Scientific Inc
Nitric Acid	Fuming	Acros Organics
Acetone	HPCL grade, 99.5+%	Alfa Aesar
Ammonia hydroxide	28 wt%	Sigma-Aldrich
Hydrazine	Aqueous solution (35 wt %)	Sigma-Aldrich
Silver nitrate	>99%	Sigma-Aldrich

Table 3.2 List of used equipments

Equipment	Model No.	Supplier
Sonicator	3000	Misonix
Rotate Evaporator	Rotovapor R210	Buchi, Germany
Magnetic Stirrer	RCT basic	IKA
Filtration System	All-Glass Filter Holder	Millipore Inc
PTFE membrane	0.2 μm pore size	Millipore Inc
Pump	DOA-P708-AA	GAST manufacturing Inc
Thermogravimetric analyzer	Q50	TA Inc.

3.2.2 Graphene Preparation

The scheme and process of fabricating graphene nanosheets are shown in Figure 3.1 and 3.2, respectively. Graphite flakes were chemically intercalated according to a modified Brodie's method [246, 247]. Typically, graphite (10 g), fuming nitric acid (160 mL), and sodium chloride oxide (85 g) were mixed at room temperature, but without the subsequent aging used in the Brodie's method. The mixture was stirred for 24 h, followed by washing, filtration, and cleaning as described by Brodie. Graphite oxide was collected through a precipitation method and evaporation of the solution. The graphene nanosheets were fabricated by chemical reduction of graphene oxide or thermal reduction of graphite oxide. For the chemical reduction process, 20 mg graphite oxide was dispersed in 150 mL deionized water by sonication, resulting in graphene oxide. Then 20 mL hydrazine was added and the mixture was heated in a rotate evaporator under water reflux at 95 ℃ for 24 h. The materials were filtrated, washed with water, and air-dried, resulting in chemical reduced graphene. For the thermal reduction, as produced graphite oxide was placed in the furnace of a thermogravimetric analyzer and heated from room temperature to 1000 ℃ at 100 ℃ min^{-1} under N_2 protection. After an isothermal treatment at 1000 ℃ for 15 min, the sample was collected for characterization.

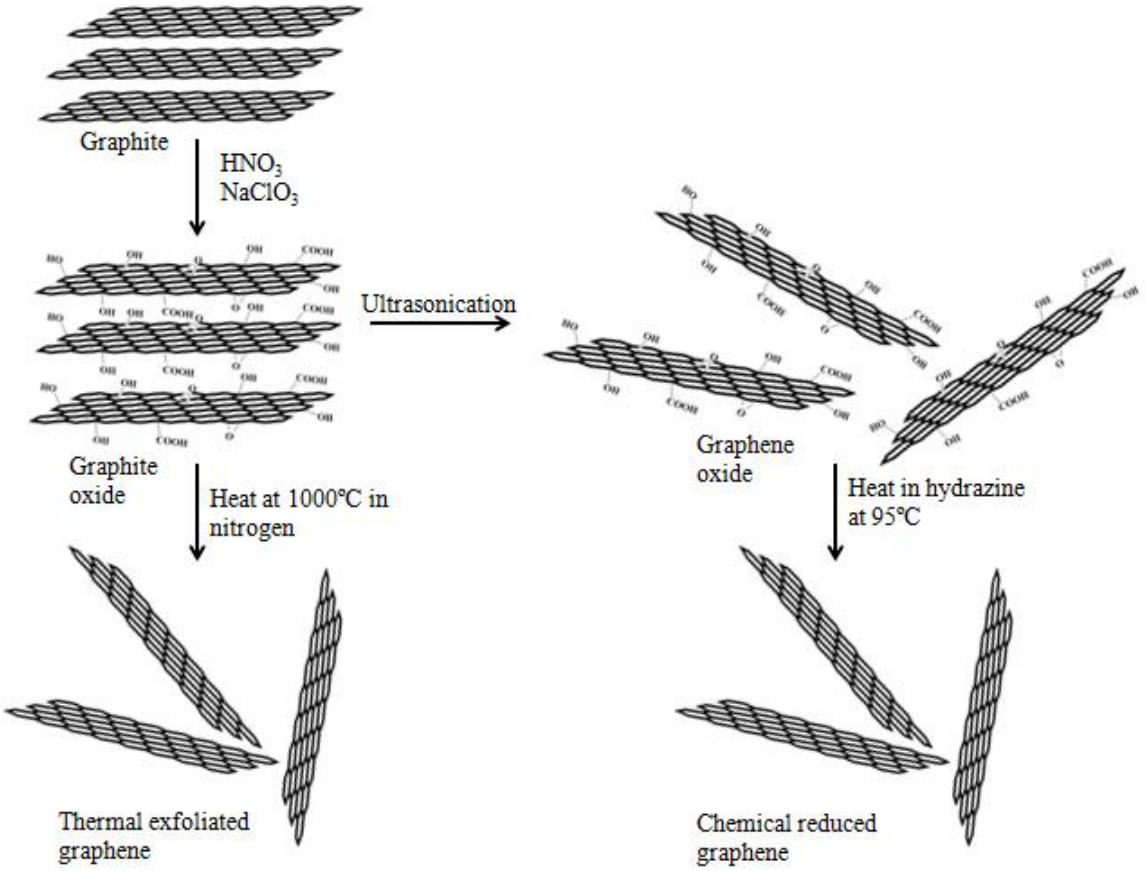

Figure 3.1 Scheme illustrates the preparation of graphite oxide from graphite and preparation of reduced graphene oxide using thermal exfoliation and chemical reduction.

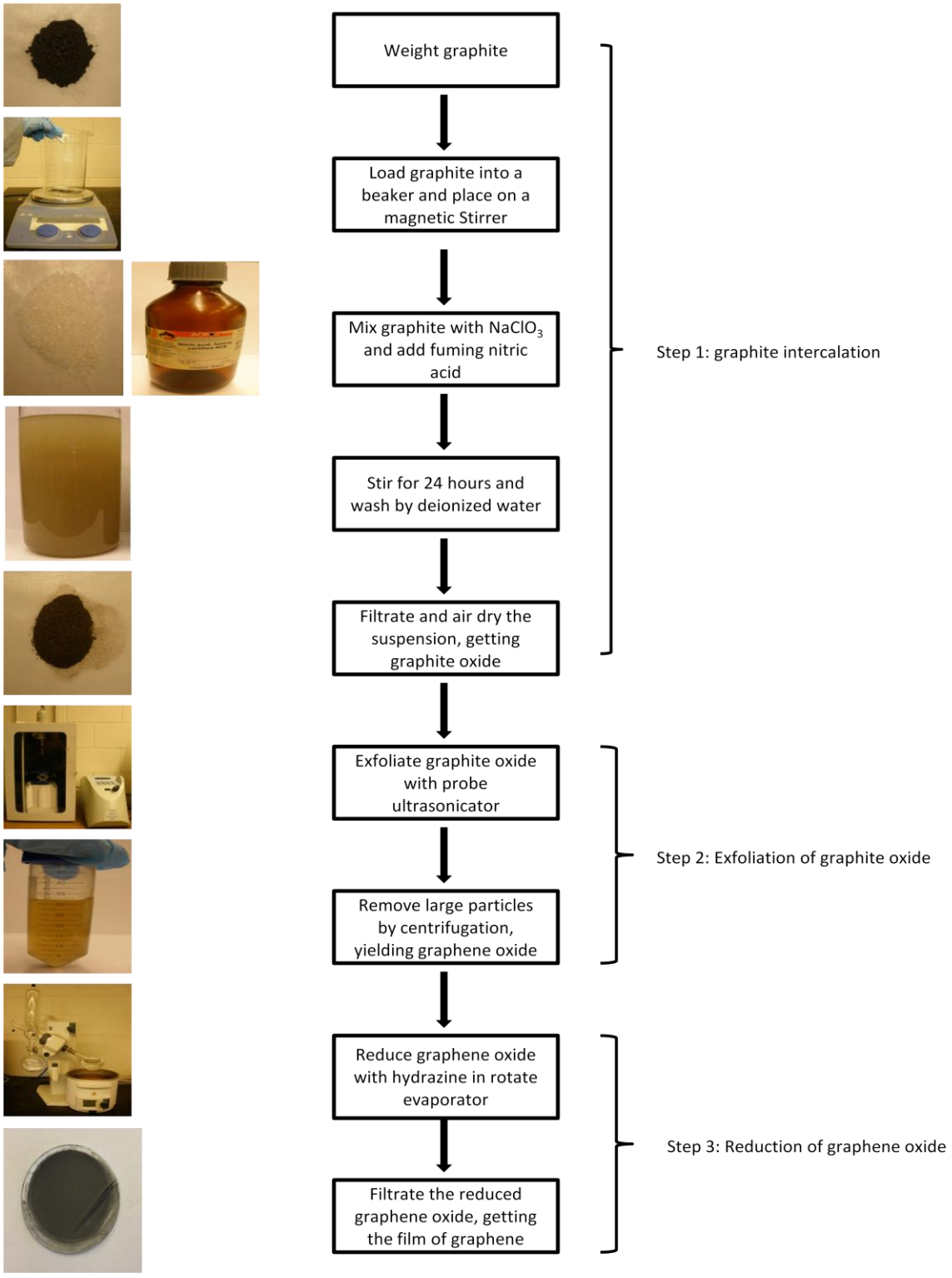

Figure 3.2 The process of fabricating graphene through hydrazine reduction.

3.2.3 Silver-Ammonia Solution Preparation

The silver-ammonia solution was synthesized with a modified method reported in the literature [248]. Silver nitrate was dissolved in 10 mL water, forming silver nitrate solutions of different concentrations (0.025 M, 0.05 M, 0.1 M, 0.4 M and 0.8 M). Ammonia hydroxide was drop-wisely added into the silver nitrate solution, forming a brown precipitation. The ammonia hydroxide was continuously added until the brown precipitation disappeared. The fresh silver ammonia solution was added into the graphene oxide solution and stirred for 24 h for ion exchange. The resulting materials were centrifuged and washed with water several times until the pH equaled to 7. The powder of $[Ag(NH_3)_2]$/graphene oxide hybrid was collected after the solution was evaporated.

3.2.4 Ag/Graphene Preparation

The Ag nanoparticle (NP)/graphene hybrid was fabricated by the reduction of $[Ag(NH_3)_2]$/graphene oxide under rapid heating. The $[Ag(NH_3)_2]$/graphene oxide hybrid was loaded into the sample pan of TGA instrument and heated from room temperature to 1000 ℃ at 100 ℃ min^{-1} under N_2 protection. The Ag NPs/graphene hybrid was collected after being kept at 1000 ℃ for 15 min. The five prepared samples were named Ag NPs/graphene (0.025 M), Ag NPs/ graphene (0.05 M), Ag NPs/graphene (0.1 M), Ag NPs/graphene (0.4 M) and Ag NPs/graphene (0.8 M), according to the different concentrations of silver salt solution.

3.2.5 Characterization

(1) Powder X-ray diffraction (XRD, Rigaku Ultima III diffractometer, 40 kV, 44 mA, with Cu Kα (λ= 1.54 Å) was used to identify the existence of Ag NPs on graphene, and data was collected at room temperature over the range $5^{\circ} \leq 2\theta \leq 80$

(2) TGA analysis was run under an air flow (60 mL min^{-1}) using a Q50 TGA instrument on sample sizes from 5 to 10 mg, and the mass was recorded as a function of

temperature. The samples were heated from room temperature to 1000 ℃ at a ramp rate of 20 ℃ min^{-1}.

(3) The Ag NPs/graphene hybrid was also characterized by high resolution transmission electron microscopy (HR-TEM, Hitachi 8100) with an acceleration voltage of 175 kV.

(4) The specific surface areas were obtained from the N_2-adsorption/ desorption analysis conducted at 77 K on a surface area and pore size analyzer (Nova 4200e model, Quantachrome Instrument Corp.). The Brunauer-Emmett-Teller (BET) specific areas were calculated from the adsorption branch of the isotherm at 77 K. All listed values are the result of an average of three sets of measurements. Prior to obtaining any results, the samples were placed on the degasser for 12 h at 150 ℃. Each set of measurements was taken at 77 mmHg and an equilibrium time of 600 s, resulting in a total experimentation time of 6-9 h per sample.

(5) The electrical conductivity of the Ag NPs/graphene hybrid was measured with a Keithley 6221 SourceMeter by a four-point configuration with probe spacing of 3.26 mm. The Ag NPs/ graphene paper was prepared by dispersing 2.5 mg Ag NPs/ graphene in 25 mL dimethylformamide (DMF) by sonication followed by filtration through a filter membrane with a pore size of 220 nm. The resulting Ag NPs/graphene film was washed with ethanol and water, and then dried at room temperature.

(6) The working electrode was prepared by casting 2 mL of well dispersed graphene and Ag/graphene toluene solution onto the glassy carbon electrode followed by drying at room temperature for 1 h. All electrochemical experiments were carried out in a 0.5 M Na_2SO_4 solution (oxygen was preremoved by bubbling N_2) using a three-electrode system, in which a platinum wire was employed as a counter electrode and Ag/AgCl as a reference electrode. Cyclic voltammetry was performed on a CHI660D electrochemical workstation at a scan rate of 2 mV s^{-1}.

3.3 Mechanism Analysis

The Ag-deposited graphene was prepared by self-assembly of silver ions onto graphene oxide, followed by simultaneous reduction of graphene oxide and silver ions. The procedure is shown in Figure 3.3. Typically, negative charge was introduced to graphene oxide by ultrasonicating graphite oxide with the assistant of ammonia hydroxide [248]. Silver ions were anchored onto the surface of graphene oxide through the electrostatic attraction between the positively charged $[Ag(NH_3)_2]$ ion in silver-ammonia solution and the negatively charged graphene oxide. Finally, $[Ag(NH_3)_2]$ and graphene oxide were reduced to Ag nanoparticles and graphene, respectively, by the thermal reduction of the $[Ag(NH_3)_2]$/ graphene oxide hybrid.

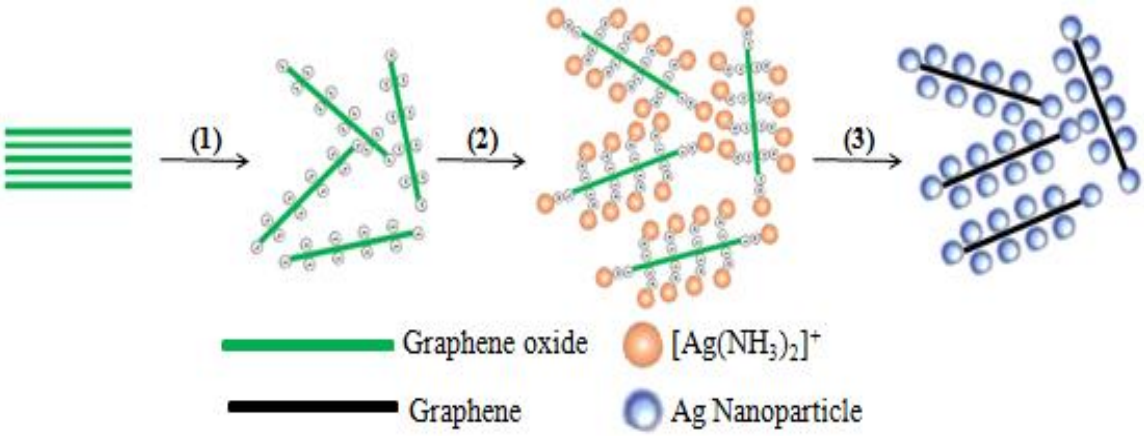

Figure 3.3 Illustration of Ag NPs/graphene hybrid formation.

As shown in Figure 3.4, we proposed the following mechanism for the deposition of silver nanoparticles on the surface of graphene sheets.

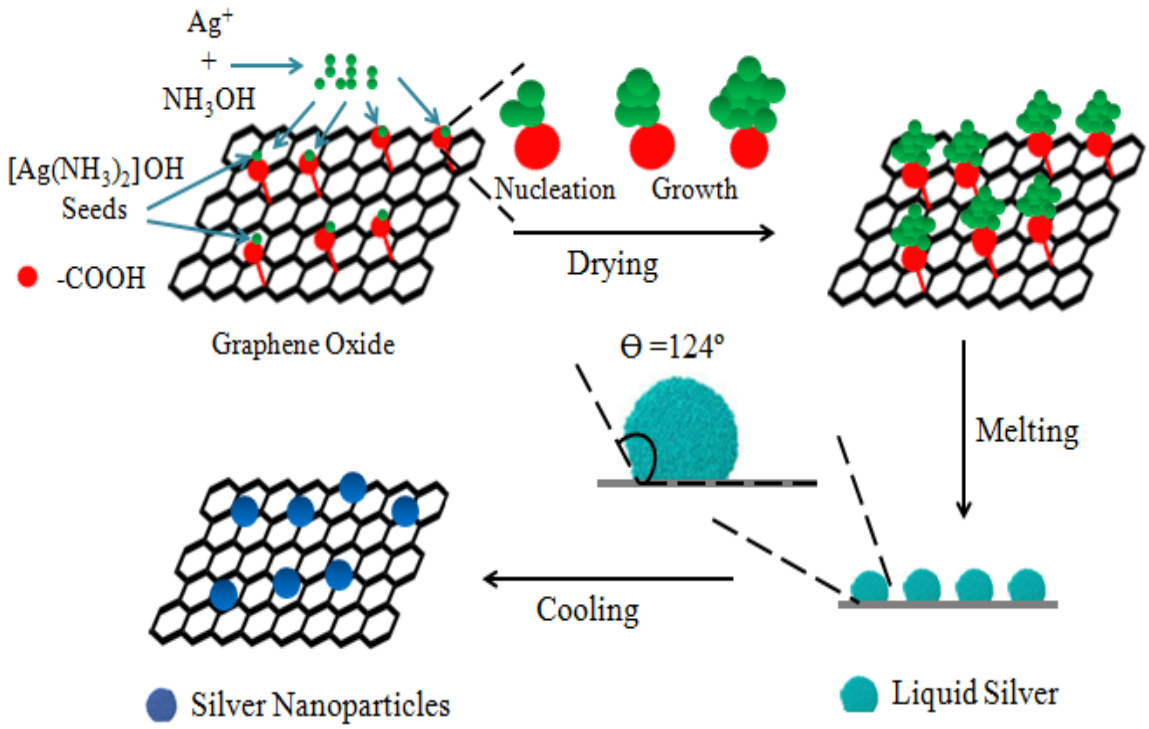

Figure 3.4 Mechanism of depositing silver nanoparticles on graphene.

Step 1: Formation of the silver ammonia complex.

Silver ammonia complex was formed by mixing silver nitrate solution with extra ammonia water.

$$AgNO_3 + NH_3 \cdot H_2O = AgOH\downarrow + NH_4NO_3$$

$$AgOH + 2\,NH_3 \cdot H_2O = Ag(NH_3)OH + H_2O$$

Step 2: Growth of silver ammonia complex nanoparticles on graphene oxide.

In this step, the carboxyl groups on GO reacted with ammonia hydroxide and ionized to $-COO^-$ ions. The $Ag(NH_2)^+$ ions were attracted onto graphene layers through the electrostatic attraction between the positively charged $Ag(NH_2)^+$ ions and the negatively charged $-COO^-$ ions, forming $Ag(NH_2)OOC-$. The $Ag(NH_2)OOC-$ aggregated on graphene layer and served as the seed of crystal growth. When the solvent was evaporated at room temperature, the silver ammonia complex became supersaturated as

the concentration increases. The crystals of $Ag(NH_2)OH$ began to grow on $Ag(NH_2)OOC$- and formed large particles.

Step 3 Simultaneous reductions of silver ions and GO.

At this stage, the reduction of silver ammonia particles and graphene oxide occurred simultaneously during the heating process from room temperature to 1273 K.

Based on our TGA experiment results, the main weight lost (~ 20 wt%) of GO occurred at around 523 K, resulting in thermally-reduced graphene. During this procedure, the oxygen-containing groups (hydroxyl, carboxyl and epoxy groups) decomposed into CO_2, CO and H_2O.

Based on literature reviews, we proposed the mechanisms of the reduction of silver ammonia complex as follows [249-252]:

$$Ag(NH_3)_2OH \xrightarrow{>413K} Ag_2O + NH_3 \uparrow + H_2O \uparrow$$

$$Ag_2O \xrightarrow{>623K} 2\,Ag + 0.5\,O_2 \uparrow$$

Therefore, GO and the silver ammonia particles were reduced to graphene and silver, respectively, under high temperature.

Step 4 Formation of silver nanoparticles

The melting point of silver is 1235K, therefore, liquid silver was formed when heated to 1273 K [253]. The contact angle of liquid silver on graphene is unknown. So the contact angle is estimated to be 124º by using the value of liquid silver on graphite [253]. Since the liquid silver could not wet the graphene surface, the liquid silver had spherical shape on graphene surface. When cooled to room temperature, the liquid silver solidified and formed spherical silver nanoparticles on graphene.

3.4 Characterization of Ag NPs/Graphene Hierarchical Materials

3.4.1 XRD Pattern

Graphene and Ag-deposited graphene were characterized by XRD and the results are shown in Figure 3.5. For the pristine graphite sample, the (002) peak appeared at 27º,

suggesting an interlayer spacing of 0.34 nm (Curve a). After oxidization, the (002) peak shifted to 12º, indicating that the interlayer distance increased to 0.72 nm (Curve b) [254]. After thermal reduction, the diffraction of graphite oxide (002) disappeared and another broad diffraction at 16º appeared which was due to exfoliation of the layer structure and the partial restacking of exfoliated graphene layers (Curve c). Ag-deposited graphene showed four new peaks at 38.3º, 44.2º, 64.5º and 77.3º (Curve d) which corresponded to the (111), (200), (220) and (311) reflection of face-centered cubic (fcc) silver crystal (JCPDS No. 4-0783) [233, 234, 255]. As shown in the inset, the broad diffraction of graphene at 16º disappeared and this may be attributed to the decorated silver nanoparticles which efficiently prevented the restacking of the exfoliated graphene sheets. The XRD pattern indicates that silver nanoparticles had been successfully incorporated with graphene and they worked as spacers to prevent the restacking of graphene sheets.

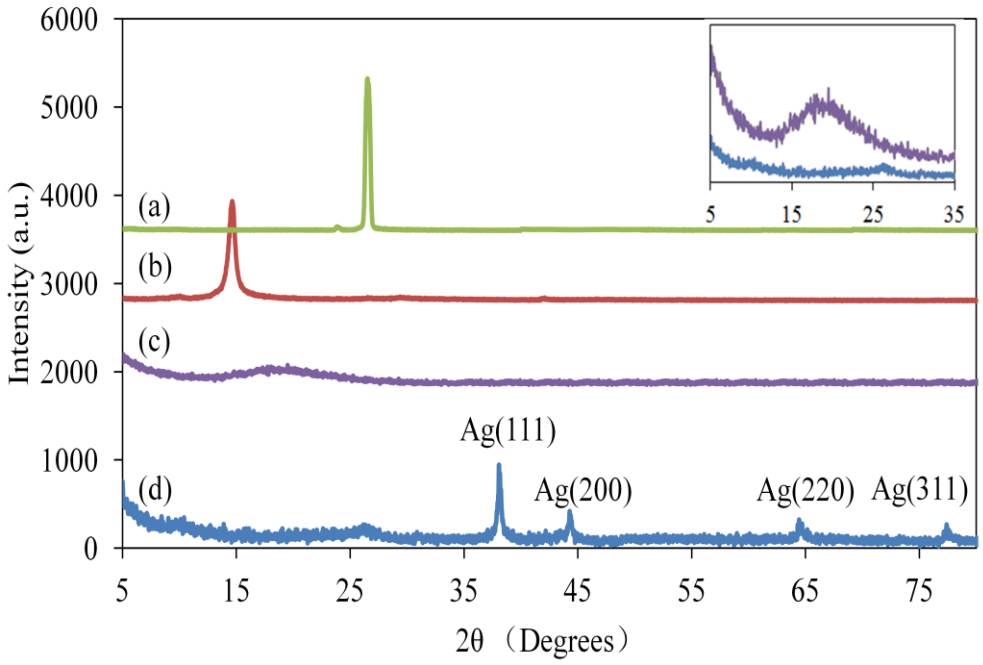

Figure 3.5 XRD results of (a) graphite, (b) graphite oxide, (c) exfoliated graphene, and (d) Ag NPs/graphene.

3.4.2 TGA Analysis

The relative amounts of Ag NPs on graphene were determined by TGA. Figure 3.6 shows the TGA results of as produced graphene and Ag NPs/graphene hybrids. As-produced graphene was completely decomposed at 700 ℃. In the Ag NPs/graphene samples, the remaining weight beyond 700 ℃ comes from the deposited silver. Through adjusting the concentration of the silver ion solution, the Ag NPs' weight percentage was tailored from 24% to 69%. The weight percentage of Ag NPs increases when synthesized with a higher concentration of silver ions (Table 3.3). The TGA results indicate that this method of adjusting the used concentration of the silver ion solution may be an effective way to tune the weight percentage of Ag NPs.

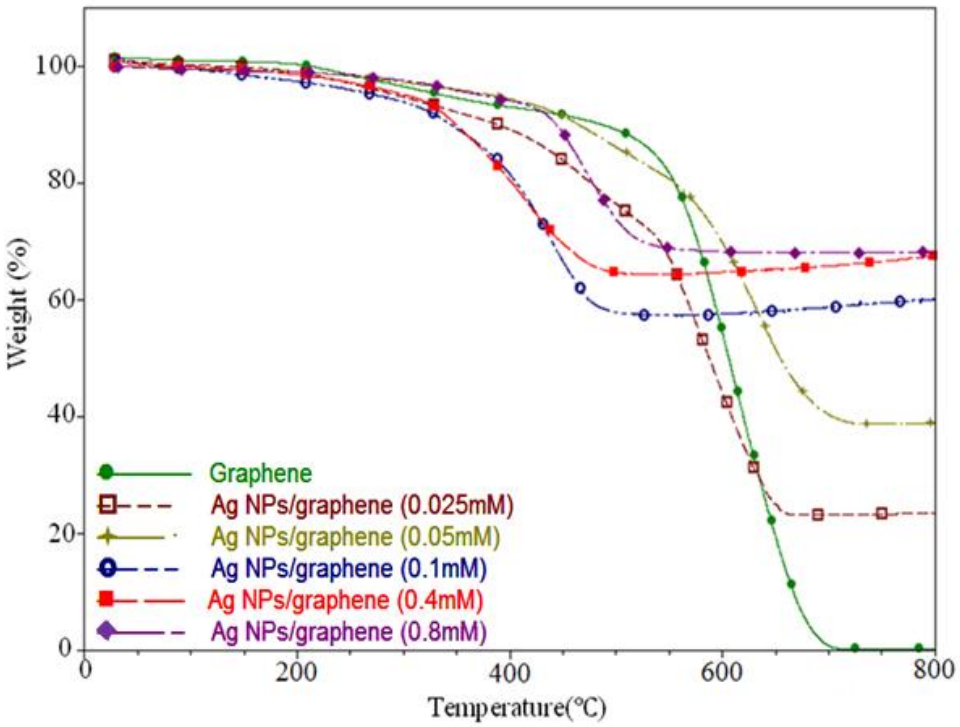

Figure 3.6 TGA results of Ag-deposited graphene and graphene.

Table 3.3 Weight percentage of silver nanoparticles on Ag deposited graphene

Sample	Weight percentage of Ag
Ag NPs/graphene (0.025M)	24%
Ag NPs/graphene (0.05M)	39%
Ag NPs/graphene (0.1M)	57%
Ag NPs/graphene (0.4M)	65%
Ag NPs/graphene (0.8M)	69%

3.4.3 TEM Analysis

The morphology of Ag NPs/graphene was characterized by HRTEM. Figure 3.7 shows the TEM images of the Ag NPs/graphene hybrid synthesized at different $AgNO_3$ solution concentrations. The smaller particles looked spherical, while the larger nanoparticles demonstrated variable shapes, which may be due to the combining of the small spherical particles [229]. The quantity of Ag NPs on the graphene surface increased noticeably when a higher concentration of $AgNO_3$ solution was used. Particularly, the sample used 0.8M $AgNO_3$ showed a much higher density of Ag NPs on the surface than other samples. This indicated that the shape, size and amount of the Ag NPs were influenced by the concentration of the $AgNO_3$ solution.

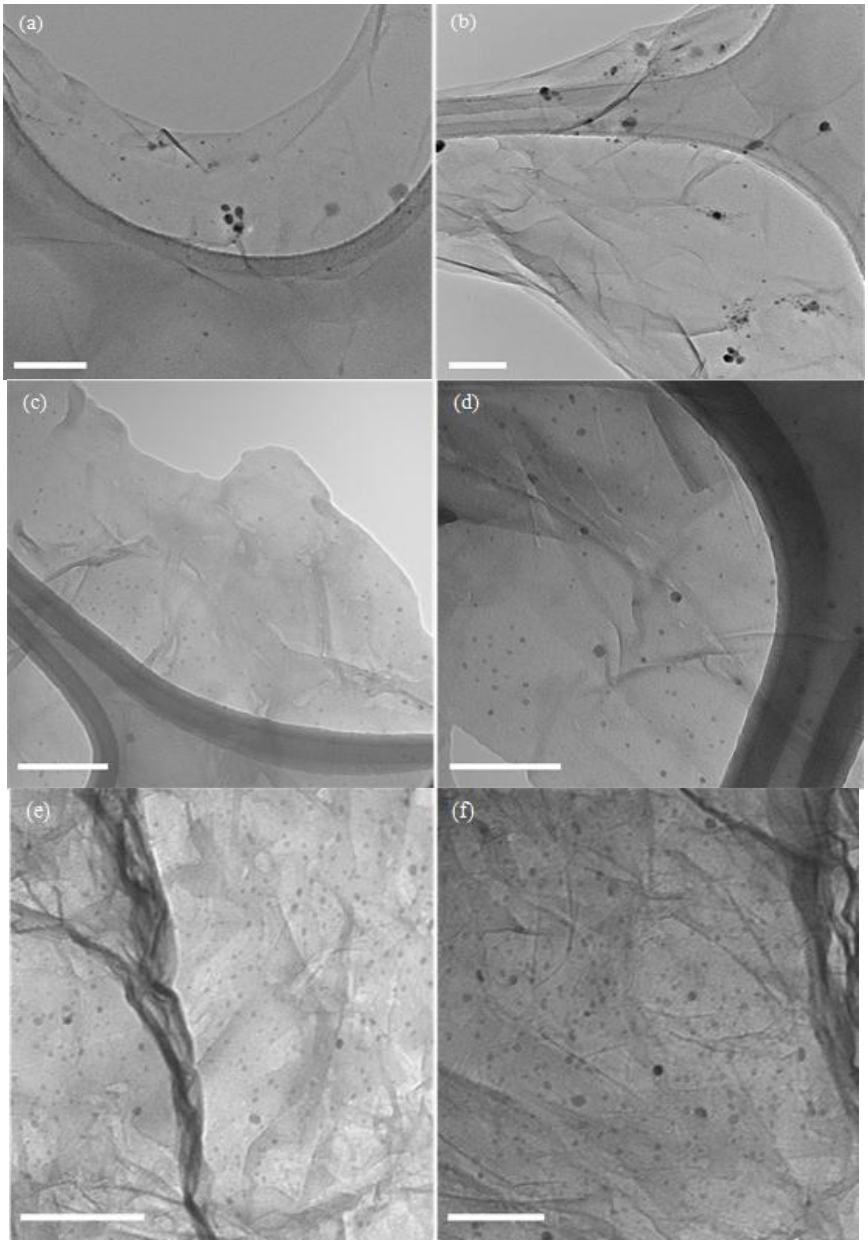

Figure 3.7 TEM images of Ag NPs/graphene synthesized by 0.025M (a), 0.05M (b), 0.1M (c), 0.4M (d) and 0.8M (e)(f) $AgNO_3$ solutions (Scale bar of all images: 100 nm).

3.4.4 Surface Area Analysis

The nitrogen adsorption / desorption behavior of chemically exfoliated graphene and Ag/graphene hybrids was also investigated and their BET surface areas were calculated. The hydrazine-reduced graphene showed a surface area of 42 m^2 g^{-1} while

thermally reduced graphene exhibited a surface area of 588 m^2 g^{-1}. Therefore, the Ag NPs/graphene were fabricated by thermal reduction, and their BET surface areas ranged from 204 to 314 m^2 g^{-1}, as shown in Table 3.4. Considering a low-density graphene (2.2 g cm^{-3}) and a high-density silver (10.49 g cm^{-3}) [78], the BET surface area (m^2 g^{-1}) was calculated by unit volume in order to better study the influence of Ag NPs on the active surface area of the hybrid material [78]. The average densities of the hybrid material were calculated using the following equations:

Table 3.4 Surface area of Ag NPs/graphene samples and as-produced graphene

Sample	BET surface area (m^2/g)	Surface area per unit volume (m^2/cm^3)
Graphene (hydrazine reduced)	42	92
Graphene (thermally reduced)	588	1294
Ag NPs/graphene (0.025M)	314	852
Ag NPs/graphene (0.05M)	254	808
Ag NPs/graphene (0.1M)	207	829
Ag NPs/graphene (0.4M)	204	923
Ag NPs/graphene (0.8M)	307	1485

$$(V_{Ag} + V_{graphene}) \times \rho_{hybrid} = M_{hybrid}$$

$$\left(\frac{M_{Ag}}{\rho_{Ag}} + \frac{V_{graphene}}{\rho_{graphene}}\right) \times \rho_{hybrid} = M_{hybrid}$$

$$\left(\frac{M_{Ag}/M_{hybrid}}{\rho_{Ag}} + \frac{M_{graphene}/M_{hybrid}}{\rho_{graphene}}\right) = \frac{1}{\rho_{hybrid}} \quad (1)$$

$$\left(\frac{W_{Ag}}{\rho_{Ag}} + \frac{W_{graphene}}{\rho_{graphene}}\right) = \frac{1}{\rho_{hybrid}}$$

$$\rho_{hybrid} = 1/\left(\frac{W_{Ag}}{\rho_{Ag}} + \frac{W_{graphene}}{\rho_{graphene}}\right)$$

where, ρ_{Ag} is the density of silver (10.49 g cm^{-3}), $\rho_{graphene}$ is the density of graphene (2.2 g cm^{-3}) and ρ_{hybrid} is density of the hybrid. M_{Ag}, $M_{graphene}$ and M_{hybrid} stand

for the mass of silver, graphene and the hybrid. W_{Ag} and $W_{graphene}$ are the weight percentages of Ag NPs and graphene respectively.

The surface areas of graphene and Ag-deposited graphene are shown in Table 3.4. The thermally reduced graphene had a surface area of 1294 m^2 per unit volume while the value for Ag-deposited graphene ranged from 808 m^2 to 1485 m^2 per unit volume. The surface area of the hybrid is lower than the value of graphene when the concentration of $AgNO_3$ solution is low (0.025 M, 0.05 M, 0.1 M and 0.4 M). While the sample that was obtained from 0.8 M $AgNO_3$ solution had a surface area of 1485 m^2 per unit volume which is higher than that of thermal reduced graphene. This may be due to the comparably high quality of silver nanoparticles on the surface of graphene and this is in accordance with the TEM results. This indicated that the Ag NPs worked as spacers and effectively prevented the restacking of chemically exfoliated graphene. And 69 wt% is a threshold that Ag NPs significantly hinder the restacking of graphene sheets for larger active area.

3.4.5 Electrical Conductivity Analysis

The in-plane electrical conductivities of the Ag NPs/graphene films were measured using a four-point method. The thickness of the paper was calculated by the following equation [233]: $M/A = \rho t$, where, M is the deposited mass, A is the deposited area, and ρ and t are the sample density and thickness respectively. The average density of the Ag NPs/graphene samples was calculated using Eq. (1). The deposited mass and area are 2.5 mg and 5.72 cm^2 respectively for each sample. The thicknesses of the samples vary from 0.9 μm to 1.6 μm.

The electrical conductivity of graphene and Ag NPs/graphene samples was plotted as a function of the weight percentage of silver nanoparticles (Figure 3.8). The graphene paper decorated with silver nanoparticles of different sizes and densities showed higher electrical conductivity than as-produced graphene paper. The Ag NPs/graphene papers with higher percentages of silver exhibited higher electrical

conductivity. In particular, the sample with 69 wt% Ag nanoparticles showed an increase of 289% in electrical conductivity, and two reasons may account for this. First, the incorporation of Ag NPs prevents the restacking of the graphene layers in the paper. Second, the Ag NPs located at the surface and interfaces of the graphene layers effectively bridged adjacent layers, thus creating conductive paths between them [233]. Silver nanoparticles could react with oxygen and hydrogen sulfide contained in air at room temperature to form a thin oxidation layer [256, 257]. The extent of oxidation is dependent on the diameter of silver nanoparticles, temperature, relative humility and exposure time of silver nanoparticles in air and it may influence the electrical conductivities of Ag NPs/graphene samples [256].

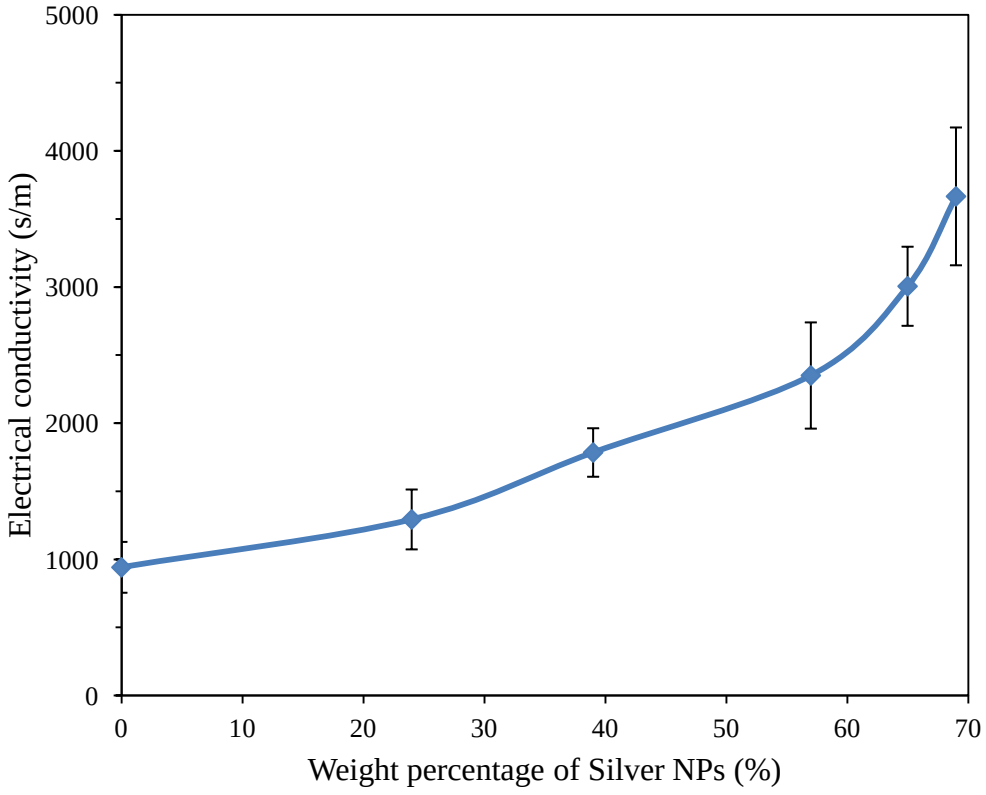

Figure 3.8 Electrical conductivity of Ag NPs/graphene hybrid with different weigh percentages.

3.4.6 Specific Capacitance

Due to the high surface area and electrical conductivity, Ag NPs/ graphene hybrid exhibited potential applications for electrochemical energy storage. As shown in Figure 3.9, Ag NPs/graphene was deposited onto a glass carbon electrode and worked as the positive electrode. Cyclic voltammetry experiments were carried out to evaluate the electrochemical performance of graphene and Ag NPs/graphene. Thermally-reduced graphene was employed as an electrode of a supercapacitor and the resultant electrochemical properties were studied. As shown in Figure 3.10, the cyclic voltammetry curves of as-produced graphene implied the electrical double layer capacitor (EDLC) nature with an approximately rectangular circle, indicating that only Na^+ adsorption/ desorption happened. The specific capacitance of the graphene was measured as 109 F g^{-1}. When Ag NPs/graphene hybrids (0.1 M and 0.8 M) were used as an electrode, respectively, the resultant current density increased significantly compared with that of as-produced graphene electrode. The specific capacitance of the Ag NP/graphene was measured as 194 and 326 F g^{-1} for 0.1 M and 0.8 M samples, respectively. The increasing specific capacitance of the hybrid may be resulted from the following reasons: First, the silver nanoparticles worked as good spacers between graphene sheets and thus increased the electroactive areas. Second, enhancement in the pore structure introduced by the silver nanoparticles between graphene layers could improve the diffusion rate of the electrolyte ions. Third, due to the increased electrical conductivity, better charge-transfer could be expected within the electrode that was fabricated by the hybrid [199]. This strongly suggested that the introducing of Ag onto the graphene led to an enhancement in the electrochemical performance.

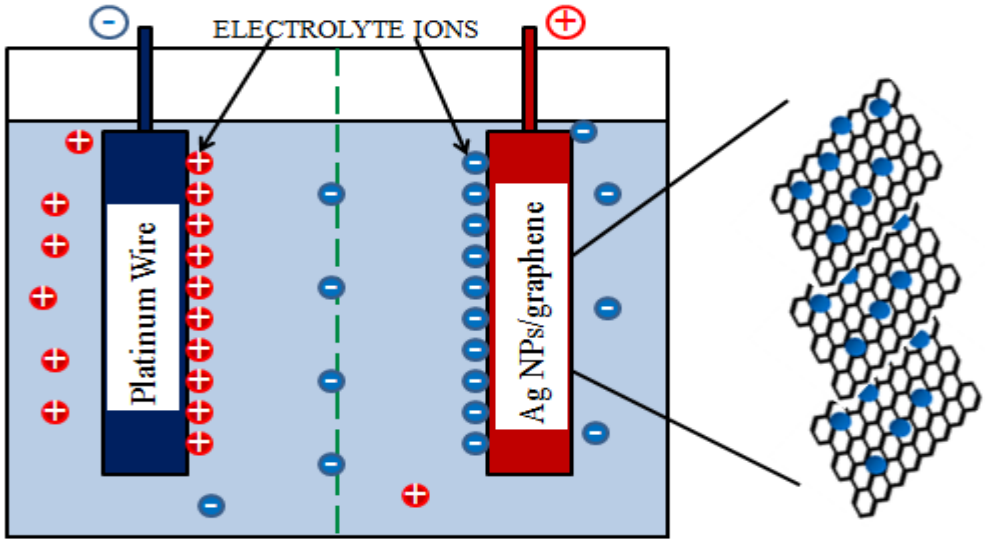

Figure 3.9 Capacitor using Ag NPs/graphene on positive electrode. (The Ag/AgCl reference electrode was omitted in this figure).

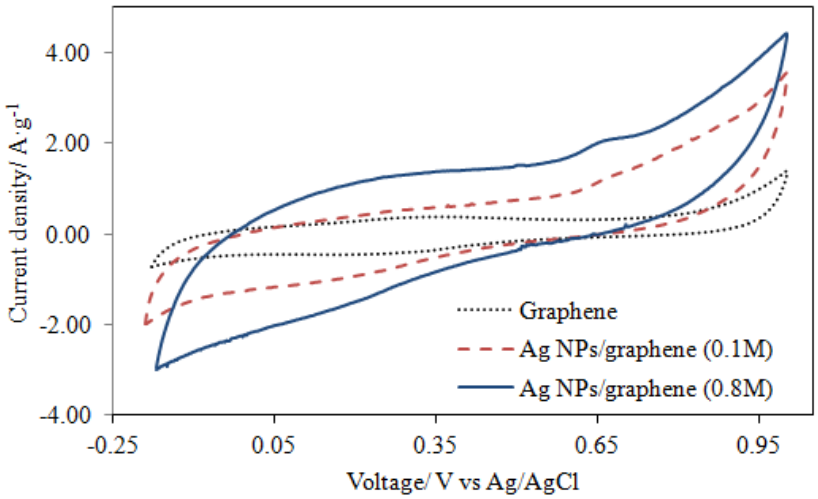

Figure 3.10 Cyclic voltammograms of graphene, Ag NPs/graphene (0.1M) and Ag NPs/graphene (0.8M) in 0.5 M Na_2SO_4 with a scan rate of 2 mVs^{-1}.

3.5 Summary

Silver nanoparticles were successfully synthesized on the exfoliated graphene layers through a simultaneous thermal reduction of graphene oxide and silver ions. The weight percentage of silver particles on graphene was tuned by adjusting silver solution concentrations. The HR-TEM images showed that the size, shape and amount of Ag NPs on graphene were influenced by the concentration of silver salt. The Ag NPs play an essential role in preventing graphene layers from restacking and aggregating; and thus, a higher surface area is created when the fraction of Ag NPs is increased. The electrical conductivity continuously increased as a function of Ag NPs fractions due to Ag NPs acting as an electrical bridge between graphene layers. The Ag/graphene was also used as the electrode of a supercapacitor and the specific capacitance was significantly enhanced in comparison to using an as-produced graphene electrode. Silver-functionalized graphene is promising for electrode materials in high-performance supercapacitors or organic solar cells.

Chapter IV

C_{60}/Graphene Hierarchical Nanostructure

4.1 Introduction

Many methods have been explored to fabricate monolayer graphene sheets [19, 47, 49, 152, 258]. Among these methods, the chemical exfoliation of graphite flakes is regarded as the most cost-effective method because it is reliable, scalable and cheap [47, 259]. In this method, graphite is first converted to graphite oxide by oxidation-based intercalation. The interlayer van der Waals force is decreased by the insertion of oxygen-containing groups (epoxy, hydroxyl and carboxyl groups) during the oxidation process. The exfoliation of graphite oxide was achieved by further ultrasonic processing and followed ultra-centrifugation [96]. However, the resulting graphene tends to agglomerate or restack to form graphite through van der Waals interactions [96]. Since most of the unique properties of graphene are only associated with individual sheets, the tendency to aggregate still remains a challenge in processing bulk-quantities [96]. To solve this problem, many attempts in chemical functionalization of graphene have been reported to improve its solubility and processability [94, 254, 260-264]. Graphene was covalently functionalized by polymer to improve its solubility and compatibility with other materials. The grafted polymers include poly(vinyl alcohol) [254, 260], polystyrene [261], and polystyrene-polyacrylamide copolymer [265]. Small molecules were also covalently grafted onto graphene to improve its solubility or tailor the properties of graphene for special applications. The small molecules used to functionalize graphene include alkyamine [266], porphyrin [262], diazonium salt [94], toluene-2,4-diisocynate [263], and alkyl isocyanates [264]. Recently, there are several reports on the fabrication of C_{60}/graphene hybrid materials through covalently functionalization. Zhang et al. grafted fullerene onto acyl-chloride functionalized graphene through covalent reaction [166, 267, 268]. However, since the acyl-chloride groups are mainly located on the edge graphene, fullerene molecules were only grafted on the edge of graphene plan. Dai et al. also

grafted C_{60} clusters onto graphene through lithiation reaction with n-butyllithium [269]. Since n- butyllithium was used in this method, this increased the cost as well as the potential dangers. Kim and his co-workers reported the non-covalent wrapping of fullerene rod into graphene layers through the method of liquid-liquid interfacial precipitation [169]. However, there are few reports on processing effect on the morphology of the C_{60} nanoparticles on graphene.

In this chapter, fullerene molecules were innovatively grafted onto graphene layers through covalent and non-covalent methods. The influence of C_{60} solution concentration on the particle size and distribution of C_{60} nanoparticles were studied and analyzed as well. Exfoliated graphene sheets usually re-stack together due to π-π interaction between graphene layers during the dispersion process. But fullerene functionalized on the surface of graphene prevents the re-stacking of graphene sheets, and maintains large specific surface area of graphene. The incorporation of zero-dimensional fullerenes onto two-dimensional graphene surface is expected to introduce some new functionality and show great potential for hydrogen storage, solar cells, sensors, thermoelectrical materials and biomedical applications.

4.2 Experiments of Covalent Functionalization

4.2.1 Materials

Toluene (>99%, pure) was purchased from Acros. The (1,2-methanofullerene C_{60})-61-carboxylic acid (FW = 778.68) and p-Toluenesulfonic acid (≥ 98.0%) were purchased from Sigma-Aldrich.

4.2.2 Covalent Synthesis of C_{60}/graphene

The functionalization of the graphite oxide was carried out by fullerene insertion and chemical reaction through the Fisher esterification between the hydroxyl groups on graphite oxide and the carboxyl groups on (1,2-methanofullerene C_{60})-61-carboxylic acid. The desiccant was filled in an appended round-bottom flask, which is connected to the

reaction flask and sealed. The water vapor generated in the Fisher esterification was continuously removed to allow constant fullerene grafting. The scheme was explained in Figure 4.1.

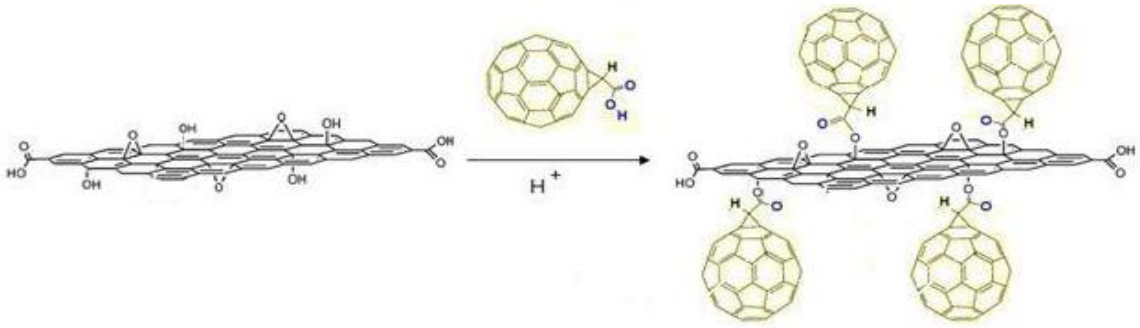

Figure 4.1 Exfoliation and functionalization of the graphite oxide with (1, 2-Methanofullerene C_{60})-61-carboxylic acid via the Fisher esterification.

After oxidation-based intercalation, the d-space of graphene layers in the graphite was expanded from 0.34 nm to ~ 0.8 nm. Fullerene molecules are in the size of 0.8 ± 0.2 nm. Some expanded graphite oxides may be exfoliated during the process and large-size fullerenes may be grafted onto them directly. Most of graphite oxide sheets will be further intercalated by small-size fullerene (less than 0.8 nm), and further exfoliated to single-layer sheet because the fullerene insertion significantly weakens the van der Waals attractions between neighboring graphene sheets. In the presence of weak acid, covalent bonding between fullerenoacetic acid and graphite oxide was formed through Fischer esterification. The condensation reaction occurs between the –COOH from the fullerene surface and –OH from the graphene surface. The attached fullerene molecules further weaken the van der Waals forces between graphene layers, resulting in exfoliation behavior.

4.2.3 Preparation of C_{60}/Graphene

Graphite oxide was prepared as described in Section 3.2.2. Subsequently, graphite oxides were exfoliated by fullerene insertion. Graphite oxide (30 mg) was first dispersed in 150 mL toluene under ultrasonic processing by Misonix sonicator 3000 for 0.5 hour at

a power of 30 W. Then 10 mg (1,2-methanofullerene C_{60})-61-carboxylic acid was added into the solution and subjected to further ultrasonic processing for 5 min at a power of 30 W. After adding 88 mg P-TsOH, the mixture was transferred to a flask of a rotary evaporator (Rotovapor R210, Buchi, Germany) with oil bath. The oil bath was heated to 90℃ and the flask was rotated for 10 h at a speed of 120 rpm under water reflux. The solid in the flask was collected by filtration and successively washed with toluene (100 mL) and water (500 mL) to yield fullerene-functionalized graphene sheets (23 mg).

4.2.4 Characterization

The resultant samples were characterized by the Fourier transform infrared (FT-IR) spectroscopy using the Spectrum- One equipped with a Universal Attenuated Total Reflectance accessory (PerkinElmer, USA). FT-IR spectra were collected, over the range from 2100 cm^{-1} to 650 cm^{-1} at a spectrum resolution of 4 cm^{-1}. A background scan of clean ZnSe-diamond crystal was acquired before scanning the samples. UV–Vis spectroscopy characterization was performed on a SHIMAZU UV-3100 spectrometer by placing liquid samples in the quartz cuvettes. Fullerene-functionalized graphene sheets were also dispersed into water, and a few drops of suspension were placed onto a silicon substrate and examined by an atomic force microscope (Multimode SPM, Veeco, Inc.) at the tapping mode.

Thermogravimetric analysis (TGA) was run under a nitrogen flow (40 mL min^{-1}) using a Pyris 1 TGA instrument on sample sizes from 2 to 3 mg, and the mass was recorded as a function of temperature. The samples were heated from room temperature to 400 ℃ at a ramp rate of 5 ℃ min^{-1}.

The fullerene functionalized graphene sheets were also characterized by high-resolution transmission electron microscopy (HRTEM, JEOL-2100) using an acceleration voltage of 200 kV.

4.3 Characterization of Covalently Functionalized C_{60}/Graphene

4.3.1 FT-IR Spectroscopy

The resultant samples were characterized by FT-IR, as shown in Figure 4.2. In the spectra of graphite oxide, the absorbance peaks at 869, 928, and 1054 cm^{-1} are attributed to the epoxy group [270-272]. The C–OH stretching is identified by the vibration peak at 1360 cm^{-1} [263, 273]. The peak at 1725 cm^{-1} corresponds to the C=O stretching from the carboxyl group [264, 274], the peak at 1615 cm^{-1} can be assigned to the adsorbed water molecules. When compare with the spectra of graphite oxide, the new peaks were observed at 1216 cm^{-1} and 1563 cm^{-1} in the spectra of fullerene-functionalized graphene. The vibration peak at 1216 cm^{-1} probably stems from the C–O–C asymmetric stretching vibration in the ester group [275]. The peak at 1563 cm^{-1} can be assigned to the antisymmetric stretching of the carboxylate functionality [276, 277]. This may be caused by the ionization of the carboxyl group in the fullerenoacetic acid. In addition, the characteristic peaks of C_{60} at 1182 and 1430 cm^{-1}[278] may be merged into the peaks at 1216 and 1360 cm^{-1}, respectively. Due to the limited amount of grafted C_{60}, the peak is too small to be observed. The FT-IR results indicate that Fisher esterification occurred between the hydroxyl groups of graphite oxide and carboxyl group of fullerenoacetic acid.

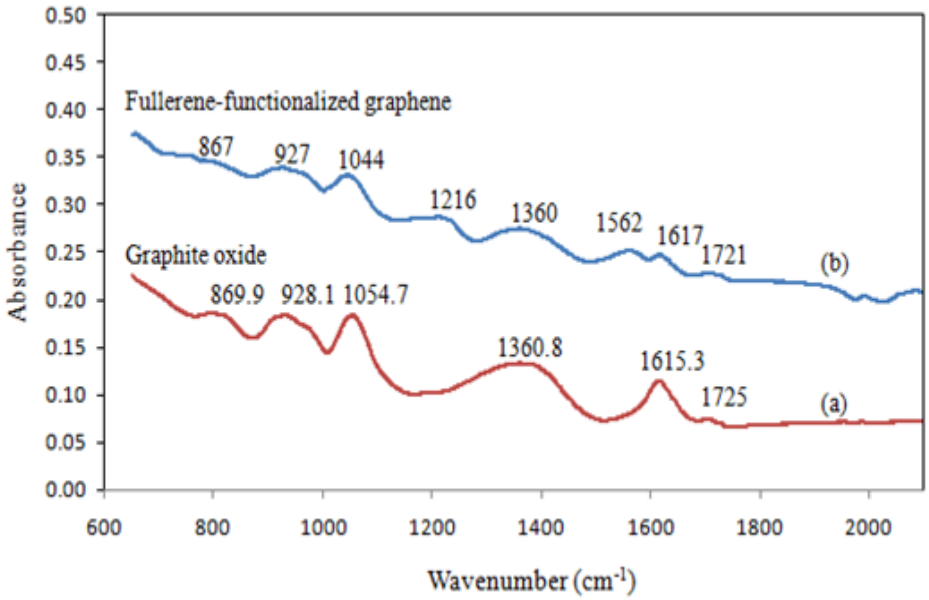

Figure 4.2 FT-IR spectra of (a) graphite oxide and (b) fullerene-functionalized graphene.

4.3.2 UV-Vis Spectroscopy

The resultant fullerene-functionalized graphene was also characterized by UV–Vis spectroscopy. As shown in Figure 4.3, fullerene-functionalized graphene sheets show a higher absorbance than graphite oxide. Since both samples have the same concentration and light path-length, the increased absorbance may be due to the higher molar absorption coefficient of fullerene-functionalized graphene sheets according to Beer–Lambert law [268]. This difference probably confirms the successful fullerene functionalization [268, 279]. This experiment also suggests that the fullerene grafting may serve as a good method to tailor the optical properties of graphene sheets. In addition, graphite oxide shows distinct Van Hove singularities, which could come from the graphene sheets. Functionalization of fullerene seems to affect the local electronic structure and significantly weakens these singularities. Due to the increased absorbance, the dispersion of fullerene-functionalized graphene has a black color, different from the brown color of graphite oxide suspension (Figure 4.3 inset). Similar color change was observed in the hydrazine reduction of graphite oxide, which was attributed to the

restoration of the electronic conjugation within the graphene sheets [96, 152]. In this experiment, the color change may be due to the introduction of the conjugated rings of fullerene.

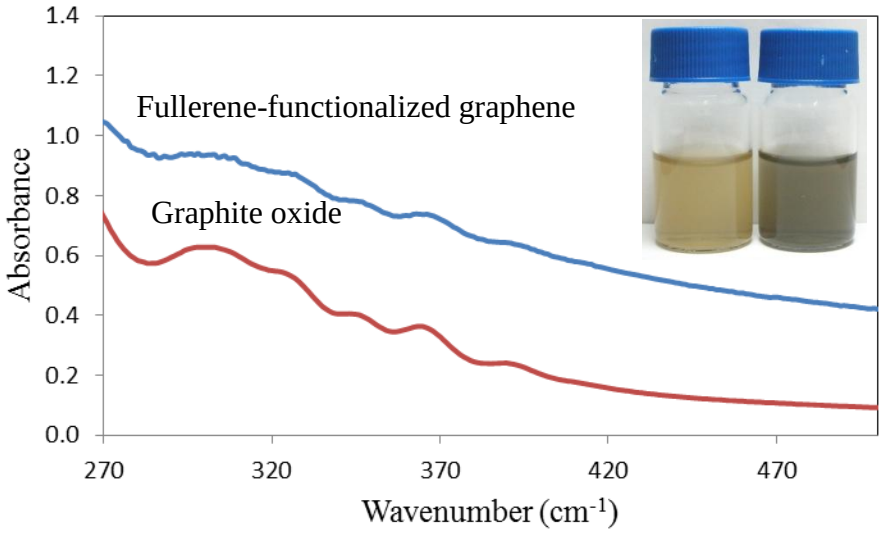

Figure 4.3 UV-Vis spectra of graphite oxide and fullerene-functionalized graphene. Inset: a photograph of graphite oxide (left) and fullerene functionalized graphene (right) dispersion at the same concentration (100mg/mL).

4.3.3 TGA Analysis

Figure 4.4 shows the TGA curves of fullerene, graphite oxide and fullerene-functionalized graphene. For the fullerene, no weight loss was observed below 400℃. Both graphite oxide and fullerene-functionalized graphene showed obvious weight loss below 400 ℃. Particularly, weight loss below 100 ℃ stems from the evaporation of water molecules which were absorbed because of the hydrophilic groups presented in both graphite oxide and fullerene-functionalized graphene [86, 100]. The major mass loss (26 wt %) of graphite oxide which was observed from 265 ℃ to 290 ℃ was due to the decomposition of the weak epoxide groups. A remaining weight of 64% was observed for graphite oxide after the removal of the epoxide groups. Fullerene-functionalized graphene showed a remaining weight of 68% after the pyrolysis of the grafted groups in

the temperature span of 230 ℃ to 260 ℃. The increased remaining weight of fullerene-functionalized graphene may come from the grafted fullerene which has a higher thermal stability. The TGA results further confirmed the successful functionalization of graphene with fullerene.

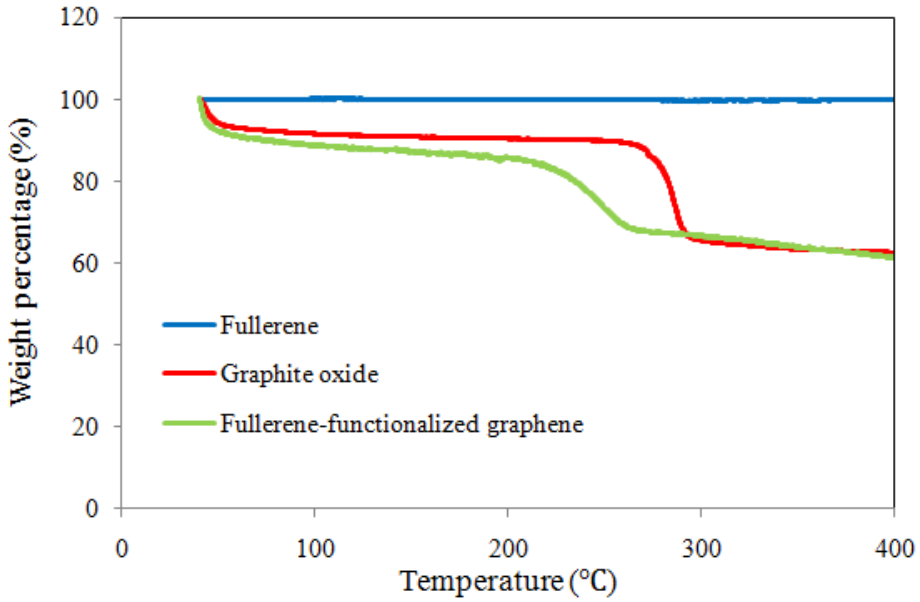

Figure 4.4 TGA results of fullerene, graphite oxide and fullerene-functionalized graphene.

4.3.4 AFM Analysis

Fullerene-functionalized graphene was also characterized by atomic force microscopy (AFM). The solid fullerene-functionalized graphene sheets were dispersed in distilled water at a concentration of 10 mg L^{-1}. The suspension was processed at a mild power with bath sonicator for 20 min to avoid breaking the chemical bond between graphene oxide and fullerene. The resultant suspension was dropped onto a silicon substrate for AFM characterization at tapping model. For the monolayer graphene sheet, it was very smooth on the surface (Figure 4.5a) while fullerene functionalized graphene showed many spherical features on the surface (Figure 4.5b). The AFM images were examined by section analysis using Nanoscope software and the results are shown on Figure 4.5c. The section analysis suggested the layer thickness of fullerene functionalized

graphene sheet was ~ 0.82 nm, indicating it is a monolayer of graphene [247, 280]. For the fullerene functionalized graphene, many spherical features were observed on the layer surface, and their height was around 2.0 nm. Since C_{60} has a diameter of around 0.8 ± 0.2 nm, the new features should be the clusters of C_{60}. In addition, much less fullerene clusters were observed on the edge of graphene sheet than on the surface. This is probably due to the fact that hydroxyl groups are mainly located on the surface of graphene oxide layers and then Fisher esterification mostly occurred on the surface [73-76].

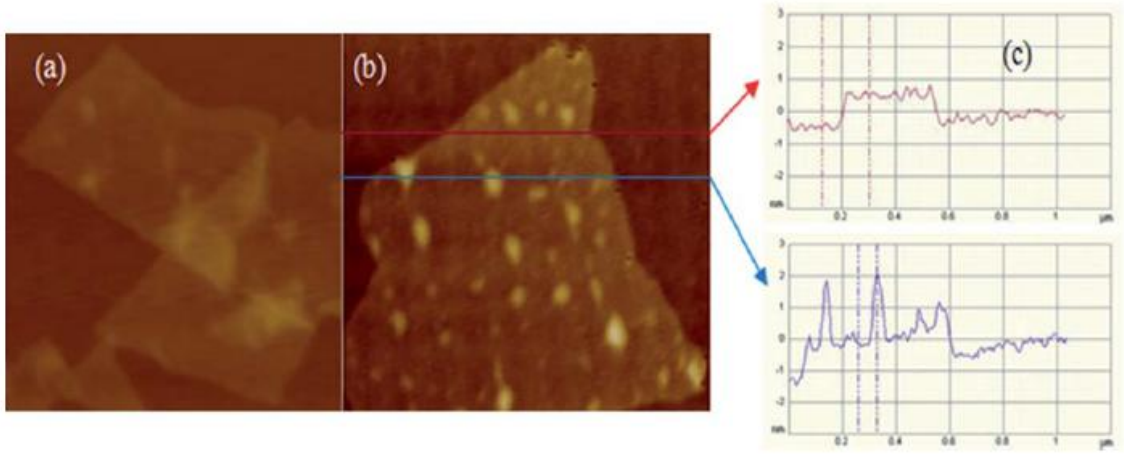

Figure 4.5 (a) AFM image of graphene sheet. (b) AFM image of fullerene-functionalized graphene. (c) Section analysis of fullerene-functionalized graphene.

4.3.5 HRTEM Analysis

HRTEM was also used to characterize the fullerene-graphene compound, and the HRTEM image is shown in Figure 4.6. In the HRTEM image, individual spherical structures that appeared as black circles with a central white spot were observed in the graphene. The measured diameter of the molecule is 0.8 ± 0.2 nm and this value is in good agreement with the reported diameter of C_{60} [165, 281]. Thus we can attribute the spherical features to the covalently grafted C_{60}. More than two C_{60} molecules are visible, but some are out of focus because the grafted C_{60} molecules are deposited at a different level of graphene and it is very difficult to find a focal plane that can include all the C_{60}.

Since C_{60} and graphene are both made of carbon, it is rather difficult to distinguish between those C_{60} grafted on the surface of graphene and graphene.

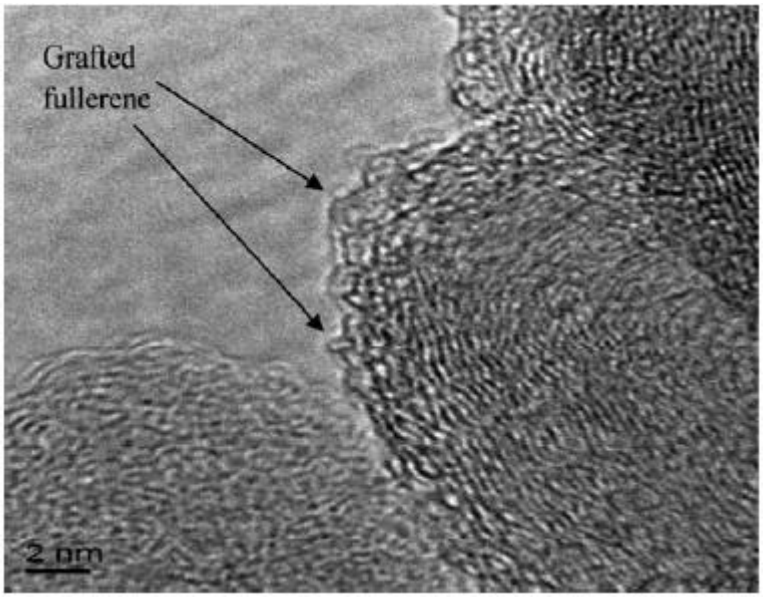

Figure 4.6 HRTEM image of fullerene-functionalized graphene compound.

4.4 Summary of Covalent Method

In summary, fullerene was intercalated to graphite oxide via the Fisher esterification between the hydroxyl groups in graphite oxide and the carboxyl groups in fullerenoacetic acid. The grafted fullerene facilitated the exfoliation of graphite oxide to monolayer graphene and helped to avoid the re-stacking of graphene sheets. This method creates a route to exfoliate and functionalize graphene and will pave a way for the application of graphene in electronic devices, energy storage, and functional materials. However, this method needs expensive materials (fullerenoacetic acid, 25mg~ $400) and long reaction time (> 24hr). Thus a fast and cheap method to fabricate C_{60}/graphene hierarchical nanostructures is proposed.

4.5 Experiments of Non-covalent Functionalization

4.5.1 Materials

The fullerene (98%), iso-proponal (anhydrous, ≥99.5 %) and m-xylene (anhydrous, ≥99%) that were used in this experiment were purchased from Sigma-Aldrich.

4.5.2 Preparation of C_{60}/Graphene

The chemical reduced graphene was prepared as described in Section 3.2.2. The C_{60}/graphene samples were prepared according to a liquid-liquid interfacial precipitation (LLIP) method [169]. Typically, C_{60} and graphene were dispersed in m-xylene and iso-proponal (IPA), respectively, through ultrasonication. Then the graphene/IPA (500 mg/L) solution was injected into the C_{60}/m-xylene solution slowly at a volume ratio of 1:1. Five different concentrations of C_{60}/m-xylene solution were used. They are 0.1, 0.5, 0.75, 1 and 2 mg/mL. After 2 hours, the resulting C_{60}/graphene was collected through vacuum filtration.

4.5.3 Characterization

XRD patterns of C_{60}/graphene samples were collected by powder X-ray diffraction (XRD, Rigaku Ultima III diffractometer, 40 kV, 44 mA, with Cu Kα, λ=1.54 Å) was used to study the C_{60}/graphene samples. The measurements were taken at a 2θ range of $5^{o} \leq 2\theta \leq 40^{o}$ with a step-width of 0.1^{o} per second at room temperature. UV–Vis spectroscopy characterization was performed on a SHIMAZU UV-3100 spectrometer by placing sample solution in quartz cuvettes. The samples were also characterized by transmission electron microscopy (TEM, Hitachi H-7650) with an acceleration voltage of 60 kV. Raman spectra were collected using the SENTTERA Raman system.

4.6 Noncovalent Synthesis of C_{60}/graphene

The C_{60} nanoparticles were deposited onto graphene as described in Figure 4.7. The graphene/IPA solution was slowly injected onto the surface of C_{60}/m-xylene solution. When the IPA meets m-xylene, an interface is formed. Since the concentration of graphene or C_{60} in the interface is lower than their initial concentration, the droplets of the two materials diffuse into the interface. The solubility of C_{60} in IPA is very low (0.002 mg/ml), so the contact of the C_{60} molecules with the IPA is unfavorable; therefore, the C_{60} molecules prefer to stay within the droplets of m-xylene. Over time, the IPA diffuses into the C_{60}/m-xylene droplet, resulting in a lower solubility of C_{60} in the droplet. When the concentration of C_{60} molecules inside the m-xylene droplets reaches the saturation point, the crystallization process occurs and a large number of C_{60} nanoparticles are formed. When there is contact with graphene layers, C_{60} nanoparticles attach onto graphene layers through π-π stacking.

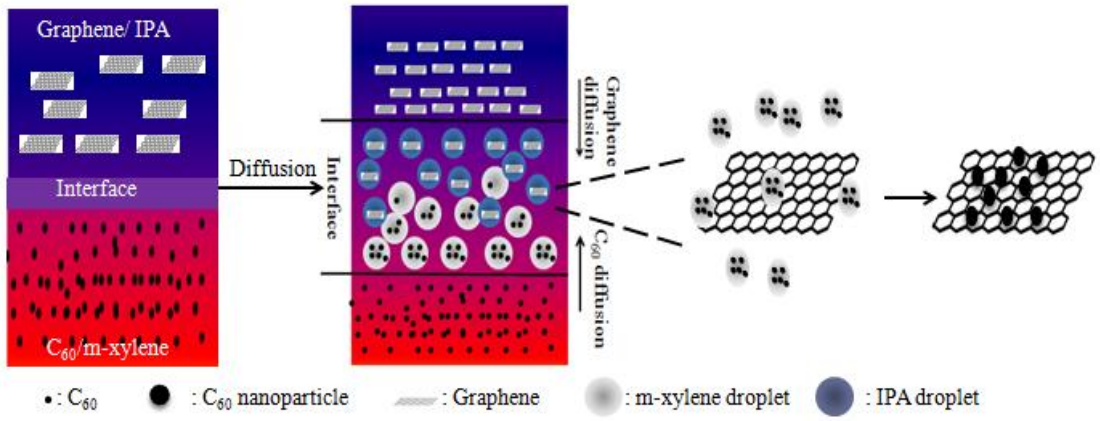

Figure 4.7 Attachment of C_{60} nanoparticles onto graphene.

4.7 Characterization of Non-covalently Functionalized C_{60}/Graphene

4.7.1 Raman Spectroscopy

Raman scattering is a fast and non destructive technique that provides a direct insight on the electronic and crystallographic structures of carbon materials[34]. The

Raman spectra of the graphene, C_{60}, and C_{60}/graphene are shown in Figure 4.8. As expected, the reduced graphene possessed an intense G-band (sp^2 carbon) at 1576 cm^{-1} [34]. The disorder-induced D-band (sp^3 carbon) at 1348 cm^{-1} is due to the presence of remaining oxygen-containing groups introduced during the intercalation procedure [86]. The sharp peak at 1466 cm^{-1} indicates the pentagonal pinch mode for C_{60} molecules [165]. The C_{60}/graphene hybrid possessed three Raman peaks at 1344cm^{-1}, 1467cm^{-1}, 1582 cm^{-1}, corresponding to the D band (1344cm^{-1}), G band (1582 cm^{-1}) of graphene, and the peak of C_{60} molecules (1467cm^{-1}). Moreover, the G band of graphene (1575 cm^{-1}) shifted to 1582 cm^{-1} in the C_{60}/graphene hybrid, indicating a charge-transfer from the graphene network to C_{60} [282], which is in accordance with the published results [169, 269]. Based on the Raman spectra, it is confirmed that C_{60} were successfully grafted onto graphene and the charge-transfer occurred between graphene and C_{60} molecules.

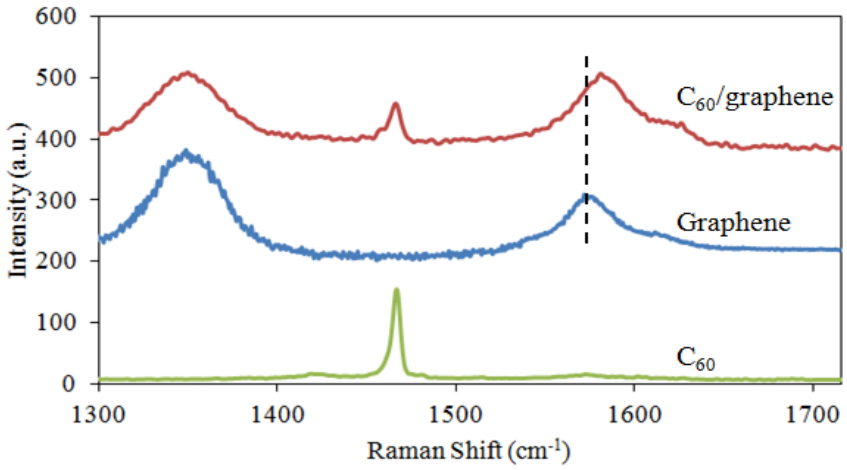

Figure 4.8 Raman spectra of C_{60}, graphene and C_{60}/graphene.

4.7.2 TEM Analysis

The as-prepared reduced graphene oxide and C_{60}/graphene nanostructures were also characterized by TEM. The reduced graphene oxide had smooth surface without any contamination (Figure 4.9a). As shown in Figure 4.9c-f, the C_{60}/graphene obviously showed some dark clusters of C_{60} nanoparticles. However, no C_{60} molecules were observed on the surface of the C_{60}/graphene nanostructure fabricated using 0.1mg/ml

C_{60}/m-xylene solution (Figure 4.9b). This might be due to the fact that the concentration of the C_{60}/m-xylene solution is too low to form a supersaturation solution after adding IPA. Therefore, a C_{60} concentration of higher than 0.1 mg/ml is needed for the growth of C_{60} nanoparticles. The C_{60} crystals had various shapes. Smaller C_{60} clusters were spherical, while larger nanoparticles showed variable shapes, which might arise from the agglomeration of small clusters [229, 283]. It is interesting that graphene layers without C_{60} molecules restacked due to the interlayer π-π interaction, forming multi-layer graphene. While the C_{60}/graphene samples showed single or few-layer structures, which might stem from the attached C_{60} particles that efficiently prevents the restacking and agglomeration of graphene layers. The TEM images indicate that C_{60} nanoparticles had been successfully incorporated with graphene and they worked as spacers to prevent the restacking of graphene sheets.

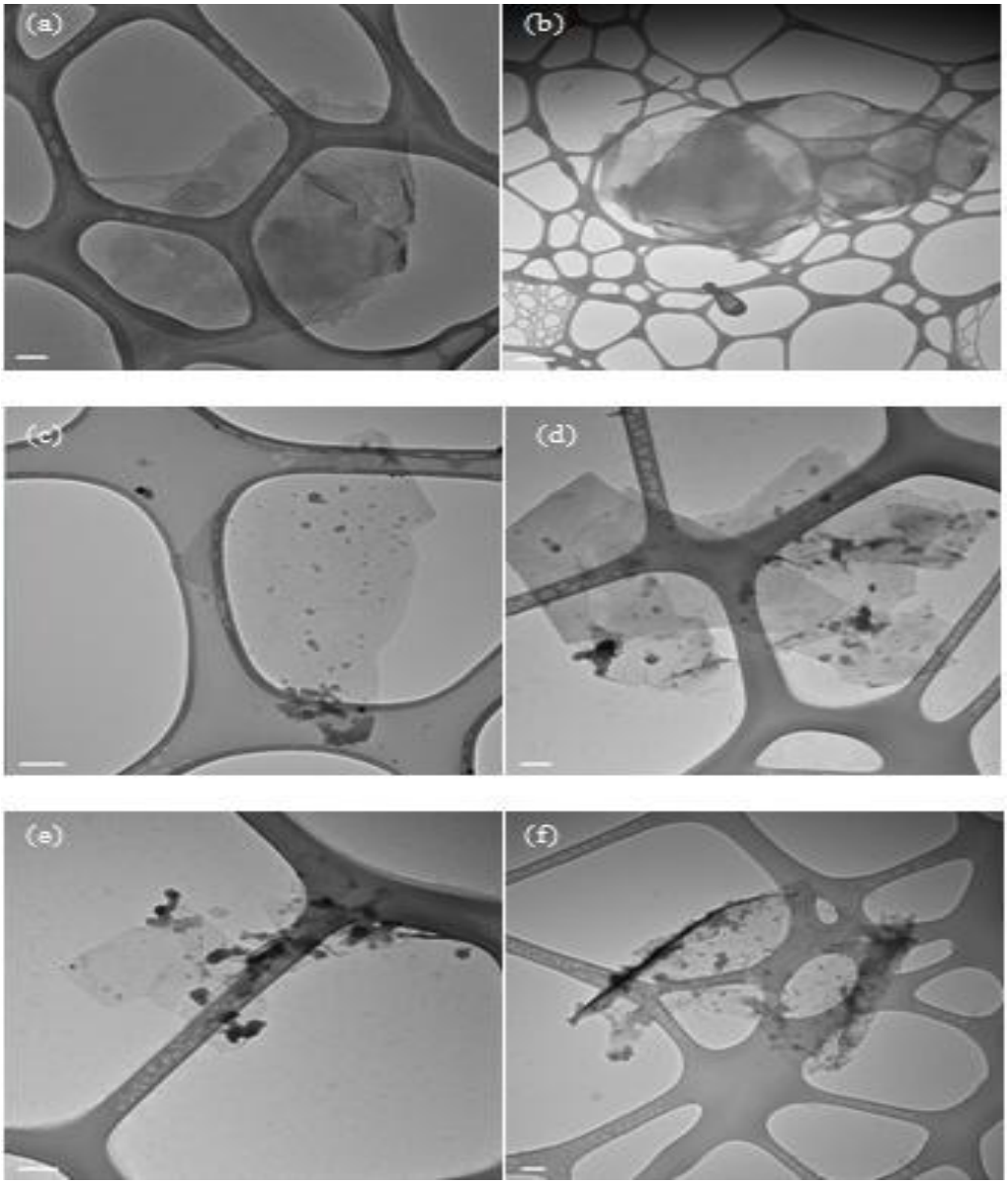

Figure 4.9 TEM images of (a) graphene. TEM images of C_{60}/graphene hybrid fabricated using (b) 0.1 mg/ml, (c) 0.5 mg/ml, (d) 0.75 mg/ml, (e) 1 mg/ml, (f) and 2 mg/ml C_{60} solution. (Scale bar for all images: 100 nm).

4.7.3 Particle Size Analysis

The particle size distribution of the grafted C_{60} was investigated based on the measurement of individual spherical C_{60} particles. Statistical results of particle size were

shown in Figure 4.10. When a 0.5mg/ml C_{60} solution was used, the average particle size was 13 nm. Higher C_{60} concentrations (0.75, 1 and 2 mg/ml) resulted in larger particles (23, 26 and 32 nm, respectively). Based on the study of Alargova et al, the diameter of the C_{60} nanoparticles prepared by LLIP method is proportional to the cubic root of the initial concentration of the C_{60} solution [284]. Thus larger average particle sizes were observed in samples prepared using C_{60} solution of higher concentration.

Additionally, it is noteworthy that the C_{60} nanoparticles prepared with higher C_{60} concentration showed wider size distribution in comparison to that with lower concentration. As described in Section 4.6, concentration difference was formed between the initial C_{60}/m-xylene solution and the interface. C_{60} solution slowly diffused into the interface and formed a concentration gradient. A higher initial C_{60} concentration tends to have a larger concentration gradient. Since the particle size is proportional to cubic root of the C_{60} concentration, thus a wider size distribution of the C_{60} nanoparticles was observed in the sample prepared with higher C_{60} concentration. So this method provides a feasible way to produce C_{60}/graphene with controllable size and distribution of C_{60} nanoparticles.

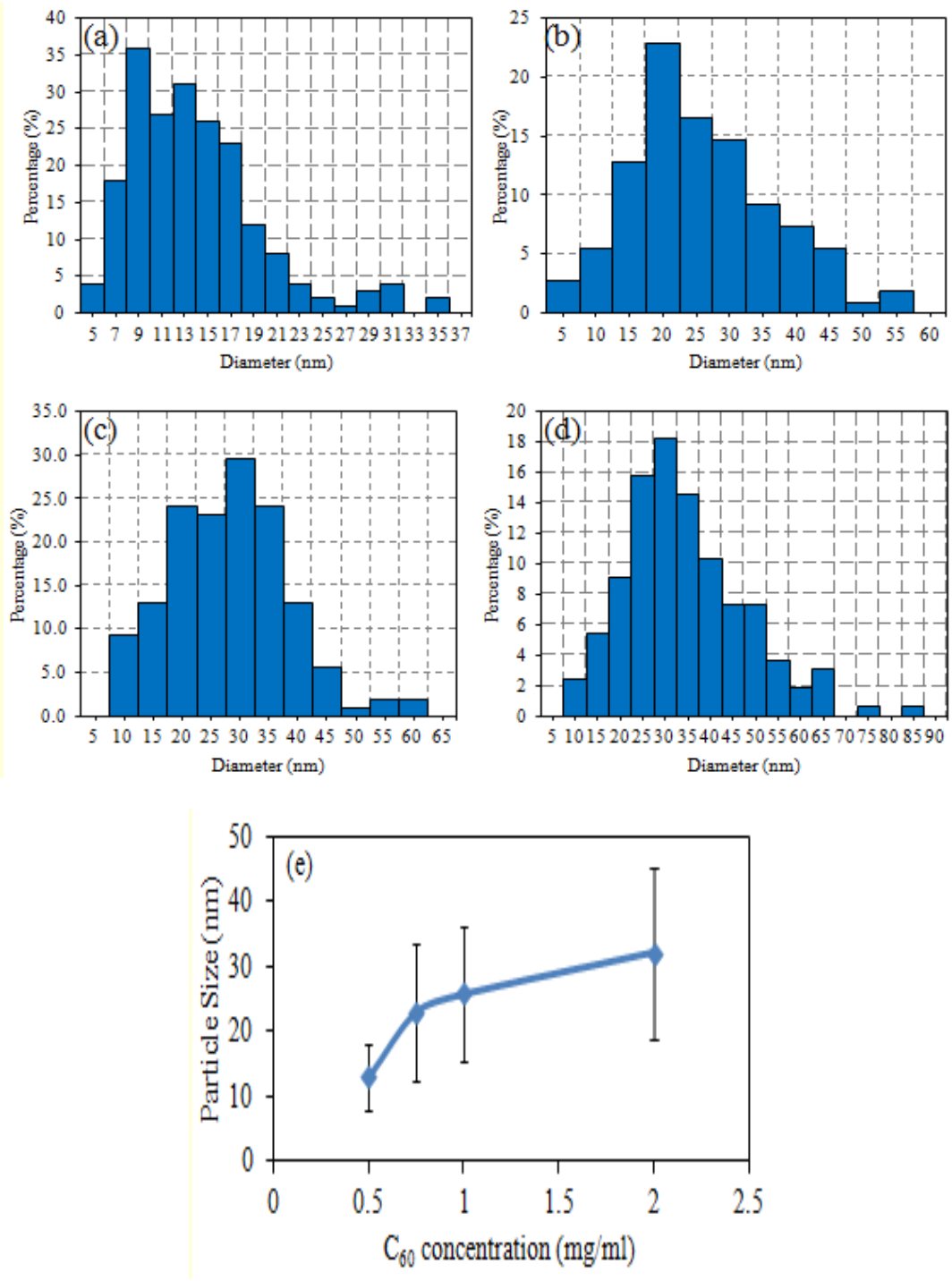

Figure 4.10 Size distribution of C_{60} clusters using (a) 0.5, (b) 0.75, (c) 1, and (d) 2 mg/ml C_{60}/m-xylene solution and (e) particle size comparisons of samples using different C_{60} concentration.

4.7.4 XRD Pattern

Graphene and C_{60}/graphene samples were characterized by XRD and the results were shown in Figure 4.11. The (002) peak of graphite at 27° indicates an interlayer spacing of 0.34 nm (Curve a). The (002) peak of graphite oxide shifted to 12°, indicating that the interlayer spacing increased to 0.72 nm after oxidization (Curve b) [280]. After chemical reduction by hydrazine, the sharp (002) peak of graphite oxide disappeared and another broad peak near 24° appeared (Curve c). This can be attributed to the exfoliation of the layer structures of graphite oxide and the partial restacking of exfoliated graphene layers. C_{60}/graphene sample showed characteristic peaks of C_{60} at 10.8°, 17.7°, 20.8°, 21.7°, 27.5° and 28.2° corresponding to the (111), (220), (311), (222), (331) and (420) diffraction of C_{60} (Curve d) [285]. As shown in the inset, the broad diffraction of graphene in the range of 22° to 26° disappeared. This might be attributed to the grafted C_{60} nanoparticles, which effectively prevented the restacking of the graphene layers. The XRD pattern indicates that C_{60} fullerenes had been successfully incorporated onto the surface of graphene and they worked as spacers to keep the individual graphene sheets from restacking.

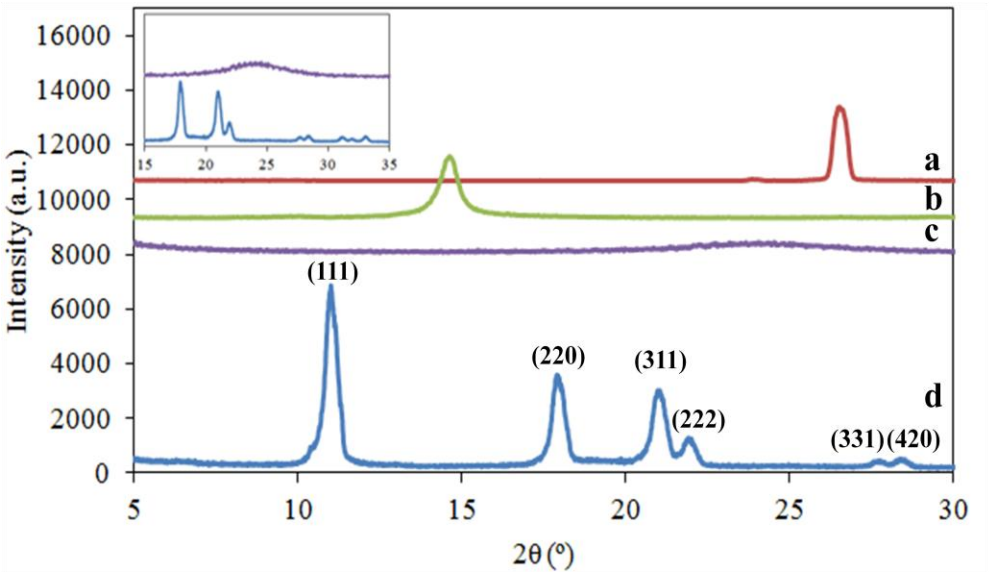

Figure 4.11 XRD patterns of (a) graphite, (b) graphite oxide, (c) reduced graphene, and (d) C_{60}/graphene nanostructures.

4.7.5 UV-Vis Spectroscopy

The UV-Vis spectra of C_{60} and C_{60}/graphene were collected by testing the solution of C_{60} and C_{60}/graphene in the same solvents (Figure 4.12). The spectrum of the C_{60} showed two characteristic peaks at 280 and 328 nm. The peak at 328 nm stemmed from π- π* electronic transitions [286]. The red shift of the peak at 328nm is correlated with the interactions between C_{60}, thus this peak is a crucial indicator for the interaction of fullerene and the aromatic rings of graphene [287]. The π-π stacking of C_{60} and graphene may delocalize the π electron system and reduce the energy for the electronic transition [169]. Therefore, the peak at 328 nm in C_{60} shifted to 334 nm in the C_{60}/graphene. The shift indicates that C_{60} was successfully grafted to graphene and the π-π interaction was the main driving force for the formation of the as prepared C_{60}/graphene nanostructures.

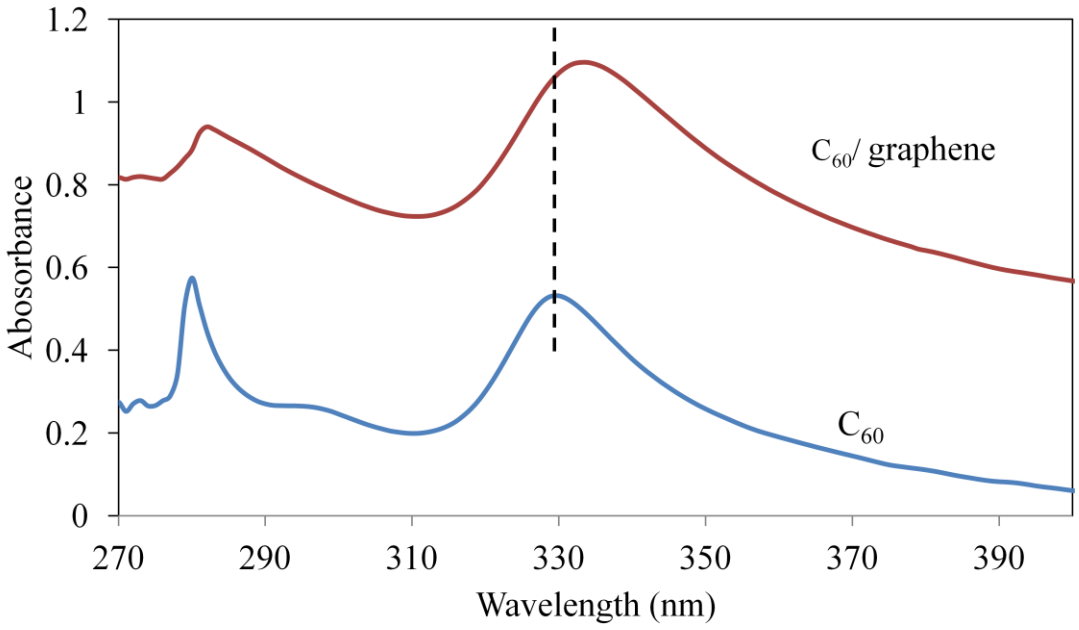

Figure 4.12 UV-Vis spectra of C_{60} and C_{60}/graphene hybrid in solution.

4.8 Summary of Non-covalent Method

The C_{60} nanoparticles were grafted onto graphene nanosheets through non-covalent method (liquid-liquid interfacial precipitation). The results of UV/Vis spectroscopy, Raman spectroscopy and X-ray diffraction indicate the successful grafting of C_{60} nanoparticles to the graphene layers. The TEM results of the C_{60}/graphene hierarchical structure indicate that the size of the grafted C_{60} nanoparticles can be tuned by adjusting the concentration of the C_{60} solution.

4.9 Summary

The C_{60}/graphene hierarchical nanostructures were fabricated through covalent and non-covalent methods. In the covalent method, C_{60} molecules were grafted onto graphene through Fisher esterification. Individual C_{60} molecules were observed on the graphene layer. However, this method used expensive materials and is time consuming. In the non-covalent method, C_{60} nanoparticles were incorporated with graphene layer through π-π stacking. The particle size and size distribution of the C_{60} nanoparticles can be tuned through adjusting the concentration of the C_{60} solution. When compared with the covalent method, the non-covalent method is more facile, faster and scalable.

Chapter V

Seebeck Effect of C_{60}/Graphene Nanocomposites

5.1 Introduction

The thermoelectric effect is the direct conversion of temperature differences to electrical voltage and vice-versa. This phenomenon is expected to play an increasingly important role in power generation, solid-state cooling, and heating systems [288]. The efficiency of thermoelectric (TE) materials depends on a combination of material properties quantified by the thermoelectric figure of merit $ZT = S^2\sigma T/k$, where S is thermopower (μVK^{-1}), σ is electronic conductivity (Sm^{-1}), k is thermal conductivity (WmK^{-1}), and T is temperature (K). While S and σ are primarily based on electronic structure, k typically has both electron and phonon contributions [289]. High Seebeck coefficient, high electrical conductivity, and low thermal conductivity are required in order to generate power in advanced thermoelectric materials. Since it is currently very technically challenging to measure in-plane thermal conductivity of thin films, some groups used cross-plane thermal conductivity as an estimate, or only reported the power factor [290]. The power factor is the product of electrical conductivity and the square of the Seebeck coefficient of the materials [290].

Currently, the majority of research in the field are focused on inorganic semiconductors [291-293], including Bi-Te series, Pb-Te series and Si-Ge series. Among these semiconductors, Bi_2Te_3 demonstrated the best thermoelectric performance. The p-type Bi_2Te_2 nanowire showed a ZT of 1.2, and p-type Bi_2Te_3/Sb_2Te_2 hybrids demonstrated a ZT of 2.4 [294]. However, the toxicity, high cost and complex manufacturing process of the inorganic TE materials are hindering their wide applications to new TE systems [291, 295]. Therefore it is necessary to explore novel TE materials with a high performance and low cost.

Conducting polymers, such as polythiophene, polyaniline (PANI) and poly(3,4-ethylenedioxythiophene):poly(styrene sulfonate) (PEDOT:PSS), possess advantages such

as low thermal conductivity, low cost, easy synthesis, easy processing into versatile form and low density, which offers them a significant advantage over conventional inorganic TM materials [7, 296]. However, the low electrical conductivity and low Seebeck coefficient have hindered these polymers as feasible candidates for TE materials in the past years [7]. Therefore, it is necessary to find proper materials which can increase the electrical conductivity of those polymers and maintain their low thermal conductivity.

To achieve this goal, considerable work has been carried out. Carbon nanotubes were utilized as the template for the growth of PANI nanocomposite to optimize the Seebeck coefficient, electrical conductivity and thermal conductivity, which achieved a ZT of 0.01 [7, 294, 297]. In addition, PEDOT:PSS stabilized CNTs were incorporated into polyvinyl acetate through a latex method. The nanocomposite showed a ZT of 0.02 with a CNTs loading of 35 wt% [298]. Graphite oxide sheets were applied as the template for the growth of PANI, resulting in a higher electrical conductivity and Seebeck coefficient due to the increased carrier mobility. The optimal ZT value of the graphite oxide/PANI composite is 4.86×10^{-4} [293].

The thermoelectric properties of graphene have recently received considerable attention because of its promising applications [288, 299-305]. However, reported ZT values of graphene are not promising, typically in the range of 10^{-10} to 10^{-9} [304, 305]. The Low ZT values are mainly due to two factors: (1) the high thermal conductivity of graphene (~1000 W m^{-1} K^{-1} for chemically reduced graphene) and (2) the low Seebeck coefficient of graphene (-10 to 20 μVK^{-1}) [306, 307]. To increase the Seebeck coefficient, oxygen plasma treatment of graphene [307] or molecular attachment [306] have been applied. Ajayan et al. reported that oxygen plasma treatment of graphene could generate local disordered carbon that opens the band gap and thus increases the Seebeck coefficient of the modified graphene to ~700 μVK^{-1} at 575 K [306]. Yan and his coworkers increased the Seebeck coefficient of few-layered graphene to 180 μVK^{-1} at 573 K by attaching molecules with high Seebeck coefficient value [307].

C_{60}, another hot carbon material, possesses an experimental Seebeck coefficient value over 2000 μV/K at 300K [308]. Moreover, the thermal conductivity of C_{60} can reach to 0.16 $W/m^{-1}K^{-1}$ [309]. According to the unique properties of graphene and C_{60} fullerenes, it might be an exciting way to develop novel thermoelectric materials by combining the outstanding properties of graphene and C_{60} into a hybrid structure. The incorporation of C_{60} can balance the thermal conductivity and increase the Seebeck coefficient while maintaining high electrical conductivity, which will result in an enhanced thermoelectric performance.

In this chapter, C_{60}/graphene hierarchical nanostructures with different amounts of C_{60} nanoparticles were prepared. Film composites were prepared by incorporating C_{60}/graphene nanostructures into epoxy resin and PEDOT:PSS. The electrical conductivity, Seebeck coefficient and power factor of the composite film were measured and analyzed.

5.2 Experimental

5.2.1 Materials

The PEDOT:PSS (PH1000) was purchased from Clevios. Epoxy resin (Epon 862) and curing agent (EPI-W) were kindly provided by Hexion.

5.2.2 Preparation of C_{60}/Graphene Hierarchical Nanostructures

The C_{60}/graphene hybrid was fabricated using the same procedure as described in Section 4.5.2. Typically, the graphene/IPA (500 mg/L) solution was injected onto the surface of C_{60}/m-xylene (500 mg/L) solution. By changing the volume ratio between the graphene/IPA solution and the C_{60}/m-xylene solution, C_{60}/graphene samples with a different weight percent of C_{60} were prepared. After 2 hours, the resulting C_{60}/graphene was collected through vacuum filtration.

5.2.3 Preparation of C_{60}/Graphene/Epoxy Nanocomposites

To fabricate the C_{60}/graphene/epoxy composite, epoxy resin (Epon 862) and curing agent (EPI-W) were mixed at a weight ratio of 100: 26.4, followed by bath sonication in acetone (1g/ml) for 10 minutes. The mixture was then added into a C_{60}/graphene (C_{60}: graphene= 1:9 by weight) solution that was prepared as previously described. The resultant mixture was stirred by a Teflon bar and collected through vacuum filtration.

5.2.4 Preparation of C_{60}/Graphene/PEDOT:PSS Nanocomposites

The C_{60}/graphene/PEDOT:PSS composite was prepared by mixing the C_{60}/graphene solution in the water solution of PEDOT:PSS with a Teflon stir bar. Then the composite film was collected by vacuum filtration.

5.2.5 Characterization

The weight percent of the C_{60}/graphene hierarchical nanostructure was determined by TGA (Q50) at a ramp rate of 10ºC per miniature in nitrogen. Electrical conductivity measurements were performed on a SRM probe (Bridge Technology Inc.) by a standard four-point probe method with a Keithley 2400 current Source Meter and a Keithley 2182A Nanovoltmeter at room temperature. For the Seebeck coefficient measurements, the thermal voltage was achieved by connecting a Keithley 2182A Nanovoltmeter with two identical bare copper wires, which were bonded onto sample films at 20 mm spacing by silver paste. The temperature gradient was obtained by using two Omega Inc. surface temperature thermocouples that were controlled by a SM325 thermometer data logger. The Seebeck coefficient measurement was calibrated before measurement, and the Seebeck coefficient was calculated with $S=-\Delta V/\Delta T+S_{Cu}$, where S_{Cu} is 6.5 uV/K at room temperature [294]. All thermoelectric properties were measured at room temperature.

5.3 Power Factor of C_{60}/Graphene/Epoxy Nanocomposites

The electrical conductivity and the Seebeck coefficient of the composites were measured. The results were plotted in Figure 5.1. Pristine epoxy resin was insulating (10^{-14} S/m) [310], and with the addition of 18wt% C_{60}/graphene, the electrical conductivity increased by more than 10^{15} order to 45.6 S/m (Figure 5.1a). With the further addition of the C_{60}/graphene hierarchical nanostructures, the electrical conductivity of the composite continued increasing to 2949 S/m. In the nanocomposite, the electrical conductivity σ can be expressed by [311]:

$$\sigma = en\mu$$

Where, e, n and μ are the electron charge, carrier concentration and carrier mobility, respectively. The incorporation of the C_{60}/graphene hierarchical nanostructure may increase the carrier concentration and carrier mobility, thus resulting in an enhanced electrical conductivity of the nanocomposite. The Seebeck coefficient of the nanocomposite decreased with higher loadings of hierarchical nanostructures. Based on the study of Chen et al., the Seebeck coefficient can be expressed as [311]:

$$\mathrm{S(T)} = \frac{E_F(T) - E_T}{eT}$$

Where, E_F is the Fermi level, and E_T is the carrier transport level. The energy difference $E_F(T)$-E_T is correlated to the carrier concentration. A larger carrier concentration may reduce $E_F(T)$-$E_{T,}$ resulting in a decreasing Seebeck coefficient [311]. Thus, the Seebeck coefficient decreased with higher loading of the C_{60}/graphene hierarchical nanostructures. The power factor of the composites was calculated and shown in Figure 5.1b. The sample with 45 wt% C_{60}/graphene showed the highest power factor of 1.1 $\mu W/K^2m$.

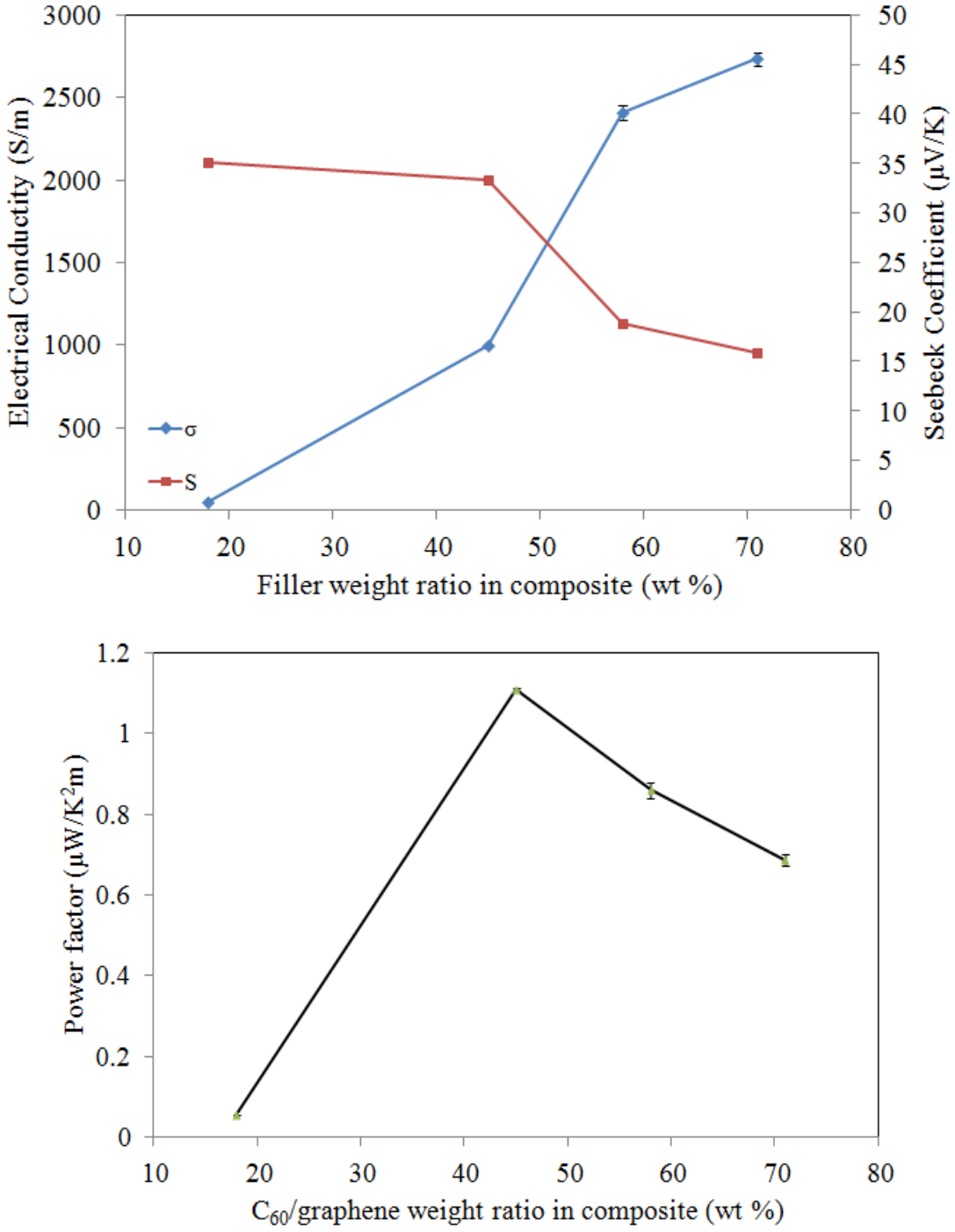

Figure 5.1 (a) Electrical conductivity, Seebeck Coefficient, and (b) power factor of the C_{60}/graphene/epoxy composite.

5.4 Power Factor of C_{60}/Graphene/PEDOT:PSS Nanocomposites

The electrical conductivity of epoxy resin is too low for a high power factor. Therefore, an intrinsically conductive polymer, PEDOT:PSS, was used for the preparation of the composite. For a better understanding of the relationship between the power factor, the weight percent of fillers in composite, and the weight percent of C_{60} in fillers, a series of samples were prepared as described in Table 5.1.

Table 5.1 Samples with different weight percent of fillers in composite and different weight percent of C_{60} in fillers

Sample number	Filler weight percent in composite (wt%)	C_{60} weight percent in filler (wt%)
A	70	10
B	50	10
C	30	10
C2	30	30
C3	30	50
C4	30	80
C5	30	90

The electrical conductivity, Seebeck coefficient and power factors of samples with 30, 50, and 70 wt% filler (Sample A, B, C) were shown in Figure 5.2. Pristine PEDOT:PSS possessed a Seebeck coefficient of ~18 μVK^{-1} and an electrical conductivity of ~70,000 Sm^{-1}. With the addition of the C_{60}/graphene fillers, the Seebeck coefficient steadily increased. With 70 wt% filler, the Seebeck coefficient increased 40% to 25.4

μVK^{-1}. The Seebeck coefficient of PEDOT:PSS is positive, indicating that it is a p-type material with positive charged holes. While C_{60} is a n-type material, the incorporation of C_{60} might result in the decrease of carrier concentration [308]. The decreased hole concentration might push the Fermi level away from the valance band, resulting in an increased Seebeck coefficient [312]. Another possible reason might be that the nanoscale C_{60} nanoparticles could generate an energy-filtering effect which preferentially allows high-energy carriers to pass while blocking low-energy carriers. Hence, it will increase the mean carrier energy in electronic transport with an enhanced Seebeck coefficient [297, 313]

According to the electrical conductivities of the composites presented in Figure 5.2a, higher filler loading resulted in decreased electrical conductivity. In the composite, the weight loading of C_{60} is lower than the reduced graphene and PEDOT:PSS. Since oxygen or moisture may dope on graphene films, the charge transport is dominated by holes. Together with the p-type PEDOT:PSS, the major carrier in the composite was holes. The incorporation of n-type C_{60} would decrease the hole carrier concentration of the composites. The reduced graphene and PEDOT:PSS are p-type materials, while C_{60} is n-type material. The opposite types of carriers will cancel each other and result in the decreased hole concentration.

The power factor of the composites was calculated and presented in Figure 5.2b. The sample with 30 wt% filler showed the highest power factor, which was 50% higher than the power factor of pure PEDOT:PSS. However, the samples with a higher loading of filler possessed a lower power factor, indicating that the decrease in electrical conductivity surpassed the increase in the Seebeck coefficient.

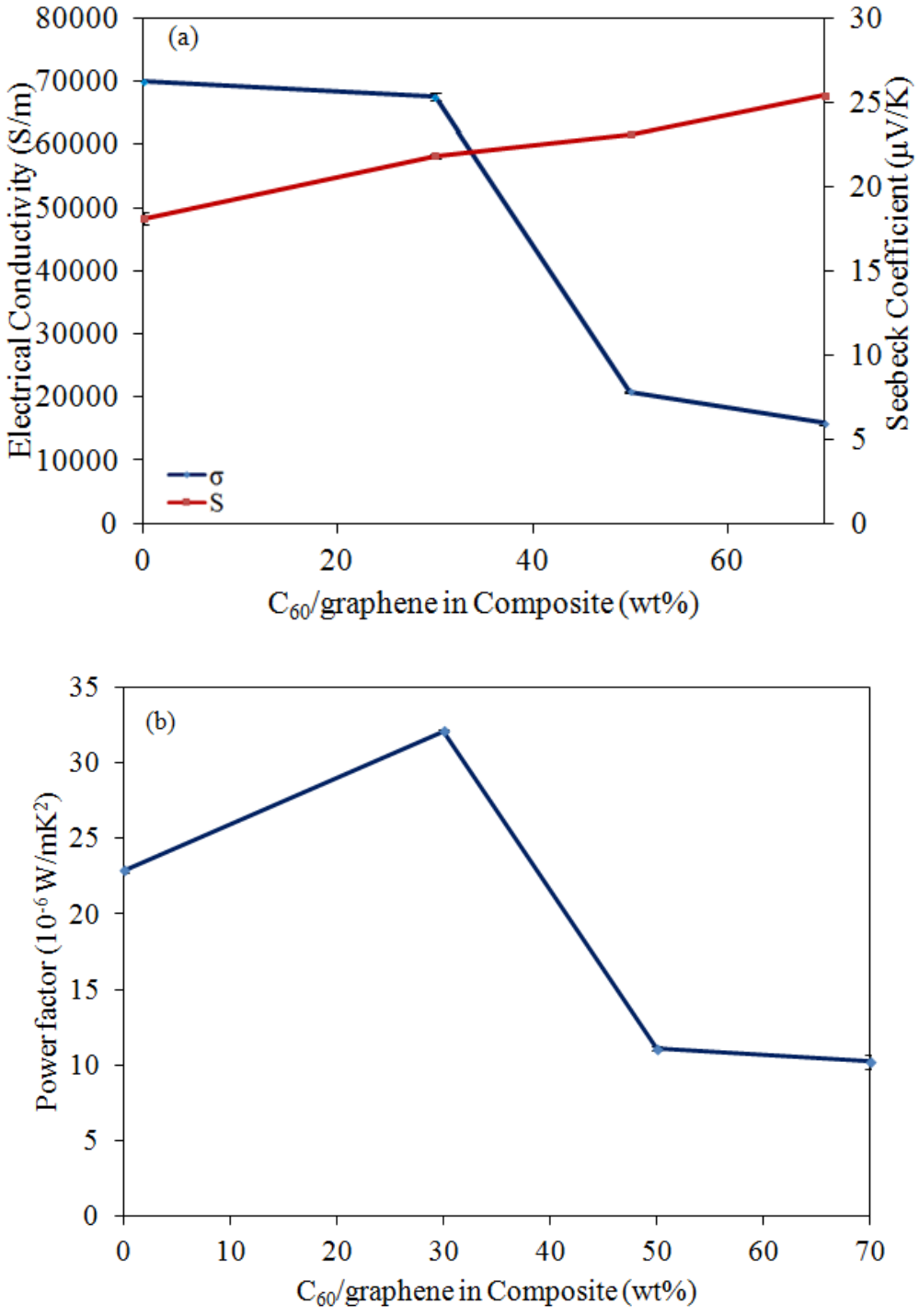

Figure 5.2 (a) Electrical conductivity, Seebeck coefficient, and (b) power factor of the PEDOT:PSS and composites with different load of C_{60}/graphene.

According to the results of composites with different weight percent of fillers, the composite with 30% filler showed better performance. It is necessary to optimize the power factor of the composites by changing the weight percent of C_{60} in fillers. All composites were fabricated with 30 wt% filler. But the weight percent of C_{60} in the filler varied from 10 wt% to 90 wt%. The test results were shown in Figure 5.3. As we can see from Figure 5.3a, the Seebeck coefficient of the composite kept increasing with a higher loading of C_{60}, which is due to the energy-filtering effect of n-type C_{60}. The addition of C_{60} brought more electrons and offset more transport carrier in the composite, which resulted in a decreasing electrical conductivity. The composite with 30 wt% C_{60} in the filler achieved an optimized power factor of 32.4 $\mu W/mK^2$ (Figure 5.3b). It is worth noting that the composite with 10% to 50% C_{60} in the filler had comparable power factors. Further addition of C_{60} resulted in a sharp drop in electrical conductivity and thus a much smaller power factor. Based on these results, we proposed the following structure (Figure 5.4a) of the C_{60}/graphene/PEDOT:PSS composite to explain the electrical performance of this composite. It was found from the TEM images that the C_{60} nanoparticles were mainly located in the middle of the graphene plane (Section 4.7.2). There were less C_{60} nanoparticles on the edge of the graphene plane. When a small amount of C_{60} was used, the coverage of C_{60} on graphene was low. The PEDOT:PSS attached on the surface of graphene through π-π stacking. Two adjacent C_{60}/graphene sheets could be bridged through the PEDOT:PSS which are attached on the edge of both graphene sheets. When the PEDOT:PSS was abundant, the parallel C_{60}/graphene sheets were connected to each other through the PEDOT:PSS grafted in the middle of the graphene plane. The conducting polymer decreased the in-plane and the through-plane electrical resistance of the C_{60}/graphene sheets, and thus kept a higher electrical conductivity of the composite. When more C_{60} were used, the C_{60} coverage on the graphene becomes larger. The through-plane bridging points were replaced by C_{60} nanoparticles which lead to the sharp drop of the electrical conductivity. The circuit scheme was used to illustrate the influence of the C_{60} coverage on the electrical conductivity of the composites as well (Figure 5.4b and 5.4c). When the coverage of C_{60} is low in the composite, the graphene sheets connect

to each other through both the C_{60} and PEDOT:PSS. The electrical resistance between the graphene sheet is the parallel resistance of C_{60} and PEDOT:PSS, which can be expressed as:

$$R_{parallel} = \frac{R_{PEDOT:PSS} + R_{C_{60}}}{R_{PEDOT:PSS} \times R_{C_{60}}}$$

Where, $R_{PEDOT:PSS}$ is the resistance of PEDOT:PSS, R_{C60} is the resistance of C_{60}. When the C_{60} loading was high, the connect points of PEDOT:PSS were replaced by C_{60} nanoparticles. The resistance is equal to the series resistance of PEDOT:PSS and C_{60}, which can be expressed as:

$$R_{series} = R_{PEDOT:PSS} + R_{C_{60}}$$

It is well known that the parallel resistance is smaller than any of the resistance in the circuit, so the $R_{parallel}$ is much smaller than the R_{series}. Therefore, the samples with more C_{60} showed a much lower electrical conductivity.

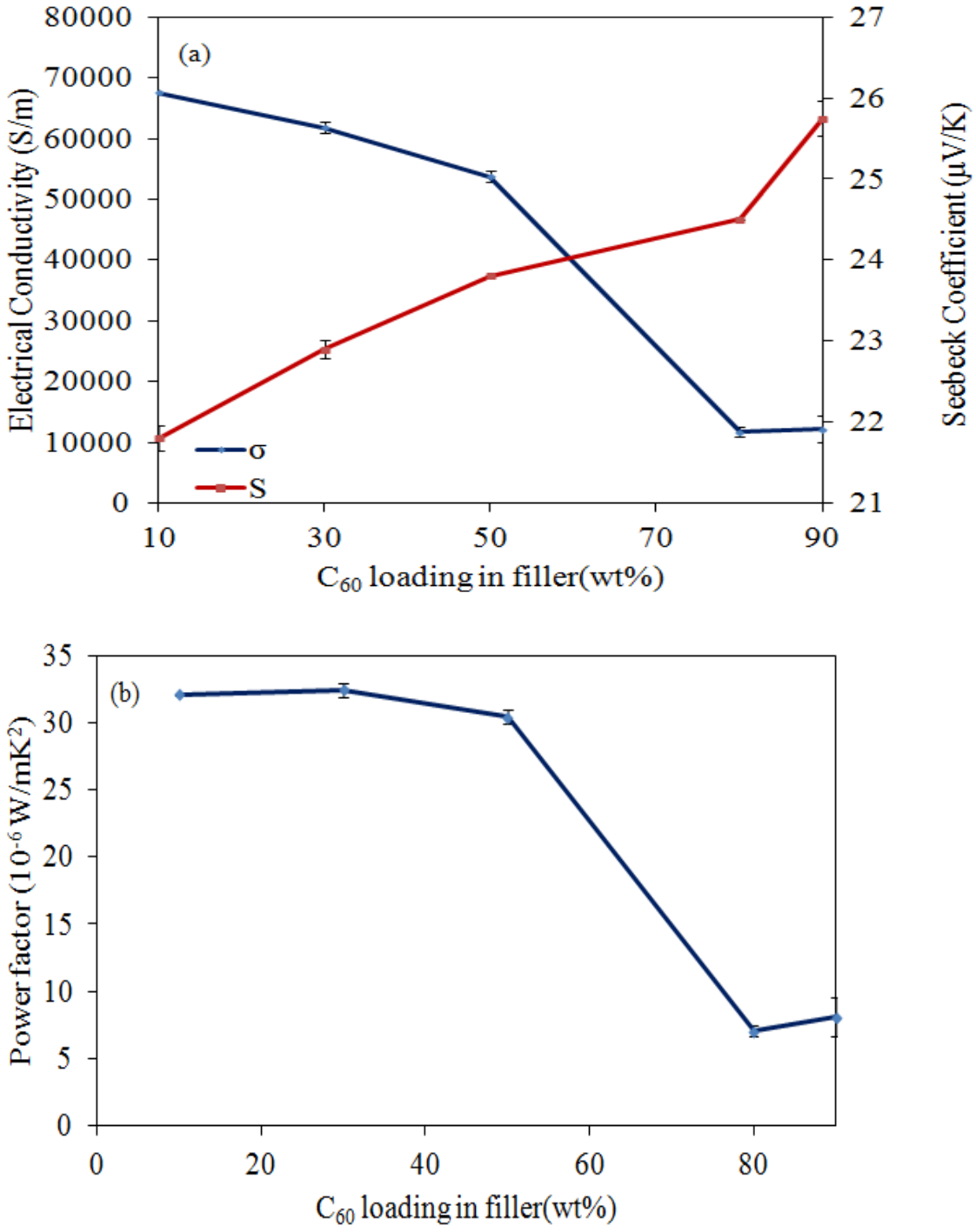

Figure 5.3 (a) Electrical conductivity, Seebeck coefficient, and (b) power factor of the composites composing fillers with different weight percent of C_{60}.

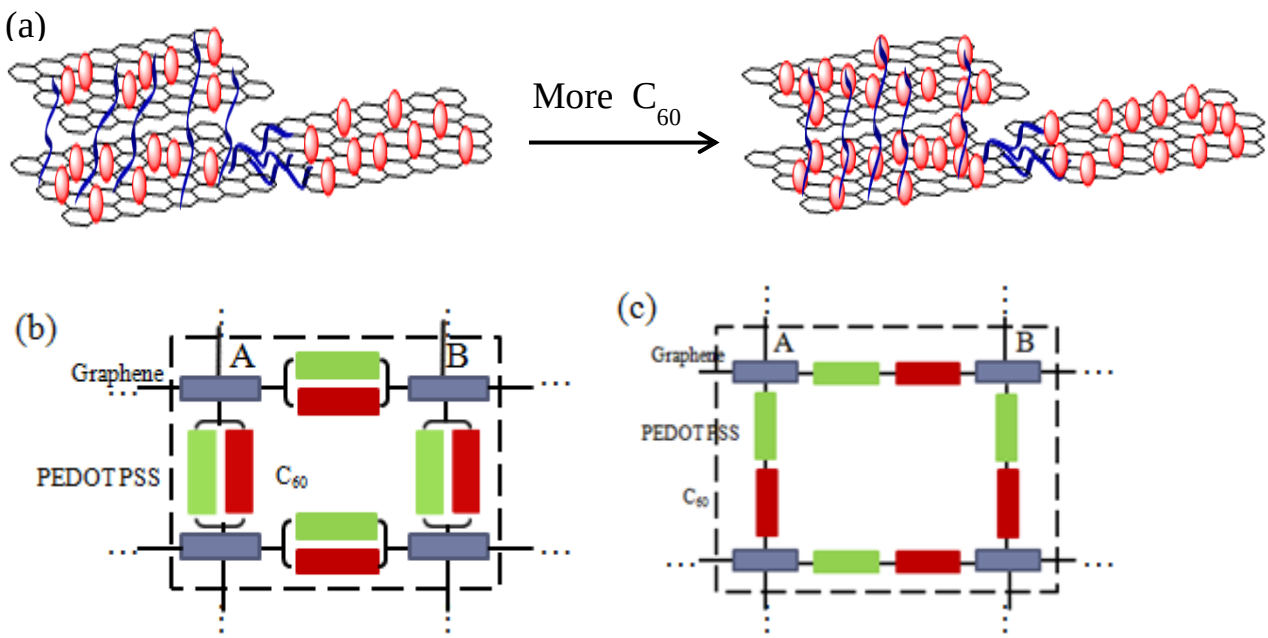

Figure 5.4 (a) Scheme illustrates the influence of C_{60} coverage on the electrical conductivity of the C_{60}/graphene/PEDOT:PSS composite. (b) The circuit conducting analogue schematic of composite with less C_{60}. (c) The circuit conducting analogue schematic of composite with more C_{60}. (Purple: graphene, green: PEDOT:PSS, red: C_{60}).

5.5 Summary

The electrical conductivity of epoxy was increased by incorporating the C_{60}/graphene nanostructures. By increasing the weight percent of C_{60}/graphene in the composite, the Seebeck coefficient decreased due to a higher carrier concentration. The C_{60}/graphene/epoxy nanocomposites achieved an optimized power factor of 1.1 $\mu W/K^2m$ by adding 45 wt% of the nanostructures. However, due to a low electrical conductivity, the power factor was not ideal.

The C_{60}/graphene/PEDOT:PSS composite showed a much higher electrical conductivity. By properly adjusting the filler loading in composite, the power factor of the composite was improved. The power factor was further improved by tuning the weight percent of C_{60} in filler. The composite with 30 wt% filler and 30 wt% C_{60} in filler achieved an optimized power factor of 32.4 $\mu W/mK^2$, which was 50% higher than the

power factor of PEDOT:PSS. This work will provide guidance to effectively enhance the power factor of polymer by adding different loading of C_{60}/graphene nanostructures.

Chapter VI

Conclusion and Future Work

6.1 Conclusions

The nanoparticles/graphene hierarchical nanostructure has demonstrated promising applications in the field of catalysis, energy, and biotechnology. Especially, the development of clean and renewable energy resources to improve the quality of environment is one of the most promising directions in the research of the hierarchical nanostructure materials.

However, to date, the wide application of the nanoparticles/graphene hierarchical nanostructure has been hindered due to several technical challenges, such as a lack of methods to effectively fabricate the nanoparticles/graphene hierarchical nanostructure and a limited understanding of the processing-structure-property relationship of the hierarchical nanostructure.

To solve these technical issues, three methods were studied to fabricate silver nanoparticles/graphene and C_{60}/graphene nanostructures, and the processing-structure-property relationship of these materials was well investigated.

Silver nanoparticles were successfully synthesized on graphene layers through electrostatic attraction, followed by a simultaneous thermal reduction of graphene oxide and silver ions. The weight percent of silver particles on graphene was tuned by adjusting the concentration of silver salt solution. The nitrogen adsorption/desorption tests indicated that the Ag NPs played an essential role in preventing graphene layers from restacking and aggregating, resulting in larger active surface areas. Since Ag NPs acted as an electrical bridge between graphene layers, the electrical conductivity of the Ag NPs/graphene continuously increased with higher weight percent of Ag NPs. Due to the increasing surface area and electrical conductivity, the Ag NPs/graphene hierarchical materials showed an enhanced specific capacitance when compared with as-fabricated

graphene. The improved properties indicate that silver-functionalized graphene is promising for electrode materials in high-performance supercapacitors.

Zero dimensional fullerene was also incorporated with graphene layers through covalent method. The characterizations by FT-IR spectroscopy, UV–Vis spectroscopy, atomic force microscopy, and transmission electron microscopy have confirmed the successful grafting of fullerene on graphene. The integration of fullerene created an effective route to introduce new functionalities and prevent the restacking of graphene.

A faster and cheaper non-covalent method was used to functionalize graphene with C_{60} nanoparticles. The UV/Vis spectroscopy, Raman spectroscopy and X-ray diffraction have proved the formation of C_{60}/graphene hierarchical nanostructures. The research also indicated that the particle size of the grafted C_{60} nanoparticles can be effectively tuned by adjusting the concentration of the C_{60} solution. A larger average particle size and size distribution were observed in the samples using C_{60} solution of higher concentrations.

The C_{60}/graphene hierarchical materials were incorporated with two different polymers to study their influence on the power factor of the composites. The C_{60}/graphene hierarchical nanostructures increased the electrical conductivity of the epoxy resin. The Seebeck coefficient of the composites decreased with higher weight percent of the hierarchical nanostructure due to an increasing carrier concentration. Due to the low electrical conductivity of the epoxy resin, the power factor of the epoxy composite is not promising, and a power factor of 1.1 $\mu W/K^2m$ was achieved by incorporating 45 wt% hierarchical nanostructures in the composites. To solve this, a conducting polymer, PEDOT:PSS, was used for preparing the composite. A higher electrical conductivity was observed in the C_{60}/graphene/PEDOT:PSS composite. With increasing C_{60}/graphene loading, an enhanced Seebeck coefficient was achieved by the energy-filtering effect at the interface of the filler and matrix. By properly adjusting the weight ratio between the C_{60}, graphene, and PEDOT:PSS , an optimal power factor of 32.4 $\mu W/K^2m$ was achieved.

6.2 Future Work

1. The reduction level of graphene can significantly influence the band gap of the reduced graphene [314]. Through adjusting the weight percentage of the oxygen-containing groups on the reduced graphene, the band gap of the reduced graphene can be tuned from 1 to 3.5 eV [314].

When prepared nanocomposite, nanostructured interface are formed between the filler and the matrix. The interface may work as an energy-filter which scatters low-energy carriers, allowing high-energy carriers transport between the filter and the matrix. The energy-filtering effect can enhance the Seebeck coefficient but decrease the electrical conductivity. An interfacial barrier height in the range of 40 to 100 meV is preferred to promote the Seebeck coefficient without greatly suppressing the electrical conductivity [315]. For reduced graphene/polymer nanocomposite, the interfacial barrier height is the difference between the highest occupied molecular orbital (HOMO) of reduced graphene and polymer matrix. The HOMO of reduced graphene is determined by the band gap of the materials. Thus the interfacial barrier height of the graphene/polymer nanocomposite can be tuned by adjusting the reduction level of graphene.

The reduction level of graphene can be tuned by adjusting the type of reducing agent, reducing time, concentration of reducing agent and reducing temperatures. The HOMO of reduced graphene and polymer matrix can be calculated from cyclic voltammetry measurements [316]. Through properly tuning the interfacial barrier height between graphene and polymer, an optimal power factor of the nanocomposites can be achieved.

2. Study the relationship between morphology of polymer matrix in composites and the thermoelectric performance of the composite. For most conducting polymers, the carrier transport is primarily controlled by the interchain and intrachain hopping processes. Typically, an aligned and ordered polymer chain would result in a reduced barrier of both interchain hopping and intrachain hopping, and thus increase the carrier

mobility [317]. The increased carrier mobility can enhance the electrical conductivity and Seebeck coefficient simultaneously [7].

Template-direct synthesis is one of the most effective ways of producing ordered polymer. For example, CNTs worked as template of producing 1D order PANI nanostructure. The strong π-π interaction between the CNTs' surface and PANI molecules benefited the growing of ordered PANI chains along the surface of CNTs [7].

Conducting polymers, including polyaniline, polypyrrole, polythiophenes, poly(3-methylthiophene), poly(3,4-ethylenedioxythiophene):polystyrene sulphonate, all contain aromatic rings that can form π-π interaction between polymer and graphene. Study of the template effect of graphene on growing these polymers should be considered. The nanostructure of the polymers can be tuned by adjusting the weight ratio of monomer to initiator, the weight ratio of polymer to graphene, and synthesis temperatures. The developed arrangement of the polymers on graphene can be characterized by X-ray diffraction spectroscopy. The carrier mobility, carrier density can be measured by a quantum design physics property measurement system [7]. Thus the relationship between the nanostructure of polymer matrix in composites and the thermoelectric performance of the composite can be studied and utilized to optimize the thermoelectric performance of the composite.

References

[1] Lee C, Wei XD, Kysar JW, Hone J. Measurement of the elastic properties and intrinsic strength of monolayer graphene. Science. 2008;321(5887):385-8.

[2] Ghosh S, Calizo I, Teweldebrhan D, Pokatilov EP, Nika DL, Balandin AA, et al. Extremely high thermal conductivity of graphene: Prospects for thermal management applications in nanoelectronic circuits. Appl Phys Lett. 2008;92(15).

[3] Balandin AA, Ghosh S, Bao WZ, Calizo I, Teweldebrhan D, Miao F, et al. Superior thermal conductivity of single-layer graphene. Nano Lett. 2008;8(3):902-7.

[4] Bolotin KI, Sikes KJ, Jiang Z, Klima M, Fudenberg G, Hone J, et al. Ultrahigh electron mobility in suspended graphene. Solid State Commun. 2008;146(9-10):351-5.

[5] Stoller MD, Park SJ, Zhu YW, An JH, Ruoff RS. Graphene-Based Ultracapacitors. Nano Lett. 2008;8(10):3498-502.

[6] Katsnelson MI. Graphene: carbon in two dimensions. Mater Today. 2007;10(1-2):20-7.

[7] Yao Q, Chen LD, Zhang WQ, Liufu SC, Chen XH. Enhanced Thermoelectric Performance of Single-Walled Carbon Nanotubes/Polyaniline Hybrid Nanocomposites. Acs Nano. 2010;4(4):2445-51.

[8] Si YC, Samulski ET. Exfoliated Graphene Separated by Platinum Nanoparticles. Chem Mater. 2008;20(21):6792-7.

[9] Rai M, Yadav A, Gade A. Silver nanoparticles as a new generation of antimicrobials. Biotechnol Adv. 2009;27(1):76-83.

[10] Sosa IO, Noguez C, Barrera RG. Optical properties of metal nanoparticles with arbitrary shapes. J Phys Chem B. 2003;107(26):6269-75.

[11] Bai S, Shen XP. Graphene-inorganic nanocomposites. Rsc Adv. 2012;2(1):64-98.

[12] Sun YQ, Wu QO, Shi GQ. Graphene based new energy materials. Energ Environ Sci. 2011;4(4):1113-32.

[13] Huang X, Qi XY, Boey F, Zhang H. Graphene-based composites. Chem Soc Rev. 2012;41(2):666-86.

[14] Geim AK, Novoselov KS. The rise of graphene. Nat Mater. 2007;6(3):183-91.

[15] http://www.andrew.cmu.edu/user/feenstra/graphene/.

[16] Meyer JC, Geim AK, Katsnelson MI, Novoselov KS, Booth TJ, Roth S. The structure of suspended graphene sheets. Nature. 2007;446(7131):60-3.

[17] Fasolino A, Los JH, Katsnelson MI. Intrinsic ripples in graphene. Nat Mater. 2007;6(11):858-61.

[18] Zhu YW, Murali S, Cai WW, Li XS, Suk JW, Potts JR, et al. Graphene and Graphene Oxide: Synthesis, Properties, and Applications. Adv Mater. 2010;22(35):3906-24.

[19] Novoselov KS, Geim AK, Morozov SV, Jiang D, Zhang Y, Dubonos SV, et al. Electric field effect in atomically thin carbon films. Science. 2004;306(5696):666-9.

[20] Novoselov KS, Geim AK, Morozov SV, Jiang D, Katsnelson MI, Grigorieva IV, et al. Two-dimensional gas of massless Dirac fermions in graphene. Nature. 2005;438(7065):197-200.

[21] Morozov SV, Novoselov KS, Katsnelson MI, Schedin F, Elias DC, Jaszczak JA, et al. Giant intrinsic carrier mobilities in graphene and its bilayer. Phys Rev Lett. 2008;100(1).

[22] Cai DY, Yusoh K, Song M. The mechanical properties and morphology of a graphite oxide nanoplatelet/polyurethane composite. Nanotechnology. 2009;20(8).

[23] Frank IW, Tanenbaum DM, Van der Zande AM, McEuen PL. Mechanical properties of suspended graphene sheets. J Vac Sci Technol B. 2007;25(6):2558-61.

[24] Dikin DA, Stankovich S, Zimney EJ, Piner RD, Dommett GHB, Evmenenko G, et al. Preparation and characterization of graphene oxide paper. Nature. 2007;448(7152):457-60.

[25] Nair RR, Blake P, Grigorenko AN, Novoselov KS, Booth TJ, Stauber T, et al. Fine structure constant defines visual transparency of graphene. Science. 2008;320(5881):1308.

[26] Blake P, Brimicombe PD, Nair RR, Booth TJ, Jiang D, Schedin F, et al. Graphene-based liquid crystal device. Nano Lett. 2008;8(6):1704-8.

[27] Chen JH, Ishigami M, Jang C, Hines DR, Fuhrer MS, Williams ED. Printed graphene circuits. Adv Mater. 2007;19(21):3623-27.

[28] Gusynin VP, Sharapov SG, Carbotte JP. Unusual microwave response of Dirac quasiparticles in graphene. Phys Rev Lett. 2006;96(25).

[29] Seol JH, Jo I, Moore AL, Lindsay L, Aitken ZH, Pettes MT, et al. Two-Dimensional Phonon Transport in Supported Graphene. Science. 2010;328(5975):213-6.

[30] Charrier A, Coati A, Argunova T, Thibaudau F, Garreau Y, Pinchaux R, et al. Solid-state decomposition of silicon carbide for growing ultra-thin heteroepitaxial graphite films. J Appl Phys. 2002;92(5):2479-84.

[31] Forbeaux I, Themlin JM, Debever JM. Heteroepitaxial graphite on 6H-SiC(0001): Interface formation through conduction-band electronic structure. Phys Rev B. 1998;58(24):16396-406.

[32] Forbeaux I, Themlin JM, Debever JM. High-temperature graphitization of the 6H-SiC (000(1)over-bar) face. Surf Sci. 1999;442(1):9-18.

[33] Singh V, Joung D, Zhai L, Das S, Khondaker SI, Seal S. Graphene based materials: Past, present and future. Prog Mater Sci. 2011;56(8):1178-271.

[34] Soldano C, Mahmood A, Dujardin E. Production, properties and potential of graphene. Carbon. 2010;48(8):2127-50.

[35] Yoshinobu T, Izumikawa I, Mitsui H, Fuyuki T, Matsunami H. Dynamic Reflection High-Energy Electron-Diffraction Observation of 3c-Sic(001) Surface Reconstruction under Si2h6 Beam Irradiation. Appl Phys Lett. 1991;59(22):2844-6.

[36] Jariwala D, Srivastava A, Ajayan PM. Graphene Synthesis and Band Gap Opening. J Nanosci Nanotechno. 2011;11(8):6621-41.

[37] Ueta HS, M.; Nakai, C.; Yamada, Y.; Sasaki, M.; Yamamoto, S. Highly oriented monolayer graphite formation on Pt(111) by a supersonic methane beam. Surf Sci. 2004;560((1-3)):183-90.

[38] Coraux J, N'Diaye AT, Busse C, Michely T. Structural coherency of graphene on Ir(111). Nano Lett. 2008;8(2):565-70.

[39] de Parga ALV, Calleja F, Borca B, Passeggi MCG, Hinarejos JJ, Guinea F, et al. Periodically rippled graphene: Growth and spatially resolved electronic structure. Phys Rev Lett. 2008;100(5).

[40] Marchini S, Gunther S, Wintterlin J. Scanning tunneling microscopy of graphene on Ru(0001). Phys Rev B. 2007;76(7).

[41] Gamo Y, Nagashima A, Wakabayashi M, Terai M, Oshima C. Atomic structure of monolayer graphite formed on Ni(111). Surf Sci. 1997;374(1-3):61-4.

[42] Somani PR, Somani SP, Umeno M. Planer nano-graphenes from camphor by CVD. Chem Phys Lett. 2006;430(1-3):56-9.

[43] Chae SJ, Gunes F, Kim KK, Kim ES, Han GH, Kim SM, et al. Synthesis of Large-Area Graphene Layers on Poly-Nickel Substrate by Chemical Vapor Deposition: Wrinkle Formation. Adv Mater. 2009;21(22):2328-33.

[44] Li XS, Cai WW, Colombo L, Ruoff RS. Evolution of Graphene Growth on Ni and Cu by Carbon Isotope Labeling. Nano Lett. 2009;9(12):4268-72.

[45] Bae S, Kim H, Lee Y, Xu XF, Park JS, Zheng Y, et al. Roll-to-roll production of 30-inch graphene films for transparent electrodes. Nat Nanotechnol. 2010;5(8):574-8.

[46] Wu JS, Tomovic Z, Enkelmann V, Mullen K. From branched hydrocarbon propellers to C-3-symmetric graphite disks. (Vol 69, pg 5179, 2004). J Org Chem. 2004;69(23):8176-86.

[47] Simpson CD, Brand JD, Berresheim AJ, Przybilla L, Rader HJ, Mullen K. Synthesis of a giant 222 carbon graphite sheet. Chem-Eur J. 2002;8(6):1424-9.

[48] Wu JS, Pisula W, Mullen K. Graphenes as potential material for electronics. Chem Rev. 2007;107(3):718-47.

[49] Wu JS, Tomovic Z, Enkelmann V, Mullen Y. From branched hydrocarbon propellers to C-3-symmetric graphite disks. J Org Chem. 2004;69(16):5179-86.

[50] Sakamoto J, van Heijst J, Lukin O, Schluter AD. Two-Dimensional Polymers: Just a Dream of Synthetic Chemists? Angew Chem Int Edit. 2009;48(6):1030-69.

[51] Yang XY, Dou X, Rouhanipour A, Zhi LJ, Rader HJ, Mullen K. Two-dimensional graphene nanoribbons. J Am Chem Soc. 2008;130(13):4216-7.

[52] Cai JM, Ruffieux P, Jaafar R, Bieri M, Braun T, Blankenburg S, et al. Atomically precise bottom-up fabrication of graphene nanoribbons. Nature. 2010;466(7305):470-3.

[53] Zhang YB, Small JP, Pontius WV, Kim P. Fabrication and electric-field-dependent transport measurements of mesoscopic graphite devices. Appl Phys Lett. 2005;86(7).

[54] Ci LJ, Song L, Jariwala D, Elias AL, Gao W, Terrones M, et al. Graphene Shape Control by Multistage Cutting and Transfer. Adv Mater. 2009;21(44):4487-91.

[55] Song L, Ci LJ, Gao W, Ajayan PM. Transfer Printing of Graphene Using Gold Film. Acs Nano. 2009;3(6):1353-6.

[56] Liang XG, Chang ASP, Zhang YG, Harteneck BD, Choo H, Olynick DL, et al. Electrostatic Force Assisted Exfoliation of Prepatterned Few-Layer Graphenes into Device Sites. Nano Lett. 2009;9(1):467-472.

[57] Lu XK, Yu MF, Huang H, Ruoff RS. Tailoring graphite with the goal of achieving single sheets. Nanotechnology. 1999;10(3):269-72.

[58] Liu XJ, Pan LK, Zhao QF, Lv T, Zhu G, Chen TQ, et al. UV-assisted photocatalytic synthesis of ZnO-reduced graphene oxide composites with enhanced photocatalytic activity in reduction of Cr(VI). Chem Eng J. 2012;183:238-43.

[59] Ishigami M, Chen JH, Cullen WG, Fuhrer MS, Williams ED. Atomic structure of graphene on SiO2. Nano Lett. 2007;7(6):1643-8.

[60] Giordani S, Colomer JF, Cattaruzza F, Alfonsi J, Meneghetti M, Prato M, et al. Multifunctional hybrid materials composed of [60]fullerene-based functionalized-single-walled carbon nanotubes. Carbon. 2009;47(3):578-88.

[61] Moser J, Barreiro A, Bachtold A. Current-induced cleaning of graphene. Appl Phys Lett. 2007;91(16).

[62] Sidorov AN, Yazdanpanah MM, Jalilian R, Ouseph PJ, Cohn RW, Sumanasekera GU. Electrostatic deposition of graphene. Nanotechnology. 2007;18(13).

[63] Shukla A, Kumar R, Mazher J, Balan A. Graphene made easy: High quality, large-area samples. Solid State Commun. 2009;149(17-18):718-21.

[64] Si Y, Samulski ET. Synthesis of water soluble graphene. Nano Lett. 2008;8(6):1679-82.

[65] Schniepp HC, Li JL, McAllister MJ, Sai H, Herrera-Alonso M, Adamson DH, et al. Functionalized single graphene sheets derived from splitting graphite oxide. J Phys Chem B. 2006;110(17):8535-9.

[66] Jung I, Dikin DA, Piner RD, Ruoff RS. Tunable Electrical Conductivity of Individual Graphene Oxide Sheets Reduced at "Low" Temperatures. Nano Lett. 2008;8(12):4283-7.

[67] Becerril HA, Mao J, Liu Z, Stoltenberg RM, Bao Z, Chen Y. Evaluation of solution-processed reduced graphene oxide films as transparent conductors. Acs Nano. 2008;2(3):463-70.

[68] Ambrosi A, Bonanni A, Sofer Z, Cross JS, Pumera M. Electrochemistry at Chemically Modified Graphenes. Chem-Eur J. 2011;17(38):10763-70.

[69] Brodie B. Sur le poids atomique du graphite. Ann Chim Phys. 1860;59:466-72.

[70] William S. Hummers Jr. REO. Preparation of Graphitic Oxide. J Am Chem Soc. 1958;80(6):1339.

[71] Staudenmaier L. Verfahren zur darstellung der graphitsaure. Ber Dtsch ChemGes. 1898;31:1481–99.

[72] Brodie BC. On the Atomic Weight of Graphite. Philosophical Transactions of the Royal Society of London. 1859;149:249-59.

[73] He HY, Klinowski J, Forster M, Lerf A. A new structural model for graphite oxide. Chemical Physics Letters. 1998;287(1-2):53-6.

[74] He HY, Riedl T, Lerf A, Klinowski J. Solid-state NMR studies of the structure of graphite oxide. J Phys Chem-Us. 1996;100(51):19954-8.

[75] Lerf A, He HY, Forster M, Klinowski J. Structure of graphite oxide revisited. J Phys Chem B. 1998;102(23):4477-82.

[76] Cai WW, Piner RD, Stadermann FJ, Park S, Shaibat MA, Ishii Y, et al. Synthesis and solid-state NMR structural characterization of (13)C-labeled graphite oxide. Science. 2008;321(5897):1815-7.

[77] Cabria I, Lopez MJ, Alonso JA. Theoretical study of the transition from planar to three-dimensional structures of palladium clusters supported on graphene. Phys Rev B. 2010;81(3).

[78] McAllister MJ, Li JL, Adamson DH, Schniepp HC, Abdala AA, Liu J, et al. Single sheet functionalized graphene by oxidation and thermal expansion of graphite. Chem Mater. 2007;19(18):4396-404.

[79] Li JL, Kudin KN, McAllister MJ, Prud'homme RK, Aksay IA, Car R. Oxygen-driven unzipping of graphitic materials. Phys Rev Lett. 2006;96(17).

[80] Chen GH, Weng WG, Wu DJ, Wu CL, Lu JR, Wang PP, et al. Preparation and characterization of graphite nanosheets from ultrasonic powdering technique. Carbon. 2004;42(4):753-9.

[81] Jang BZW, S. C.; Bai, Y. Low-temperature method of producing nano-scaled graphene platelets and their nanocomposites. US Patent Appl No 10/ 858,814. 2005;Pub. No. US 2005/0271574.

[82] Yang D, Velamakanni A, Bozoklu G, Park S, Stoller M, Piner RD, et al. Chemical analysis of graphene oxide films after heat and chemical treatments by X-ray photoelectron and Micro-Raman spectroscopy. Carbon. 2009;47(1):145-52.

[83] Bagri A, Mattevi C, Acik M, Chabal YJ, Chhowalla M, Shenoy VB. Structural evolution during the reduction of chemically derived graphene oxide. Nat Chem. 2010;2(7):581-7.

[84] Jelea A, Marinelli F, Ferro Y, Allouche A, Brosset C. Quantum study of hydrogen-oxygen-graphite interactions. Carbon. 2004;42(15):3189-98.

[85] Mao S, Pu HH, Chen JH. Graphene oxide and its reduction: modeling and experimental progress. Rsc Adv. 2012;2(7):2643-62.

[86] Stankovich S, Dikin DA, Piner RD, Kohlhaas KA, Kleinhammes A, Jia Y, et al. Synthesis of graphene-based nanosheets via chemical reduction of exfoliated graphite oxide. Carbon. 2007;45(7):1558-65.

[87] Chen H, Muller MB, Gilmore KJ, Wallace GG, Li D. Mechanically strong, electrically conductive, and biocompatible graphene paper. Adv Mater. 2008;20(18):3557-61.

[88] Shin HJ, Kim KK, Benayad A, Yoon SM, Park HK, Jung IS, et al. Efficient Reduction of Graphite Oxide by Sodium Borohydrilde and Its Effect on Electrical Conductance. Adv Funct Mater. 2009;19(12):1987-92.

[89] Gao W, Alemany LB, Ci LJ, Ajayan PM. New insights into the structure and reduction of graphite oxide. Nat Chem. 2009;1(5):403-8.

[90] Fan ZJ, Kai W, Yan J, Wei T, Zhi LJ, Feng J, et al. Facile Synthesis of Graphene Nanosheets via Fe Reduction of Exfoliated Graphite Oxide. Acs Nano. 2011;5(1):191-8.

[91] Fan ZJ, Wang K, Wei T, Yan J, Song LP, Shao B. An environmentally friendly and efficient route for the reduction of graphene oxide by aluminum powder. Carbon. 2010;48(5):1686-9.

[92] Mei XG, Ouyang JY. Ultrasonication-assisted ultrafast reduction of graphene oxide by zinc powder at room temperature. Carbon. 2011;49(15):5389-97.

[93] Stankovich S, Piner RD, Chen XQ, Wu NQ, Nguyen ST, Ruoff RS. Stable aqueous dispersions of graphitic nanoplatelets via the reduction of exfoliated graphite oxide in the presence of poly(sodium 4-styrenesulfonate). J Mater Chem. 2006;16(2):155-8.

[94] Lomeda JR, Doyle CD, Kosynkin DV, Hwang WF, Tour JM. Diazonium Functionalization of Surfactant-Wrapped Chemically Converted Graphene Sheets. J Am Chem Soc. 2008;130(48):16201-6.

[95] Allen MJ, Tung VC, Kaner RB. Honeycomb Carbon: A Review of Graphene. Chem Rev. 2010;110(1):132-45.

[96] Li D, Muller MB, Gilje S, Kaner RB, Wallace GG. Processable aqueous dispersions of graphene nanosheets. Nat Nanotechnol. 2008;3(2):101-5.

[97] Fernandez-Merino MJ, Guardia L, Paredes JI, Villar-Rodil S, Solis-Fernandez P, Martinez-Alonso A, et al. Vitamin C Is an Ideal Substitute for Hydrazine in the Reduction of Graphene Oxide Suspensions. J Phys Chem C. 2010;114(14):6426-32.

[98] Park S, An JH, Jung IW, Piner RD, An SJ, Li XS, et al. Colloidal Suspensions of Highly Reduced Graphene Oxide in a Wide Variety of Organic Solvents. Nano Lett. 2009;9(4):1593-7.

[99] Viet HP, Tran VC, Nguyen-Phan TD, Hai DP, Kim EJ, Hur SH, et al. One-step synthesis of superior dispersion of chemically converted graphene in organic solvents. Chem Commun. 2010;46(24):4375-7.

[100] Park S, An JH, Piner RD, Jung I, Yang DX, Velamakanni A, et al. Aqueous Suspension and Characterization of Chemically Modified Graphene Sheets. Chem Mater. 2008;20(21):6592-4.

[101] Moon IK, Lee J, Ruoff RS, Lee H. Reduced graphene oxide by chemical graphitization. Nat Commun. 2010;1.

[102] Wu ZS, Ren WC, Gao LB, Liu BL, Jiang CB, Cheng HM. Synthesis of high-quality graphene with a pre-determined number of layers. Carbon. 2009;47(2):493-9.

[103] Jin MH, Kim TH, Lim SC, Duong DL, Shin HJ, Jo YW, et al. Facile Physical Route to Highly Crystalline Graphene. Adv Funct Mater. 2011;21(18):3496-501.

[104] Cote LJ, Cruz-Silva R, Huang JX. Flash Reduction and Patterning of Graphite Oxide and Its Polymer Composite. J Am Chem Soc. 2009;131(31):11027-32.

[105] Chen WF, Yan LF, Bangal PR. Preparation of graphene by the rapid and mild thermal reduction of graphene oxide induced by microwaves. Carbon. 2010;48(4):1146-52.

[106] Zhu YW, Murali S, Stoller MD, Velamakanni A, Piner RD, Ruoff RS. Microwave assisted exfoliation and reduction of graphite oxide for ultracapacitors. Carbon. 2010;48(7):2118-22.

[107] Bi H, Huang FQ, Zhao W, Lu XJ, Chen J, Lin TQ, et al. The production of large bilayer hexagonal graphene domains by a two-step growth process of segregation and surface-catalytic chemical vapor deposition. Carbon. 2012;50(8):2703-9.

[108] Yu YJ, Zhao Y, Ryu S, Brus LE, Kim KS, Kim P. Tuning the Graphene Work Function by Electric Field Effect. Nano Lett. 2009;9(10):3430-4.

[109] Lin TQ, Huang FQ, Liang J, Wang YX. A facile preparation route for boron-doped graphene, and its CdTe solar cell application. Energ Environ Sci. 2011;4(3):862-5.

[110] Li XL, Wang XR, Zhang L, Lee SW, Dai HJ. Chemically derived, ultrasmooth graphene nanoribbon semiconductors. Science. 2008;319(5867):1229-32.

[111] Schedin F, Geim AK, Morozov SV, Hill EW, Blake P, Katsnelson MI, et al. Detection of individual gas molecules adsorbed on graphene. Nat Mater. 2007;6(9):652-5.

[112] Tapaszto L, Dobrik G, Lambin P, Biro LP. Tailoring the atomic structure of graphene nanoribbons by scanning tunnelling microscope lithography. Nat Nanotechnol. 2008;3(7):397-401.

[113] Elias AL, Botello-Mendez AR, Meneses-Rodriguez D, Gonzalez VJ, Ramirez-Gonzalez D, Ci L, et al. Longitudinal Cutting of Pure and Doped Carbon Nanotubes to Form Graphitic Nanoribbons Using Metal Clusters as Nanoscalpels. Nano Lett. 2010;10(2):366-72.

[114] Morelos-Gomez A, Vega-Diaz SM, Gonzalez VJ, Tristan-Lopez F, Cruz-Silva R, Fujisawa K, et al. Clean Nanotube Unzipping by Abrupt Thermal Expansion of Molecular Nitrogen: Graphene Nanoribbons with Atomically Smooth Edges. Acs Nano. 2012;6(3):2261-72.

[115] Kosynkin DV, Higginbotham AL, Sinitskii A, Lomeda JR, Dimiev A, Price BK, et al. Longitudinal unzipping of carbon nanotubes to form graphene nanoribbons. Nature. 2009;458(7240):872-5.

[116] Cano-Marquez AG, Rodriguez-Macias FJ, Campos-Delgado J, Espinosa-Gonzalez CG, Tristan-Lopez F, Ramirez-Gonzalez D, et al. Ex-MWNTs: Graphene Sheets and Ribbons Produced by Lithium Intercalation and Exfoliation of Carbon Nanotubes. Nano Lett. 2009;9(4):1527-33.

[117] Jiao LY, Zhang L, Wang XR, Diankov G, Dai HJ. Narrow graphene nanoribbons from carbon nanotubes. Nature. 2009;458(7240):877-80.

[118] Jiao LY, Wang XR, Diankov G, Wang HL, Dai HJ. Facile synthesis of high-quality graphene nanoribbons. Nat Nanotechnol. 2010;5(5):321-5.

[119] Pillai ZS, Kamat PV. What factors control the size and shape of silver nanoparticles in the citrate ion reduction method? J Phys Chem B. 2004;108(3):945-51.

[120] Sun YG, Xia YN. Shape-controlled synthesis of gold and silver nanoparticles. Science. 2002;298(5601):2176-9.

[121] Li L, Qin ZY, Wang LF, Liu HJ, Zhu MF. Anchoring alpha-manganese oxide nanocrystallites on multi-walled carbon nanotubes as electrode materials for supercapacitor. J Nanopart Res. 2010;12(7):2349-53.

[122] Lightcap IV, Kosel TH, Kamat PV. Anchoring Semiconductor and Metal Nanoparticles on a Two-Dimensional Catalyst Mat. Storing and Shuttling Electrons with Reduced Graphene Oxide. Nano Lett. 2010;10(2):577-83.

[123] He FA, Fan JT, Ma D, Zhang LM, Leung C, Chan HL. The attachment of Fe3O4 nanoparticles to graphene oxide by covalent bonding. Carbon. 2010;48(11):3139-44.

[124] Lin Y, Zhang K, Chen WF, Liu YD, Geng ZG, Zeng J, et al. Dramatically Enhanced Photoresponse of Reduced Graphene Oxide with Linker-Free Anchored CdSe Nanoparticles. Acs Nano. 2010;4(6):3033-8.

[125] Li BJ, Cao HQ. ZnO@graphene composite with enhanced performance for the removal of dye from water. J Mater Chem. 2011;21(10):3346-9.

[126] Li YJ, Gao W, Ci LJ, Wang CM, Ajayan PM. Catalytic performance of Pt nanoparticles on reduced graphene oxide for methanol electro-oxidation. Carbon. 2010;48(4):1124-30.

[127] Guo SJ, Dong SJ, Wang EK. Three-Dimensional Pt-on-Pd Bimetallic Nanodendrites Supported on Graphene Nanosheet: Facile Synthesis and Used as an Advanced Nanoelectrocatalyst for Methanol Oxidation. Acs Nano. 2010;4(1):547-55.

[128] Rao CV, Reddy ALM, Ishikawa Y, Ajayan PM. Synthesis and electrocatalytic oxygen reduction activity of graphene-supported Pt3Co and Pt3Cr alloy nanoparticles. Carbon. 2011;49(3):931-6.

[129] Kamat PV. Graphene-Based Nanoarchitectures. Anchoring Semiconductor and Metal Nanoparticles on a Two-Dimensional Carbon Support. J Phys Chem Lett. 2010;1(2):520-7.

[130] Bourlinos AB, Gournis D, Petridis D, Szabo T, Szeri A, Dekany I. Graphite oxide: Chemical reduction to graphite and surface modification with primary aliphatic amines and amino acids. Langmuir. 2003;19(15):6050-5.

[131] Bell NJ, Yun HN, Du AJ, Coster H, Smith SC, Amal R. Understanding the Enhancement in Photoelectrochemical Properties of Photocatalytically Prepared TiO2-Reduced Graphene Oxide Composite. J Phys Chem C. 2011;115(13):6004-9.

[132] Li B, Zhang XT, Li XH, Wang L, Han RY, Liu BB, et al. Photo-assisted preparation and patterning of large-area reduced graphene oxide-TiO2 conductive thin film. Chem Commun. 2010;46(20):3499-501.

[133] Lambert TN, Chavez CA, Bell NS, Washburn CM, Wheeler DR, Brumbach MT. Large area mosaic films of graphene-titania: self-assembly at the liquid-air interface and photo-responsive behavior. Nanoscale. 2011;3(1):188-91.

[134] Akhavan O. Photocatalytic reduction of graphene oxides hybridized by ZnO nanoparticles in ethanol. Carbon. 2011;49(1):11-8.

[135] Williams G, Kamat PV. Graphene-Semiconductor Nanocomposites: Excited-State Interactions between ZnO Nanoparticles and Graphene Oxide. Langmuir. 2009;25(24):13869-73.

[136] Ng YH, Iwase A, Bell NJ, Kudo A, Amal R. Semiconductor/reduced graphene oxide nanocomposites derived from photocatalytic reactions. Catal Today. 2011;164(1):353-7.

[137] Cong HP, Ren XC, Wang P, Yu SH. Macroscopic Multifunctional Graphene-Based Hydrogels and Aerogels by a Metal Ion Induced Self-Assembly Process. Acs Nano. 2012;6(3):2693-703.

[138] Tang YB, Lee CS, Xu J, Liu ZT, Chen ZH, He ZB, et al. Incorporation of Graphenes in Nanostructured TiO2 Films via Molecular Grafting for Dye-Sensitized Solar Cell Application. Acs Nano. 2010;4(6):3482-8.

[139] Wang DH, Choi DW, Li J, Yang ZG, Nie ZM, Kou R, et al. Self-Assembled TiO2-Graphene Hybrid Nanostructures for Enhanced Li-Ion Insertion. Acs Nano. 2009;3(4):907-14.

[140] Wang DH, Kou R, Choi D, Yang ZG, Nie ZM, Li J, et al. Ternary Self-Assembly of Ordered Metal Oxide-Graphene Nanocomposites for Electrochemical Energy Storage. Acs Nano. 2010;4(3):1587-95.

[141] Wu ZS, Wang DW, Ren W, Zhao J, Zhou G, Li F, et al. Anchoring Hydrous RuO2 on Graphene Sheets for High-Performance Electrochemical Capacitors. Adv Funct Mater. 2010;20(20):3595-602.

[142] Liu HD, Gao P, Fang JH, Yang G. Li3V2(PO4)(3)/graphene nanocomposites as cathode material for lithium ion batteries. Chem Commun. 2011;47(32):9110-2.

[143] Cao AN, Liu Z, Chu SS, Wu MH, Ye ZM, Cai ZW, et al. A Facile One-step Method to Produce Graphene-CdS Quantum Dot Nanocomposites as Promising Optoelectronic Materials. Adv Mater. 2010;22(1):103-6.

[144] Wang P, Jiang TF, Zhu CZ, Zhai YM, Wang DJ, Dong SJ. One-Step, Solvothermal Synthesis of Graphene-CdS and Graphene-ZnS Quantum Dot Nanocomposites and Their Interesting Photovoltaic Properties. Nano Res. 2010;3(11):794-9.

[145] Chang K, Chen WX. In situ synthesis of MoS2/graphene nanosheet composites with extraordinarily high electrochemical performance for lithium ion batteries. Chem Commun. 2011;47(14):4252-4.

[146] Zou WB, Zhu JW, Sun YX, Wang X. Depositing ZnO nanoparticles onto graphene in a polyol system. Mater Chem Phys. 2011;125(3):617-20.

[147] Zhou KF, Zhu YH, Yang XL, Jiang X, Li CZ. Preparation of graphene-TiO2 composites with enhanced photocatalytic activity. New J Chem. 2011;35(2):353-9.

[148] Zhou KF, Zhu YH, Yang XL, Li CZ. Preparation and Application of Mediator-Free H2O2 Biosensors of Graphene-Fe3O4 Composites. Electroanal. 2011;23(4):862-9.

[149] Huang XD, Zhou XF, Zhou L, Qian K, Wang YH, Liu ZP, et al. A Facile One-Step Solvothermal Synthesis of SnO2/Graphene Nanocomposite and Its Application as an Anode Material for Lithium-Ion Batteries. Chemphyschem. 2011;12(2):278-81.

[150] Li BJ, Cao HQ, Shao J, Li GQ, Qu MZ, Yin G. Co3O4@graphene Composites as Anode Materials for High-Performance Lithium Ion Batteries. Inorg Chem. 2011;50(5):1628-32.

[151] Wang HW, Hu ZA, Chang YQ, Chen YL, Lei ZQ, Zhang ZY, et al. Facile solvothermal synthesis of a graphene nanosheet-bismuth oxide composite and its electrochemical characteristics. Electrochim Acta. 2010;55(28):8974-80.

[152] Stankovich S, Dikin DA, Dommett GHB, Kohlhaas KM, Zimney EJ, Stach EA, et al. Graphene-based composite materials. Nature. 2006;442(7100):282-6.

[153] Du M, Yang T, Jiao K. Immobilization-free direct electrochemical detection for DNA specific sequences based on electrochemically converted gold nanoparticles/graphene composite film. J Mater Chem. 2010;20(41):9253-60.

[154] Fu CP, Kuang YF, Huang ZY, Wang X, Du NN, Chen JH, et al. Electrochemical co-reduction synthesis of graphene/Au nanocomposites in ionic liquid and their electrochemical activity. Chem Phys Lett. 2010;499(4-6):250-3.

[155] Liu CB, Wang K, Luo SL, Tang YH, Chen LY. Direct Electrodeposition of Graphene Enabling the One-Step Synthesis of Graphene-Metal Nanocomposite Films. Small. 2011;7(9):1203-6.

[156] Liu S, Wang JQ, Zeng J, Ou JF, Li ZP, Liu XH, et al. "Green" electrochemical synthesis of Pt/graphene sheet nanocomposite film and its electrocatalytic property. J Power Sources. 2010;195(15):4628-33.

[157] Zhou YG, Chen JJ, Wang FB, Sheng ZH, Xia XH. A facile approach to the synthesis of highly electroactive Pt nanoparticles on graphene as an anode catalyst for direct methanol fuel cells. Chem Commun. 2010;46(32):5951-3.

[158] Wu SX, Yin ZY, He QY, Huang XA, Zhou XZ, Zhang H. Electrochemical Deposition of Semiconductor Oxides on Reduced Graphene Oxide-Based Flexible, Transparent, and Conductive Electrodes. J Phys Chem C. 2010;114(27):11816-21.

[159] Cheng Q, Tang J, Ma J, Zhang H, Shinya N, Qin LC. Graphene and nanostructured MnO2 composite electrodes for supercapacitors. Carbon. 2011;49(9):2917-25.

[160] Kim YT, Han JH, Hong BH, Kwon YU. Electrochemical Synthesis of CdSe Quantum-Dot Arrays on a Graphene Basal Plane Using Mesoporous Silica Thin-Film Templates. Adv Mater. 2010;22(4):515-8.

[161] Lin JA, Penchev M, Wang GP, Paul RK, Zhong JB, Jing XY, et al. Heterogeneous Graphene Nanostructures: ZnO Nanostructures Grown on Large-Area Graphene Layers. Small. 2010;6(21):2448-52.

[162] Kim S, Choi H, Jung M, Choi SY, Ju S. Hybrid nanowire-multilayer graphene film light-emitting sources. Nanotechnology. 2010;21(42).

[163] Yu KH, Lu GH, Mao S, Chen KH, Kim H, Wen ZH, et al. Selective Deposition of CdSe Nanoparticles on Reduced Graphene Oxide to Understand Photoinduced Charge Transfer in Hybrid Nanostructures. Acs Appl Mater Inter. 2011;3(7):2703-9.

[164] Zhang Y, Chen BA, Zhang LM, Huang J, Chen FH, Yang ZP, et al. Controlled assembly of Fe3O4 magnetic nanoparticles on graphene oxide. Nanoscale. 2011;3(4):1446-50.

[165] Zhang XY, Huang Y, Wang Y, Ma YF, Liu ZF, Chen YS. Synthesis and characterization of a graphene-C-60 hybrid material. Carbon. 2009;47(1):334-7.

[166] Liu ZB, Xu YF, Zhang XY, Zhang XL, Chen YS, Tian JG. Porphyrin and Fullerene Covalently Functionalized Graphene Hybrid Materials with Large Nonlinear Optical Properties. J Phys Chem B. 2009;113(29):9681-6.

[167] Zhang Y, Ren LQ, Wang SR, Marathe A, Chaudhuri J, Li GG. Functionalization of graphene sheets through fullerene attachment. J Mater Chem. 2011;21(14):5386-91.

[168] Kim YK, Min DH. Preparation of scrolled graphene oxides with multi-walled carbon nanotube templates. Carbon. 2010;48(15):4283-8.

[169] Yang J, Heo M, Lee HJ, Park SM, Kim JY, Shin HS. Reduced Graphene Oxide (rGO)-Wrapped Fullerene (C-60) Wires. Acs Nano. 2011;5(10):8365-71.

[170] Yang SB, Feng XL, Ivanovici S, Mullen K. Fabrication of Graphene-Encapsulated Oxide Nanoparticles: Towards High-Performance Anode Materials for Lithium Storage. Angew Chem Int Edit. 2010;49(45):8408-11.

[171] Zhang C, Ren LL, Wang XY, Liu TX. Graphene Oxide-Assisted Dispersion of Pristine Multiwalled Carbon Nanotubes in Aqueous Media. J Phys Chem C. 2010;114(26):11435-40.

[172] Myung S, Solanki A, Kim C, Park J, Kim KS, Lee KB. Graphene-Encapsulated Nanoparticle-Based Biosensor for the Selective Detection of Cancer Biomarkers. Adv Mater. 2011;23(19):2221-5.

[173] Fang YX, Guo SJ, Zhu CZ, Zhai YM, Wang EK. Self-Assembly of Cationic Polyelectrolyte-Functionalized Graphene Nanosheets and Gold Nanoparticles: A Two-Dimensional Heterostructure for Hydrogen Peroxide Sensing. Langmuir. 2010;26(13):11277-82.

[174] Li LL, Liu KP, Yang GH, Wang CM, Zhang JR, Zhu JJ. Fabrication of Graphene-Quantum Dots Composites for Sensitive Electrogenerated Chemiluminescence Immunosensing. Adv Funct Mater. 2011;21(5):869-78.

[175] Zhang M, Lei DN, Yin XM, Chen LB, Li QH, Wang YG, et al. Magnetite/graphene composites: microwave irradiation synthesis and enhanced cycling and rate performances for lithium ion batteries. J Mater Chem. 2010;20(26):5538-43.

[176] Zhou GM, Wang DW, Li F, Zhang LL, Li N, Wu ZS, et al. Graphene-Wrapped Fe3O4 Anode Material with Improved Reversible Capacity and Cyclic Stability for Lithium Ion Batteries. Chem Mater. 2010;22(18):5306-13.

[177] Wang JZ, Zhong C, Wexler D, Idris NH, Wang ZX, Chen LQ, et al. Graphene-Encapsulated Fe3O4 Nanoparticles with 3D Laminated Structure as Superior Anode in Lithium Ion Batteries. Chem-Eur J. 2011;17(2):661-7.

[178] Wang HL, Cui LF, Yang YA, Casalongue HS, Robinson JT, Liang YY, et al. Mn3O4-Graphene Hybrid as a High-Capacity Anode Material for Lithium Ion Batteries. J Am Chem Soc. 2010;132(40):13978-80.

[179] Mai YJ, Wang XL, Xiang JY, Qiao YQ, Zhang D, Gu CD, et al. CuO/graphene composite as anode materials for lithium-ion batteries. Electrochim Acta. 2011;56(5):2306-11.

[180] Wang B, Wu XL, Shu CY, Guo YG, Wang CR. Synthesis of CuO/graphene nanocomposite as a high-performance anode material for lithium-ion batteries. J Mater Chem. 2010;20(47):10661-4.

[181] Zhu JX, Sharma YK, Zeng ZY, Zhang XJ, Srinivasan M, Mhaisalkar S, et al. Cobalt Oxide Nanowall Arrays on Reduced Graphene Oxide Sheets with Controlled Phase, Grain Size, and Porosity for Li-Ion Battery Electrodes. J Phys Chem C. 2011;115(16):8400-6.

[182] Chen SQ, Wang Y. Microwave-assisted synthesis of a Co3O4-graphene sheet-on-sheet nanocomposite as a superior anode material for Li-ion batteries. J Mater Chem. 2010;20(43):9735-9.

[183] Wu ZS, Ren WC, Wen L, Gao LB, Zhao JP, Chen ZP, et al. Graphene Anchored with Co3O4 Nanoparticles as Anode of Lithium Ion Batteries with Enhanced Reversible Capacity and Cyclic Performance. Acs Nano. 2010;4(6):3187-94.

[184] Qiu YC, Yan KY, Yang SH, Jin LM, Deng H, Li WS. Synthesis of Size-Tunable Anatase TiO2 Nanospindles and Their Assembly into Anatase@Titanium Oxynitride/Titanium Nitride-Graphene Nanocomposites for Rechargeable Lithium Ion Batteries with High Cycling Performance. Acs Nano. 2010;4(11):6515-26.

[185] Chen JS, Wang ZY, Dong XC, Chen P, Lou XW. Graphene-wrapped TiO2 hollow structures with enhanced lithium storage capabilities. Nanoscale. 2011;3(5):2158-61.

[186] Zhu JX, Zhu T, Zhou XZ, Zhang YY, Lou XW, Chen XD, et al. Facile synthesis of metal oxide/reduced graphene oxide hybrids with high lithium storage capacity and stable cyclability. Nanoscale. 2011;3(3):1084-9.

[187] Zhu XJ, Zhu YW, Murali S, Stollers MD, Ruoff RS. Nanostructured Reduced Graphene Oxide/Fe2O3 Composite As a High-Performance Anode Material for Lithium Ion Batteries. Acs Nano. 2011;5(4):3333-8.

[188] Wang G, Liu T, Luo YJ, Zhao Y, Ren ZY, Bai JB, et al. Preparation of Fe2O3/graphene composite and its electrochemical performance as an anode material for lithium ion batteries. J Alloy Compd. 2011;509(24):L216-L20.

[189] Chang K, Chen WX. L-Cysteine-Assisted Synthesis of Layered MoS2/Graphene Composites with Excellent Electrochemical Performances for Lithium Ion Batteries. Acs Nano. 2011;5(6):4720-8.

[190] Zhang LS, Jiang LY, Yan HJ, Wang WD, Wang W, Song WG, et al. Mono dispersed SnO2 nanoparticles on both sides of single layer graphene sheets as anode materials in Li-ion batteries. J Mater Chem. 2010;20(26):5462-7.

[191] Wang XY, Zhou XF, Yao K, Zhang JG, Liu ZP. A SnO2/graphene composite as a high stability electrode for lithium ion batteries. Carbon. 2011;49(1):133-9.

[192] Ding Y, Jiang Y, Xu F, Yin J, Ren H, Zhuo Q, et al. Preparation of nano-structured LiFePO4/graphene composites by co-precipitation method. Electrochem Commun. 2010;12(1):10-3.

[193] Zhou XF, Wang F, Zhu YM, Liu ZP. Graphene modified LiFePO4 cathode materials for high power lithium ion batteries. J Mater Chem. 2011;21(10):3353-8.

[194] Rao CV, Reddy ALM, Ishikawa Y, Ajayan PM. LiNi1/3Co1/3Mn1/3O2-Graphene Composite as a Promising Cathode for Lithium-Ion Batteries. Acs Appl Mater Inter. 2011;3(8):2966-72.

[195] Yoo E, Kim J, Hosono E, Zhou H, Kudo T, Honma I. Large reversible Li storage of graphene nanosheet families for use in rechargeable lithium ion batteries. Nano Lett. 2008;8(8):2277-82.

[196] Zhang YP, Li HB, Pan LK, Lu T, Sun Z. Capacitive behavior of graphene-ZnO composite film for supercapacitors. J Electroanal Chem. 2009;634(1):68-71.

[197] Li FH, Song JF, Yang HF, Gan SY, Zhang QX, Han DX, et al. One-step synthesis of graphene/SnO2 nanocomposites and its application in electrochemical supercapacitors. Nanotechnology. 2009;20(45).

[198] Yan J, Wei T, Qiao WM, Shao B, Zhao QK, Zhang LJ, et al. Rapid microwave-assisted synthesis of graphene nanosheet/Co3O4 composite for supercapacitors. Electrochim Acta. 2010;55(23):6973-8.

[199] Yan J, Fan ZJ, Wei T, Qian WZ, Zhang ML, Wei F. Fast and reversible surface redox reaction of graphene-MnO2 composites as supercapacitor electrodes. Carbon. 2010;48(13):3825-33.

[200] Kim F, Luo JY, Cruz-Silva R, Cote LJ, Sohn K, Huang JX. Self-Propagating Domino-like Reactions in Oxidized Graphite. Adv Funct Mater. 2010;20(17):2867-73.

[201] Snook GA, Kao P, Best AS. Conducting-polymer-based supercapacitor devices and electrodes. J Power Sources. 2011;196(1):1-12.

[202] Wang HL, Hao QL, Yang XJ, Lu LD, Wang X. Graphene oxide doped polyaniline for supercapacitors. Electrochem Commun. 2009;11(6):1158-61.

[203] Hu YH, Wang H, Hu B. Thinnest Two-Dimensional Nanomaterial-Graphene for Solar Energy. Chemsuschem. 2010;3(7):782-96.

[204] Luo B, Liu SM, Zhi LJ. Chemical Approaches toward Graphene-Based Nanomaterials and their Applications in Energy-Related Areas. Small. 2012;8(5):630-46.

[205] Yang NL, Zhai J, Wang D, Chen YS, Jiang L. Two-Dimensional Graphene Bridges Enhanced Photoinduced Charge Transport in Dye-Sensitized Solar Cells. Acs Nano. 2010;4(2):887-94.

[206] Yen MY, Hsiao MC, Liao SH, Liu PI, Tsai HM, Ma CCM, et al. Preparation of graphene/multi-walled carbon nanotube hybrid and its use as photoanodes of dye-sensitized solar cells. Carbon. 2011;49(11):3597-606.

[207] Sun SR, Gao L, Liu YQ. Enhanced dye-sensitized solar cell using graphene-TiO2 photoanode prepared by heterogeneous coagulation. Appl Phys Lett. 2010;96(8).

[208] Guo CX, Yang HB, Sheng ZM, Lu ZS, Song QL, Li CM. Layered Graphene/Quantum Dots for Photovoltaic Devices. Angew Chem Int Edit. 2010;49(17):3014-7.

[209] Xu ZP, Buehler MJ. Geometry Controls Conformation of Graphene Sheets: Membranes, Ribbons, and Scrolls. Acs Nano. 2010;4(7):3869-76.

[210] Li Y, Fan XB, Qi JJ, Ji JY, Wang SL, Zhang GL, et al. Gold nanoparticles-graphene hybrids as active catalysts for Suzuki reaction. Mater Res Bull. 2010;45(10):1413-8.

[211] Qu LT, Liu Y, Baek JB, Dai LM. Nitrogen-Doped Graphene as Efficient Metal-Free Electrocatalyst for Oxygen Reduction in Fuel Cells. Acs Nano. 2010;4(3):1321-6.

[212] Yoo E, Okata T, Akita T, Kohyama M, Nakamura J, Honma I. Enhanced Electrocatalytic Activity of Pt Subnanoclusters on Graphene Nanosheet Surface. Nano Lett. 2009;9(6):2255-9.

[213] Dong LF, Gari RRS, Li Z, Craig MM, Hou SF. Graphene-supported platinum and platinum-ruthenium nanoparticles with high electrocatalytic activity for methanol and ethanol oxidation. Carbon. 2010;48(3):781-7.

[214] Hu YJ, Zhang H, Wu P, Zhang H, Zhou B, Cai CX. Bimetallic Pt-Au nanocatalysts electrochemically deposited on graphene and their electrocatalytic characteristics towards oxygen reduction and methanol oxidation. Phys Chem Chem Phys. 2011;13(9):4083-94.

[215] Yue QL, Zhang K, Chen XM, Wang L, Zhao JS, Liu JF, et al. Generation of OH radicals in oxygen reduction reaction at Pt-Co nanoparticles supported on graphene in alkaline solutions. Chem Commun. 2010;46(19):3369-71.

[216] Zhang XY, Li HP, Cui XL, Lin YH. Graphene/TiO2 nanocomposites: synthesis, characterization and application in hydrogen evolution from water photocatalytic splitting. J Mater Chem. 2010;20(14):2801-6.

[217] Liu JB, Fu SH, Yuan B, Li YL, Deng ZX. Toward a Universal "Adhesive Nanosheet" for the Assembly of Multiple Nanoparticles Based on a Protein-Induced Reduction/Decoration of Graphene Oxide. J Am Chem Soc. 2010;132(21):7279-81.

[218] Huang J, Zhang LM, Chen BA, Ji N, Chen FH, Zhang Y, et al. Nanocomposites of size-controlled gold nanoparticles and graphene oxide: Formation and applications in SERS and catalysis. Nanoscale. 2010;2(12):2733-8.

[219] Huang X, Zhou XZ, Wu SX, Wei YY, Qi XY, Zhang J, et al. Reduced Graphene Oxide-Templated Photochemical Synthesis and in situ Assembly of Au Nanodots to Orderly Patterned Au Nanodot Chains. Small. 2010;6(4):513-6.

[220] Jasuja K, Berry V. Implantation and Growth of Dendritic Gold Nanostructures on Graphene Derivatives: Electrical Property Tailoring and Raman Enhancement. Acs Nano. 2009;3(8):2358-66.

[221] Zhou HQ, Qiu CY, Yu F, Yang HC, Chen MJ, Hu LJ, et al. Thickness-Dependent Morphologies and Surface-Enhanced Raman Scattering of Ag Deposited on n-Layer Graphenes. J Phys Chem C. 2011;115(23):11348-54.

[222] Geng XM, Niu L, Xing ZY, Song RS, Liu GT, Sun MT, et al. Aqueous-Processable Noncovalent Chemically Converted Graphene-Quantum Dot Composites for Flexible and Transparent Optoelectronic Films. Adv Mater. 2010;22(5):638-42.

[223] Du J, Lai XY, Yang NL, Zhai J, Kisailus D, Su FB, et al. Hierarchically Ordered Macro-Mesoporous TiO2-Graphene Composite Films: Improved Mass Transfer, Reduced Charge Recombination, and Their Enhanced Photocatalytic Activities. Acs Nano. 2011;5(1):590-6.

[224] Yang XY, Zhang XY, Ma YF, Huang Y, Wang YS, Chen YS. Superparamagnetic graphene oxide-Fe3O4 nanoparticles hybrid for controlled targeted drug carriers. J Mater Chem. 2009;19(18):2710-4.

[225] Paek SM, Yoo E, Honma I. Enhanced Cyclic Performance and Lithium Storage Capacity of SnO2/Graphene Nanoporous Electrodes with Three-Dimensionally Delaminated Flexible Structure. Nano Lett. 2009;9(1):72-5.

[226] Zhang LS, Liang XQ, Song WG, Wu ZY. Identification of the nitrogen species on N-doped graphene layers and Pt/NG composite catalyst for direct methanol fuel cell. Phys Chem Chem Phys. 2010;12(38):12055-9.

[227] Xu C, Wang X, Zhu JW. Graphene-Metal Particle Nanocomposites. J Phys Chem C. 2008;112(50):19841-5.

[228] Michaels AM, Jiang J, Brus L. Ag nanocrystal junctions as the site for surface-enhanced Raman scattering of single Rhodamine 6G molecules. J Phys Chem B. 2000;104(50):11965-71.

[229] Das MR, Sarma RK, Saikia R, Kale VS, Shelke MV, Sengupta P. Synthesis of silver nanoparticles in an aqueous suspension of graphene oxide sheets and its antimicrobial activity. Colloid Surface B. 2011;83(1):16-22.

[230] Zhu MS, Chen PL, Liu MH. Graphene Oxide Enwrapped Ag/AgX (X = Br, Cl) Nanocomposite as a Highly Efficient Visible-Light Plasmonic Photocatalyst. Acs Nano. 2011;5(6):4529-36.

[231] Lee J, Novoselov KS, Shin HS. Interaction between Metal and Graphene: Dependence on the Layer Number of Graphene. Acs Nano. 2011;5(1):608-12.

[232] Gotoh K, Kinumoto T, Fujii E, Yamamoto A, Hashimoto H, Ohkubo T, et al. Exfoliated graphene sheets decorated with metal/metal oxide nanoparticles: Simple preparation from cation exchanged graphite oxide. Carbon. 2011;49(4):1118-25.

[233] Tien HW, Huang YL, Yang SY, Wang JY, Ma CCM. The production of graphene nanosheets decorated with silver nanoparticles for use in transparent, conductive films. Carbon. 2011;49(5):1550-60.

[234] He FA, Fan JT, Song F, Zhang LM, Chan HLW. Fabrication of hybrids based on graphene and metal nanoparticles by in situ and self-assembled methods. Nanoscale. 2011;3(3):1182-8.

[235] Wang Y, Shi ZQ, Huang Y, Ma YF, Wang CY, Chen MM, et al. Supercapacitor Devices Based on Graphene Materials. J Phys Chem C. 2009;113(30):13103-7.

[236] Wang Y, Wu YP, Huang Y, Zhang F, Yang X, Ma YF, et al. Preventing Graphene Sheets from Restacking for High-Capacitance Performance. J Phys Chem C. 2011;115(46):23192-7.

[237] Hou JB, Shao YY, Ellis MW, Moore RB, Yi BL. Graphene-based electrochemical energy conversion and storage: fuel cells, supercapacitors and lithium ion batteries. Physical Chemistry Chemical Physics. 2011;13(34):15384-402.

[238] Sheng KX, Xu YX, Li C, Shi GQ. High-performance self-assembled graphene hydrogels prepared by chemical reduction of graphene oxide. New Carbon Mater. 2011;26(1):9-15.

[239] Le LT, Ervin MH, Qiu HW, Fuchs BE, Lee WY. Graphene supercapacitor electrodes fabricated by inkjet printing and thermal reduction of graphene oxide. Electrochem Commun. 2011;13(4):355-8.

[240] Li YM, van Zijll M, Chiang S, Pan N. KOH modified graphene nanosheets for supercapacitor electrodes. J Power Sources. 2011;196(14):6003-6.

[241] Lv W, Tang DM, He YB, You CH, Shi ZQ, Chen XC, et al. Low-Temperature Exfoliated Graphenes: Vacuum-Promoted Exfoliation and Electrochemical Energy Storage. Acs Nano. 2009;3(11):3730-6.

[242] Zhu YW, Murali S, Stoller MD, Ganesh KJ, Cai WW, Ferreira PJ, et al. Carbon-Based Supercapacitors Produced by Activation of Graphene. Science. 2011;332(6037):1537-41.

[243] Hao QL, Wang HL, Yang XJ, Lu LD, Wang X. Morphology-controlled fabrication of sulfonated graphene/polyaniline nanocomposites by liquid/liquid interfacial polymerization and investigation of their electrochemical properties. Nano Res. 2011;4(4):323-33.

[244] Shi WH, Zhu JX, Sim DH, Tay YY, Lu ZY, Zhang XJ, et al. Achieving high specific charge capacitances in Fe3O4/reduced graphene oxide nanocomposites. J Mater Chem. 2011;21(10):3422-7.

[245] Wee G, Mak WF, Phonthammachai N, Kiebele A, Reddy MV, Chowdari BVR, et al. Particle Size Effect of Silver Nanoparticles Decorated Single Walled Carbon Nanotube Electrode for Supercapacitors. J Electrochem Soc. 2010;157(2):A179-A84.

[246] Wang T, Kaempgen M, Nopphawan P, Wee G, Mhaisalkar S, Srinivasan M. Silver nanoparticle-decorated carbon nanotubes as bifunctional gas-diffusion electrodes for zinc-air batteries. J Power Sources. 2010;195(13):4350-5.

[247] Wang SR, Tambraparni M, Qiu JJ, Tipton J, Dean D. Thermal Expansion of Graphene Composites. Macromolecules. 2009;42(14):5251-5.

[248] Tang XZ, Cao ZW, Zhang HB, Liu J, Yu ZZ. Growth of silver nanocrystals on graphene by simultaneous reduction of graphene oxide and silver ions with a rapid and efficient one-step approach. Chem Commun. 2011;47(11):3084-6.

[249] Navaladian S, Viswanathan B, Viswanath RP, Varadarajan TK. Thermal decomposition as route for silver nanoparticles. Nanoscale Res Lett. 2007;2(1):44-8.

[250] Logvinenko V, Polunina O, Mikhailov Y, Mikhailov K, Bokhonov B. Study of thermal decomposition of silver acetate. J Therm Anal Calorim. 2007;90(3):813-6.

[251] Waterhouse GIN, Bowmaker GA, Metson JB. The thermal decomposition of silver (I, III) oxide: A combined XRD, FT-IR and Raman spectroscopic study. Phys Chem Chem Phys. 2001;3(17):3838-45.

[252] Olson LP, Whitcomb DR, Rajeswaran M, Blanton TN, Stwertka BJ. The simple yet elusive crystal structure of silver acetate and the role of the Ag-Ag bond in the formation of silver nanoparticles during the thermally induced reduction of silver carboxylates. Chem Mater. 2006;18(6):1667-74.

[253] Hula RC, Edtmaier C, Holzweber M, Hutter H, Eisenmenger-Sittner C. The wetting behaviour of silver on carbon, pure and carburized nickel, cobalt and molybdenum substrates. Appl Surf Sci. 2010;256(14):4697-701.

[254] Veca LM, Lu FS, Meziani MJ, Cao L, Zhang PY, Qi G, et al. Polymer functionalization and solubilization of carbon nanosheets. Chem Commun. 2009(18):2565-7.

[255] Yang J, Zang CL, Sun L, Zhao N, Cheng XN. Synthesis of graphene/Ag nanocomposite with good dispersibility and electroconductibility via solvothermal method. Mater Chem Phys. 2011;129(1-2):270-4.

[256] Cai WP, Zhong HC, Zhang LD. Optical measurements of oxidation behavior of silver nanometer particle within pores of silica host. J Appl Phys. 1998;83(3):1705-10.

[257] Lavrenko VA, Malyshevskaya AI, Kuznetsova LI, Litvinenko VF, Pavlikov VN. Features of high-temperature oxidation in air of silver and alloy Ag-Cu, and adsorption of oxygen on silver. Powder Metall Met C+. 2006;45(9-10):476-80.

[258] Berger C, Song ZM, Li XB, Wu XS, Brown N, Naud C, et al. Electronic confinement and coherence in patterned epitaxial graphene. Science. 2006;312(5777):1191-6.

[259] Wei ZQ, Barlow DE, Sheehan PE. The Assembly of Single-Layer Graphene Oxide and Graphene Using Molecular Templates. Nano Lett. 2008;8(10):3141-5.

[260] Salavagione HJ, Gomez MA, Martinez G. Polymeric Modification of Graphene through Esterification of Graphite Oxide and Poly(vinyl alcohol). Macromolecules. 2009;42(17):6331-4.

[261] Hu HT, Wang XB, Wang JC, Wan L, Liu FM, Zheng H, et al. Preparation and properties of graphene nanosheets-polystyrene nanocomposites via in situ emulsion polymerization. Chem Phys Lett. 2010;484(4-6):247-53.

[262] Xu YF, Liu ZB, Zhang XL, Wang Y, Tian JG, Huang Y, et al. A Graphene Hybrid Material Covalently Functionalized with Porphyrin: Synthesis and Optical Limiting Property. Adv Mater. 2009;21(12):1275-79.

[263] Xu C, Wu XD, Zhu JW, Wang X. Synthesis of amphiphilic graphite oxide. Carbon. 2008;46(2):386-9.

[264] Stankovich S, Piner RD, Nguyen ST, Ruoff RS. Synthesis and exfoliation of isocyanate-treated graphene oxide nanoplatelets. Carbon. 2006;44(15):3342-7.

[265] Shen JF, Hu YH, Li C, Qin C, Ye MX. Synthesis of Amphiphilic Graphene Nanoplatelets. Small. 2009;5(1):82-5.

[266] Niyogi S, Bekyarova E, Itkis ME, McWilliams JL, Hamon MA, Haddon RC. Solution properties of graphite and graphene. J Am Chem Soc. 2006;128(24):7720-1.

[267] Zhang XY, Huang Y, Wang Y, Ma YF, Liu ZF, Chen YS. Synthesis and characterization of a graphene-C(60) hybrid material. Carbon. 2009;47(1):334-7.

[268] Zhang XY, Liu ZB, Huang Y, Wan XJ, Tian JG, Ma YF, et al. Synthesis, Characterization and Nonlinear Optical Property of Graphene-C(60) Hybrid. J Nanosci Nanotechno. 2009;9(10):5752-6.

[269] Yu DS, Park K, Durstock M, Dai LM. Fullerene-Grafted Graphene for Efficient Bulk Heterojunction Polymer Photovoltaic Devices. J Phys Chem Lett. 2011;2(10):1113-8.

[270] Mao Y, Gleason KK. Hot filament chemical vapor deposition of poly(glycidyl methacrylate) thin films using tert-butyl peroxide as an initiator. Langmuir. 2004;20(6):2484-8.

[271] Vandijkwolthuis WNE, Franssen O, Talsma H, Vansteenbergen MJ, Vandenbosch JJK, Hennink WE. Synthesis, Characterization, and Polymerization of Glycidyl Methacrylate Derivatized Dextran. Macromolecules. 1995;28(18):6317-22.

[272] Wang S, Liang R, Wang B, Zhang C. Epoxide-terminated carbon nanotubes. Carbon. 2007;45(15):3047-9.

[273] Szabo T, Berkesi O, Forgo P, Josepovits K, Sanakis Y, Petridis D, et al. Evolution of surface functional groups in a series of progressively oxidized graphite oxides. Chem Mater. 2006;18(11):2740-9.

[274] Titelman GI, Gelman V, Bron S, Khalfin RL, Cohen Y, Bianco-Peled H. Characteristics and microstructure of aqueous colloidal dispersions of graphite oxide. Carbon. 2005;43(3):641-9.

[275] Mao CB, Zhou L, Wu XZ, Sun XY. The combination of the polymeric solution-sol-gel process and combustion synthesis to manufacture BiPbSrCaCuO powder. Supercond Sci Tech. 1996;9(11):994-1000.

[276] Kirwan LJ, Fawell PD, van Bronswijk W. An in situ FTIR-ATR study of polyacrylate adsorbed onto hematite at high pH and high ionic strength. Langmuir. 2004;20(10):4093-100.

[277] Ramachandran E, Natarajan S. XRD, thermal and FTIR studies on gel grown DL-phenylalanine crystals. Cryst Res Technol. 2007;42(6):617-20.

[278] Fabian J. Theoretical investigation of the C-60 infrared spectrum. Phys Rev B. 1996;53(20):13864-70.

[279] Sun XM, Liu Z, Welsher K, Robinson JT, Goodwin A, Zaric S, et al. Nano-Graphene Oxide for Cellular Imaging and Drug Delivery. Nano Res. 2008;1(3):203-12.

[280] Wang SR, Zhang Y, Abidi N, Cabrales L. Wettability and Surface Free Energy of Graphene Films. Langmuir. 2009;25(18):11078-81.

[281] Delgado JL, de la Cruz P, Urbina A, Navarrete JTL, Casado J, Langa F. The first synthesis of a conjugated hybrid of C-60-fullerene and a single-wall carbon nanotube. Carbon. 2007;45(11):2250-2.

[282] Rodrigues OED, Saraiva GD, Nascimento RO, Barros EB, Mendes J, Kim YA, et al. Synthesis and Characterization of Selenium-Carbon Nanocables. Nano Lett. 2008;8(11):3651-5.

[283] Mao AQ, Zhang DH, Jin X, Gu XL, Wei XQ, Yang GJ, et al. Synthesis of graphene oxide sheets decorated by silver nanoparticles in organic phase and their catalytic activity. J Phys Chem Solids. 2012;73(8):982-6.

[284] Alargova RG, Deguchi S, Tsujii K. Stable colloidal dispersions of fullerenes in polar organic solvents. J Am Chem Soc. 2001;123(43):10460-7.

[285] Yoshimoto S, Amano J, Miura K. Synthesis of a fullerene/expanded graphite composite and its lubricating properties. J Mater Sci. 2010;45(7):1955-62.

[286] Jorge G. Domínguez-Chávez SC-M, Ivana Moggio, Eduardo Arias-Marín, Tatiana Klimova, Irina Lijanova and Marcos Martínez-García*. Double Molecular Antenna Pyrene –Bridge - Fullerene C_{60}. The Open Organic Chemistry Journal. 2010;4:15-23.

[287] Melenevskaya EVCaEY. Analysis of Interactions in Fullerene-solvent-polymer System by UV-spectroscopy. Fullerenes, Nanotubes and Carbon Nanostructures. 2008;16:640–3.

[288] Dresselhaus MS, Chen G, Tang MY, Yang RG, Lee H, Wang DZ, et al. New directions for low-dimensional thermoelectric materials. Adv Mater. 2007;19(8):1043-53.

[289] Yee SK, Malen JA, Majumdar A, Segalman RA. Thermoelectricity in Fullerene-Metal Heterojunctions. Nano Lett. 2011;11(10):4089-94.

[290] Zhang B, Sun J, Katz HE, Fang F, Opila RL. Promising Thermoelectric Properties of Commercial PEDOT:PSS Materials and Their Bi2Te3 Powder Composites. Acs Appl Mater Inter. 2010;2(11):3170-8.

[291] Aich RB, Blouin N, Bouchard A, Leclerc M. Electrical and Thermoelectric Properties of Poly(2,7-Carbazole) Derivatives. Chem Mater. 2009;21(4):751-7.

[292] Fan XA, Yang JY, Zhu W, Bao SQ, Duan XK, Xiao CJ, et al. Effect of nominal Sb2Te3 content on thermoelectric properties of p-type (Bi2Te3)(x)(Sb2Te3)(1-x) alloys by MA-HP. J Phys D Appl Phys. 2006;39(23):5069-73.

[293] Zhao Y, Tang GS, Yu ZZ, Qi JS. The effect of graphite oxide on the thermoelectric properties of polyaniline. Carbon. 2012;50(8):3064-73.

[294] Kun Zhang MD, Jingjing Qiu, Louisa Hope-Weeks and Shiren Wang. Thermoelectric properties of porous multi-walled carbon nanotube/polyaniline core/shell nanocomposites. Nanotechnology. 2012 23:8.

[295] Hiroshige Y, Ookawa M, Toshima N. High thermoelectric performance of poly(2,5-dimethoxyphenylenevinylene) and its derivatives. Synthetic Met. 2006;156(21-24):1341-7.

[296] Zhao XB, Hu SH, Zhao MJ, Zhu TJ. Thermoelectric properties of Bi0.5Sb1.5Te3/polyaniline hybrids prepared by mechanical blending. Mater Lett. 2002;52(3):147-9.

[297] Meng CZ, Liu CH, Fan SS. A Promising Approach to Enhanced Thermoelectric Properties Using Carbon Nanotube Networks. Adv Mater. 2010;22(4):535-9.

[298] Yu C, Choi K, Yin L, Grunlan JC. Light-Weight Flexible Carbon Nanotube Based Organic Composites with Large Thermoelectric Power Factors. Acs Nano. 2011;5(10):7885-92.

[299] Yin ZY, Wu SX, Zhou XZ, Huang X, Zhang QC, Boey F, et al. Electrochemical Deposition of ZnO Nanorods on Transparent Reduced Graphene Oxide Electrodes for Hybrid Solar Cells. Small. 2010;6(2):307-12.

[300] Sootsman JR, Chung DY, Kanatzidis MG. New and Old Concepts in Thermoelectric Materials. Angew Chem Int Edit. 2009;48(46):8616-39.

[301] Snyder GJ, Toberer ES. Complex thermoelectric materials. Nat Mater. 2008;7(2):105-14.

[302] Ni XX, Liang GC, Wang JS, Li BW. Disorder enhances thermoelectric figure of merit in armchair graphane nanoribbons. Appl Phys Lett. 2009;95(19).

[303] Sevincli H, Cuniberti G. Enhanced thermoelectric figure of merit in edge-disordered zigzag graphene nanoribbons. Phys Rev B. 2010;81(11).

[304] Checkelsky JG, Ong NP. Thermopower and Nernst effect in graphene in a magnetic field. Phys Rev B. 2009;80(8).

[305] Wei P, Bao WZ, Pu Y, Lau CN, Shi J. Anomalous Thermoelectric Transport of Dirac Particles in Graphene. Phys Rev Lett. 2009;102(16).

[306] Xiao N, Dong XC, Song L, Liu DY, Tay Y, Wu SX, et al. Enhanced Thermopower of Graphene Films with Oxygen Plasma Treatment. Acs Nano. 2011;5(4):2749-55.

[307] Sim D, Liu DY, Dong XC, Xiao N, Li SA, Zhao Y, et al. Power Factor Enhancement for Few-Layered Graphene Films by Molecular Attachments. J Phys Chem C. 2011;115(5):1780-5.

[308] Paloheimo J, Isotalo H, Kastner J, Kuzmany H. Conduction Mechanisms in Undoped Thin-Films of C60 and C60/70. Synthetic Met. 1993;56(2-3):3185-90.

[309] Sumino M, Harada K, Ikeda M, Tanaka S, Miyazaki K, Adachi C. Thermoelectric properties of n-type C-60 thin films and their application in organic thermovoltaic devices. Appl Phys Lett. 2011;99(9).

[310] Zhou YX, Wu PX, Cheng ZY, Ingram J, Jeelani S. Improvement in electrical, thermal and mechanical properties of epoxy by filling carbon nanotube. Express Polym Lett. 2008;2(1):40-8.

[311] Tsai TC, Chang HC, Chen CH, Whang WT. Widely variable Seebeck coefficient and enhanced thermoelectric power of PEDOT:PSS films by blending thermal decomposable ammonium formate. Org Electron. 2011;12(12):2159-64.

[312] Poehler TO, Katz HE. Prospects for polymer-based thermoelectrics: state of the art and theoretical analysis. Energ Environ Sci. 2012;5(8):8110-5.

[313] Humphrey TE, O'Dwyer MF, Linke H. Power optimization in thermionic devices. J Phys D Appl Phys. 2005;38(12):2051-4.

[314] Mathkar A, Tozier D, Cox P, Ong PJ, Galande C, Balakrishnan K, et al. Controlled, Stepwise Reduction and Band Gap Manipulation of Graphene Oxide. J Phys Chem Lett. 2012;3(8):986-91.

[315] He M, Ge J, Lin ZQ, Feng XH, Wang XW, Lu HB, et al. Thermopower enhancement in conducting polymer nanocomposites via carrier energy scattering at the organic-inorganic semiconductor interface. Energ Environ Sci. 2012;5(8):8351-8.

[316] Brownson DAC, Munro LJ, Kampouris DK, Banks CE. Electrochemistry of graphene: not such a beneficial electrode material? Rsc Adv. 2011;1(6):978-88.

[317] Du Y, Shen SZ, Cai KF, Casey PS. Research progress on polymer-inorganic thermoelectric nanocomposite materials. Prog Polym Sci. 2012;37(6):820-41.

Publications

Peer-Reviewed Journal Papers

Xin Zhang, Walid M. Hikal, **Yue Zhang**, Sanjoy K. Bhattacharia, Li Li, Siddharth Panditrao, Shiren Wang, and Brandon L. Weeks, "Direct laser initiation and improved thermal stability of nitrocellulose/ graphene oxide nanocomposites", (Accepted, Applied Physics Letters).

Yue Zhang, Liqiang Ren, Kun Zhang, , Shiren Wang and Jingjing Qiu, "Graphene nanobelt-enhanced organic solar cells", Science of Advanced Materials, (2013), 5, 366-372.

Yue Zhang, Shiren Wang, Li Li, Kun Zhang, Jingjing Qiu, Marauo Davis, Louisa J Hope-Weeks, "Tuning electrical conductivity and surface area of chemically-exfoliated graphene through nanocrystal functionalization ", Materials Chemistry and Physics (2012), 135(2-3), 1057-1063.

Yue Zhang, Liqiang Ren, Shiren Wang, Archis Marathe, Jharna Chaudhuri, Guigen Li, "Functionalization of graphene sheets through fullerene attachment", Journal of Materials Chemistry (2011), 21(14), 5386-5391.

Shiren Wang, **Yue Zhang**, Noureddine Abidi, Luis Cabrales, "Wettability and Surface Free Energy of Graphene Films". Langmuir 2009, 25 (18), 11078-11081.

Xiaoxi Huang, Xiaolin Li, **Yue Zhang**, Dawei Dong, Liqun Zhang, "Investigation on Swelling Property of Rubber in Asphalt". Special Purpose Rubber Products, 2009 30(3), 35-39.

Liqiang Ren, **Yue Zhang**, Jingjing Qiu, and Shiren Wang, "Exploring thermally reduced graphene nanodisc as an additive for polymer solar cells" (Submitted to Organic Electronics).

Yue Zhang, Kun Zhang, Jingjing Qiu, and Shiren Wang, "High Seebeck effects from conducting polymer: Poly(3,4-ethylenedioxythiophene): poly(styrenesulfonate) nanocomposite with hybrid C60/graphene architecture", (Submitted).

Yue Zhang, Kun Zhang, Li Li, Jingjing Qiu, and Shiren Wang, "Enhanced thermoelectric performance of epoxy resin nanocomposite prepared with C_{60}/graphene hybrid", (Submitted).

Conference Papers

Yue Zhang, Shiren Wang, Kun Zhang, Jingjing Qiu, Marauo Davis and Hope-Weeks Louisa, "Electrical conductivity and surface area of silver nanoparticle/graphene hybrid", Proceeding of SAMPE 2011.

Yue Zhang, Madhava Tambraparni, Shiren Wang, "Graphene composites for thermal management applications", Proceeding of SAMPE 2010.

PATENT

Liqun Zhang, Xiaoxi Huang, Xiaolin Li, **Yue Zhang**, Wei Xie, Guichang Cao, "Method for preparing rubber powder masterbatch capable of quickly dispersing modified asphalt", PRC Patent CN 101565286 A, published on Oct. 28 2009.